Metal-Insulator Transition in Two-Dimensional Hubbard and Extended Hubbard Models: a Numerical Study.

Habilitationsschirft

F. F. Assaad

Institut für Theoretische Physik III,
Universität Stuttgart,
Pfaffenwaldring 57, D-70550 Stuttgart
Germany.

1998

Abstract

Quantum Monte Carlo simulations of the two-dimensional Hubbard model with Coulomb repulsion U and hopping matrix element t lead to the conclusion that the doping induced metal-insulator transition in this model is anomalous. The statement is based on the following data. i) The charge susceptibility scales as $\chi_c \sim |\mu - \mu_c|^{-1/2}$ where μ (μ_c) is the (critical) chemical potential. ii) The *low temperature* high-frequency Hall coefficient in the strong and weak coupling regimes remains electron-like with small amplitude at the transition. iii) The zero temperature single particle Green function for frequencies ω in the charge gap scales as $G(\vec{r}, \omega) \sim \exp(-|\vec{r}|/\xi_l)$ with $\xi_l \sim |\omega - \mu_c|^{-1/4}$. In a single particle picture the latter result leads to a flat, $|\vec{k}|^4$, dispersion relation at the critical point. By computing the single particle spectral function $A(\vec{k}, \omega)$ at zero temperature, half-band filling on 16×16 clusters, we confirm the existence of such a dispersion relation around the $(\pm\pi, 0)$ and $(0, \pm\pi)$ points in the Brillouin zone. Following the idea that such a flat dispersion relation places metallic state in the vicinity of the metal-insulator close to a number of instabilities, we extended the Hubbard model with a term W which depends upon the square of a local kinetic energy. This term contains pair hopping processes. At finite values of W the localization length satisfies $\xi_l \sim |\omega - \mu_c|^{-1/2}$. This change in exponent is related to a transition from a $|\vec{k}|^4$ to a $|\vec{k}|^2$ dispersion relation around the $(0, \pm\pi)$, $(\pm\pi, 0)$ points in the Brillouin zone as W is enhanced. At finite doping $d_{x^2-y^2}$ pair field correlation grow rapidly as a function of W and the uniform spin susceptibility shows a pseudogap behavior. The results imply that doping the Mott insulator at finite values of W leads to a $d_{x^2-y^2}$ superconductor. At half-band filling and constant U, W triggers a quantum transition between the Mott insulator and $d_{x^2-y^2}$ superconductor. We study this quantum transition and put the emphasis on the nature of static and dynamical spin degrees of freedom in the superconducting state. The data shows a remarkable compatibility between antiferromagnetic fluctuations and $d_{x^2-y^2}$ superconductivity. This is summarized by the following points. i) The equal time spin-spin correlations follow a powerlaw $e^{-i\vec{r}\cdot\vec{Q}}|\vec{r}|^{-\alpha}$. Here $\vec{Q} = (\pi, \pi)$ and α is in the range $1 < \alpha < 2$ and depends upon the coupling constants W and U. This result is reached on the basis of zero temperature calculations on lattice sizes up to 24×24. ii) The spin relaxation rate $1/T_1$ scales to zero but the staggered spin susceptibility $\mathrm{Re}\chi(\vec{q} = (\pi, \pi), \omega = 0)$ diverges in the low temperature limit. Finally, $\mathrm{Im}\chi(\vec{q} = (\pi, \pi), \omega)$ shows a peak at finite frequencies.

Contents

Introduction

Given a band structure

$$\epsilon_{\pm}(\vec{k}) = \pm\left(\Delta + \frac{\hbar^2\vec{k}^2}{2m}\right) \tag{1}$$

an insulating state will be obtained when the N-single particle states of the lower band are doubly occupied with electrons. This insulator has a charge gap

$$\Delta_c = \frac{1}{4}\left(E_0(2N+2, S_z=0) - 2E_0(2N, S_z=0) + E_0(2N-2, S_z=0)\right) = \Delta \tag{2}$$

and a spin gap

$$\Delta_s = E_0(2N, S_z=1) - E_0(2N, S_z=0) = 2\Delta. \tag{3}$$

Here, $E_0(N, S_z)$ denotes the ground state energy with N-electrons and total z-component of spin S_z.

A correlated or Mott insulator is an insulator which finds its origin in the electron-electron interaction. This interaction is not taken into account by the band structure. A prototype model which describes a Mott insulator is given by the Hubbard Hamiltonian:

$$H = -t\sum_{\langle\vec{i},\vec{j}\rangle,\sigma}\left(c^{\dagger}_{\vec{i},\sigma}c_{\vec{j},\sigma} + \text{H.c.}\right) + U\sum_{\vec{i}} n_{\vec{i},\uparrow}n_{\vec{i},\downarrow} \tag{4}$$

Here, $c^{\dagger}_{\vec{i},\sigma}$ ($c_{\vec{i},\sigma}$) creates (annihilates) an electron with z-component of spin σ on site $\vec{i}$ and $n_{\vec{i},\sigma} = c^{\dagger}_{\vec{i},\sigma}c_{\vec{i}\sigma}$. We consider a square lattice and the sum $\langle\vec{i},\vec{j}\rangle$ runs over nearest neighbors. The kinetic energy is diagonal in Fourier space and at half-band filling (one electron per site) predicts a metallic state. On the other hand, the potential term is diagonal in real space. At half-filling it predicts an insulator since double occupancy required to carry a charge from one side of the sample to the other costs an energy set by U. This competition between localization (diagonal in real space) and delocalization (diagonal in Fourier space) constitutes the central difficulty in solving the model. In one dimension, an exact solution is available [1]. At any finite value of the repulsion U a charge gap is present. In two-dimensions there is no exact solution. Numerically a single particle gap accompanied by the vanishing of the Drude weight [2] is seen at half-filling [3–8]. Thus, the correct starting point to capture the physics of the half-filled Hubbard model is to consider the kinetic term as a perturbation to the potential term. This perturbation is important since the ground state of just the Hubbard term is macroscopically degenerate due to the spin degrees of freedom. Treating the kinetic energy up to second order in perturbation theory yields the Heisenberg model,

$$H = J \sum_{\langle \vec{i}, \vec{j} \rangle} \vec{S}_{\vec{i}} \cdot \vec{S}_{\vec{j}} \tag{5}$$

where $J = 4t^2/U$. On a square lattice, there is ample numerical evidence that the Heisenberg [9,10] and half-filled Hubbard models [11,12] show long range antiferromagnetic spin ordering at zero temperature. Along with this continuous symmetry breaking comes a Goldstone mode: spin waves. Thus the insulating state of the Hubbard model has a charge gap but no spin gap. This distinguishes it from a band-insulator.

Undoped high-T_c cuprates constitute a modern example of a two-dimensional Mott insulator [13]. Band structure calculations of $La_{2-\delta}Sr_{\delta}CuO_4$ at $\delta = 0$ predict a metallic state [14]. Experimentally, an insulating state with long range antiferromagnetic order is seen [15]. The building blocks of high-T_c cuprates are CuO_2 planes. Their physics has been argued to be captured by the single band Hubbard or t-J models [16,17] on a square lattice. At half band filling, those models map onto the Heisenberg model which in turn maps onto the $O(3)$ non-linear sigma model. In its renormalized classical regime, the latter model accounts well for the spin degrees of freedom of undoped cuprates [18, 19]. Correlated insulators may take different forms and show spin as well as charge gaps. An example of such insulators are even leg-ladder systems realized for example in $Sr_2Cu_3O_5$ [20]. Those systems may be described by the Hubbard model on ladder geometries [21]. They differ from the band insulator since the spin and charge gaps are not related by the simple relation of Eq. (2) and (3). In fact, the spin gap may continuously be driven to zero and the charge gap kept finite by changing the parameters of the model. Here, we will concentrate on Mott insulators with long range antiferromagnetic order.

Our motivation is to understand the nature of the resulting metallic state obtained by doping a correlated insulator with long range antiferromagnetic order. High-T_c cuprates have revealed the richness of the physics obtained when a Mott insulator is doped. As a first step we study the metal-insulator transition and will assume that it is a continuous transition. For a recent review of the metal-insulator transition we refer the reader to [22].

An important issue concerns the nature of the spin degrees of freedom when charge carries are added to the insulating state. In one dimension, the insulating state of the Hubbard model has antiferromagnetic correlations which decay as

$1/r$ where r denotes the distance [23]. Here, we omit logarithmic corrections. At infinitesimal doping, long range spin-spin correlations decay as $r^{-1.5}$ with a $2k_f$ modulation [24]. Here k_f is the Fermi wave vector. It has been shown [25, 26] that there is a length scale set by the mean hole distance, $1/\delta$, below (above) which the the spin-spin correlations decay as $1/r$ ($1/r^{1.5}$). This magnetic length scale diverges continuously at the metal-insulator transition since δ is nothing but the doping.

In two dimensions, an important question is the existence or non-existence of long range magnetic order in the metallic phase. From the experimental point of view, doping $La_{2-\delta}Sr_{\delta}CuO_4$ with as little as $\delta = 0.02$ is sufficient to destroy magnetic order and at $\delta = 0.05$ the metallic state occurs [15]. From the analytical point of view, mean-field approximations or more sophisticated approximations which satisfy Pauli principle as well as the Mermin-Wagner theorem predict the existence of magnetic order in the metallic state [27,28]. Numerical calculations of the Hubbard and t-J models seems to exclude the occurrence of long range order for dopings $\delta > 0.05$ [6, 29, 30]. Thus numerics as well as experiment are consistent with the picture that the metal-insulator transition as well as the magnetic transition occur simultaneously. That both transitions occur simultaneously is important. Consider the length scale ξ set by the mean hole distance. This length scale diverges at the metal insulator transition. If the metal-insulator and magnetic transitions occur simultaneously, it is plausible to assume that as in the one-dimensional case ξ is also the relevant length scale for spin degrees of freedom. Thus both the charge and magnetic degrees of freedom have to be treated on the same footing since they have the same characteristic energy scale. The numerical data of Refs. [6,29,30] show that the spin-structure factor is consistent with $S(\vec{Q}_m) \sim \delta$ where $\vec{Q}_m$ corresponds to the wave vector for which $S(\vec{Q}_m)$ is maximal. This may be interpreted with a magnetic length scale which scales as $\delta^{-1/2}$ which is nothing but the mean hole distance in two dimensions.

Another line of argument to understand the relevance of antiferromagnetic order in the metallic phase is the following. Antiferromagnetic order doubles the unit cell and thus halves the Brillouin zone. In the reduced Brillouin zone (i.e. magnetic Brillouin zone) the insulator corresponds to a filled band. If antiferromagnetic order survives doping it is plausible to assume that the physics of the metal-insulator transition is captured by adding holes to this band. In contrast, if magnetic order disappears with the metal-insulator transition, this simple rigid band picture fails since the magnetic Brillouin zone itself is destroyed.

We now consider the charge degrees of freedom. To characterize the metal-insulator transition, we can consider the charge susceptibility, $\chi_c = \partial n/\partial \mu$, the Drude weight D [2] or the Hall coefficient R_H. Here, n denotes the particle number and μ the chemical potential. One can also study the metal-insulator transition by approaching it from the insulator side. In order to do so we propose the following. In the terminology of the band insulator described by the band structure of Eq. 1, we place an impurity state in the gap. The impurity state can hybridize with the band electrons and has a energy $-\Delta < E_i < \Delta$. The localization length of the impurity state will diverge as E_i approaches the band edge Δ. In the case of a band metal-insulator transition, the above quantities satisfy:

$$D \sim \delta, \;\; R_H \sim \frac{1}{\delta}, \;\; \chi_c \sim \delta^{1-2/d}, \;\; \text{and} \;\; \xi_l \sim |E_i - \Delta|^{-1/2}. \tag{6}$$

Here, δ denotes the doping ($\delta = 0$ corresponds to the insulator) and d is the dimensionality. Are those relations valid when a correlated insulator is doped? The answer is model and dimension dependent.

In one dimension, the metal-insulator transition obtained by doping the Hubbard model does indeed satisfy the above equations [22]. The charge susceptibility as well as the Drude weight may be calculated with the use of the Bethe-Ansatz solution [31, 32]. In Chap. 2 we will compute numerically the localization length and see that it satisfies $\xi_l \sim |E_i - \Delta|^{-1/2}$.

We now consider the two dimensional case for which we have the following numerical data.

i: For the Hubbard and t-J models numerics are consistent with $\chi_c \sim \delta^{-1}$ [6, 29, 30, 33]. This results stands in contrast to the band metal-insulator transition which satisfies $\chi_c \sim \delta^0$ in two dimensions. For the Hubbard model $\chi_c \sim \delta^{-1}$ was shown to be independent on nesting properties. Turning on a *small* next nearest neighbor hopping matrix element $t'/t = 0.2$ does not alter the exponent.

ii: In Chap. 1 we define and compute the high frequency Hall coefficient for the Hubbard model. At *low* temperatures, both in the weak and strong coupling regimes, this quantity does not diverge at the metal-insulator transition. Our results are consistent with an electron like Hall coefficient with small amplitude at the metal-insulator transition.

iii: In Chap. 2, we calculate the localization lenght for the two-dimensional Hubbard model. Simulations at zero temperature on clusters up to 16×16 are consistent with $\xi_l \sim |\omega - \mu_c|^{-1/4}$ where in the above terminology ω corresponds to the energy of the impurity state and μ_c to the charge gap. In a single particle picture, the result $\xi_l \sim |\omega - \mu_c|^{-1/4}$ may be understood through the existence of a flat band with dispersion relation $|\vec{k}|^4$ at the critical point. Based on the calculation of the single particle spectral function, $A(\vec{k}, \omega)$, we provide numerical evidence for the existence of those flat bands around the $(0, \pm\pi)$ and $(\pm\pi, 0)$ points in the Brillouin zone. In model calculations this flat dispersion relation has been pointed out in Refs. [34–36]. In high-T_c cuprates the occurrence of flat bands at finite doping is documented in Refs. [37, 38].

iv: Recently, the quotient $D/\langle K \rangle$ where $\langle K \rangle$ denotes the kinetic energy, has been computed on small clusters for the t-J model. The results are consistent with $D/\langle K \rangle \sim \delta$ [39] for *small* values of δ. Since one expects $\langle K \rangle \sim \delta$ this leads to

$D \sim \delta^2$. The above leads to the concept of an incoherent metallic state in the vicinity of the metal-insulator transition. Since $D \sim \delta^2$ and the optical conductivity satisfies the sum rule $\int d\omega \sigma(\omega) \sim -\langle K \rangle \sim \delta$ most of the weight in $\sigma(\omega)$ is not located in the coherent Drude response but in the incoherent response at higher frequencies.

The numerical results, $D \sim \delta^2$ [39], $\chi_c \sim \delta^{-1}$ [6, 29, 30, 33], and $\xi_l \sim |\omega - \mu_c|^{-1/4}$ in two dimensions, may be understood under the assumption of a single relevant length scale and a hyperscaling form for the singular part of the free energy provided that we accept an anomalously large dynamical exponent $z = 4$ [22, 40]. Since the metal-insulator transition is driven by a change in chemical potential the constraint $\nu z = 1$ holds. Here ν corresponds to the correlation length exponent. The band metal insulator transition in all dimensions as well as the metal-insulator transition in the one-dimensional Hubbard model satisfy this hyperscaling assumption with $z = 2$ and $\nu = 1/2$. We will briefly review the assumption of hyperscaling in Sec. 2.5.

The observed flat dispersion relation places the metallic state in the vicinity of the metal-insulator transition close to various instabilities. The metallic state will be very sensitive to perturbations capable restoring coherence. From this status arises the motivation of adding a term to the Hubbard model. This constitutes the topic of Chap. 3. The term we add essentially contains pair hopping processes and has a matrix element set by W. We will refer to this model as the t-U-W model. We argue that low energy physics of the W term may be accounted for by the three-site term obtained in a strong coupling expansion of the Hubbard model [41]. For values of $W < W_c$ the insulating state at half-filling remains invariant. However, the nature of the doping induced metal-insulator transition changes since already for *small* values of W/t the localization lenght satisfies $\xi_l \sim |\omega - \mu_c|^{-1/2}$. This change in exponent is accompanied by the disappearance of the flat dispersion relation observed in the Hubbard model at the $(0, \pm\pi)$, $(\pm\pi, 0)$ points in the Brillouin zone. Recent numerical calculation of the Drude weight on small clusters are consistent with $D \sim \delta$ [39] at finite values of W. The change in the nature of the metal-insulator transition may be traced back to the nature of the metallic state. Indeed, we give numerical evidence that doping the Mott insulator at finite values of W/t leads to a $d_{x^2-y^2}$ superconductor. Since the added term does not favor d-wave paring over extended s-wave pairing we conclude that the d-wave symmetry is naturally selected due to the underlying magnetic degrees of freedom.

At half-band filling, constant value of U, W triggers a zero temperature transition between the correlated insulator with long range antiferromagnetic order and a d-wave superconductor. We will discuss some aspect of this transition in Sec. 3.3 and put emphasis on the nature of the spin correlations in the superconducting phase. The results show a remarkable compatibility between antiferromagnetic fluctuations and d-wave superconductivity.

In three dimensions, the metal insulator transition may equally show an anomalous character. To illustrate this, we consider the compound $Sr_{1-x}La_xTiO_3$ [42]. At $x = 1$ titanium is in a Ti^{3+} state thus leaving one electron on the d-shell. Band structure calculations thus to a metallic state. Experimentally an insulator with Neel ordering of the Ti^{3+} $S = 1/2$ spins is observed ($T_N = 120 - 150K$). The Ti-atoms form a nearly cubic array and, provided that orbital degeneracy may be neglected, this state may be described by a half-filled Hubbard model on a cubic lattice. Replacing La by Sr introduces charge carries. At $x < 0.95$ a metallic state with no long range magnetic order is obtained. This metallic state has a T^2 resistivity as expected in Fermi-Liquid theory. At $x = 0$ titanium is in a Ti^{4+} state thus leaving the d-shell empty. This leads to a band insulator. Experiments show that the Hall coefficient satisfies $R_H \sim 1/x$. When approaching the Mott insulator ($x = 1$) the Hall coefficient shows no divergence. At the band insulator ($x = 0$) R_H diverges as in Eq. 6. As the Mott insulating state is approached both the spin susceptibility as well as the coefficient of the T-linear term in the specific heat (γ) diverge. The Wilson ratio, which is given by the quotient of the two former quantities remains constant for all considered values of x. No anomaly is observed in χ_s and γ when the band insulator is approached. Thus, this metal-insulator transition at $x = 1$ bears some similarities with the two dimensional case in the sense that it can be understood by the divergence of the effective mass as opposed to the vanishing of number of charge carriers. However, it is not clear if it belongs to the same universality class as the two dimensional case described by the dynamical exponent $z = 4$ and correlation length exponent $\nu = 1/4$. To answer this question from the theoretical side, one requires a calculation of the localization length as well as of the Drude weight. This is a numerically challenging task. Alternatively, Ti-oxides have been discussed in the approximation of infinite dimension (infinite coordination number) [43,44]. In this approximation, γ diverges at the metal-insulator transition realized at $x = 1$. In infinite dimensions, the self energy is local [45]. Thus, antiferromagnetic fluctuations as well as correlation induced flat bands around some special $\vec{k}$-points in the Brillouin zone are not described within this approach.

The article is organized as follows. In Chap 1 we concentrate on the high frequency Hall coefficient. This is a challenging calculation for the quantum Monte Carlo method so that we will spend some time discussing the setup. In Chap. 2 we study the metal-insulator transition by approaching it from the insulating side. Chap. 3 is devoted to the t-U-W model. From the technical point of view, we have used auxiliary field quantum Monte Carlo methods [46] both at finite [12,47] and zero temperature [48–50]. Dynamical results were obtained with the use of the Maximum Entropy method [51,52]. The results presented here are based on some technical innovations which are described in Chap. 4. Some aspects of the work presented in this article have been published in Refs. [53–58].

Chapter 1

High Frequency Hall Coefficient for the Hubbard Model

In the Drude description of metals, the Drude weight is given by $D = \pi e^2 n/m$ and the Hall coefficient by $R_H = 1/nec$ where n (m) denotes the density (effective mass) of charge carriers in the relevant single-particle description. Already in a semi-classical approach, this interpretation of the Hall coefficient fails when the relaxation time, τ, is $\vec{k}$ dependent. Shastry et al. [59] have proposed to consider the Hall coefficient at frequencies $\omega \gg 1/\tau(\vec{k})$. At those frequencies, the Hall coefficient, is insensitive to the functional form of $\tau(\vec{k})$ and is inversely proportional to the density of charge carriers. This quantity is a probe for the nature of a metal-insulator transition where the Drude weight scales continuously to zero. There are two ways in which the Drude weight can vanish: i) the number of charge carries scales to zero thus leading to a divergence in the high frequency Hall coefficient. This is the case in a band metal-insulator transition (See Eq.(6) of the introduction) ii) The effective mass of the charge carries diverges. In this case one does not expect any singularity in the Hall coefficient at the metal-insulator transition.

Here we compute the high frequency Hall coefficient for the two dimensional Hubbard model with the use of quantum Monte Carlo methods. At *low* temperatures and in the vicinity of the Mott transition, our results show no enhancement of R_H in both the weak and strong coupling regimes. At energy scales accessible to the Monte Carlo method, our results are consistent with a metal-insulator transition driven by the divergence of the effective mass as opposed to the vanishing of the number of charge carriers [60].

The organization of this chapter is the following. In the next sections, we will define the high frequency Hall coefficient and give examples for the non-interacting case. We then discuss some special aspects of the Monte-Carlo method for the computation of R_H. Our numerical results are discussed in Sec. 1.4.

1.1 Definition of R_H

Our starting point is the two-dimensional Hubbard model in a transverse magnetic field:

$$H = \sum_{\langle \vec{i},\vec{j} \rangle,\sigma} \left(t_{\vec{i},\vec{j}} \left(\vec{A} \right) c^{\dagger}_{\vec{i},\sigma} c_{\vec{j},\sigma} + \text{H.c.} \right) + U \sum_{\vec{i}} n_{\vec{i},\uparrow} n_{\vec{i},\downarrow}. \tag{1.1}$$

Here, $\langle \vec{i}, \vec{j} \rangle$ denotes nearest-neighbors, $c^{\dagger}_{\vec{i},\sigma}$ ($c_{\vec{i},\sigma}$) creates (annihilates) an electron with z-component of spin σ on site $\vec{i}$ and $n_{\vec{i},\sigma} = c^{\dagger}_{\vec{i},\sigma} c_{\vec{i}\sigma}$. The hopping matrix elements contain the Peierls phase factors, $t_{\vec{i},\vec{j}}(\vec{A}) = -t \exp\left(\frac{2\pi i}{\Phi_0} \int_{\vec{i}}^{\vec{j}} \vec{A} \cdot d\vec{l} \right)$ where Φ_0 is the flux quantum and in the Landau gauge $\vec{A}(\vec{l}) = -B(l_y, 0, 0)$. The square lattice lies in the $\vec{e}_x$, $\vec{e}_y$ plane. To reduce finite size effects we consider a torus geometry and thus have to impose the boundary conditions:

$$c^{\dagger}_{\vec{i}+\vec{L}_\alpha,\sigma} = \exp\left(\frac{2\pi i}{\Phi_0} \chi_{\vec{L}_\alpha}(\vec{i}) \right) c^{\dagger}_{\vec{i},\sigma}. \tag{1.2}$$

Here, $\vec{L}_\alpha$ is a vector with norm equal to the linear size of the lattice, along the $\vec{e}_\alpha$ direction and $\alpha = x, y$. $\chi_{\vec{L}_\alpha}\left(\vec{i}\right)$ is defined with:

$$\vec{A}(\vec{x} + \vec{L}_\alpha) = \vec{A}(\vec{x}) + \vec{\nabla} \chi_{\vec{L}_\alpha}(\vec{x}). \tag{1.3}$$

With the above boundary conditions, one obtains:

$$[H, T_{\vec{L}_x}] = [H, T_{\vec{L}_y}] = 0 \tag{1.4}$$

where $T_{\vec{x}}$ is the translation operator over a distance $\vec{x}$. To obtain a single valued wave function, one requires: $[T_{\vec{L}_x}, T_{\vec{L}_y}] = 0$. Since in general:

$$T_{\vec{L}_x} T_{\vec{L}_y} = \exp\left(\frac{2\pi i}{\Phi_0} B L_x L_y \right) T_{\vec{L}_y} T_{\vec{L}_x}, \tag{1.5}$$

one has the constraint:

$$B L_x L_y = n \Phi_0 \tag{1.6}$$

with n an integer. Hence, the smallest magnetic field one may consider is given by

$$B a^2 / \Phi_0 = 1/L^2 \tag{1.7}$$

where a is the lattice constant and L the linear number of sites [61]. Due to the above constraint, the extrapolation to small magnetic fields is coupled to the thermodynamic limit. In all our calculation, we will adopt the above scaling of the magnetic field.

The linear response to a time dependent electric field $\vec{E}(t) = \vec{E}(\omega)\exp(-i\omega t)$ yields the conductivity tensor: $\sigma_{\alpha,\gamma}(i\omega_m) = \frac{e^2}{\hbar\omega_m} D_{\alpha,\gamma}(i\omega_m)$ where

$$D_{\alpha,\gamma}(i\omega_m) = \frac{1}{L^2}\left(-\frac{\langle K\rangle}{2}\delta_{\alpha,\gamma} - \int_0^\beta \mathrm{d}\tau e^{i\omega_m \tau}\langle j_\alpha(\tau) j_\gamma(0)\rangle\right). \tag{1.8}$$

In the above equation, $\omega_m = 2\pi m/\beta$ are Matsubara frequencies, β is the inverse temperature, $\langle K\rangle$ denotes the thermal average of the kinetic energy in Eq. (1.1), and $j_\alpha = -i\sum_{\vec{i},\sigma}\left(t_{\vec{i},\vec{i}+\vec{a}_\alpha}(\vec{A})c^\dagger_{\vec{i},\sigma}c_{\vec{i}+\vec{a}_\alpha,\sigma} - t_{\vec{i}+\vec{a}_\alpha,\vec{i}}(\vec{A})c^\dagger_{\vec{i}+\vec{a}_\alpha,\sigma}c_{\vec{i},\sigma}\right)$. We define R_H by:

$$R_H(B, i\omega_m) = \frac{1}{B}\frac{\sigma_{x,y}(i\omega_m)}{\sigma^2_{x,x}(i\omega_m) + \sigma^2_{x,y}(i\omega_m)}. \tag{1.9}$$

The above corresponds to the quantity we will compute with the QMC method. To make contact with experiments, one should calculate $R_H(B,\omega)$ for real frequencies. From the technical point of view, this requires analytical continuation imaginary time data. Although this is possible for σ_{xx}, fluctuations in σ_{xy} are large thus making the analytical continuation hard. We now show, however, that there are limiting cases where $R_H(B,\omega)$ and $R_H(B, i\omega_m)$ coincide. In the high frequency limit, $\omega >> U, t$ one obtains:

$$R^\star_H = R_H(B, \omega\to\infty) = R_H(B, i\omega_m \to i\infty) = -\frac{4\hbar L^2}{e^2 B}\frac{i\langle[j_x, j_y]\rangle}{\langle K\rangle^2}. \tag{1.10}$$

Taking the combined limit to infinite volume and vanishing magnetic fields (see Eq. (1.7)), one obtains:

$$\lim_{L\to\infty} R^\star_H = -\frac{(2\pi)^2}{ec}\frac{\int \mathrm{d}\vec{k}\cos(k_x)\cos(k_y)n(\vec{k})}{\left(\sum_\sigma \int \mathrm{d}\vec{k}\cos(k_x)n(\vec{k})\right)^2} \tag{1.11}$$

This relates $R^\star_H$ to the momentum distribution $n(\vec{k}) \equiv \sum_\sigma \langle c^\dagger_{\vec{k},\sigma}c_{\vec{k},\sigma}\rangle$ in the absence of magnetic field.

In the appendix, we show that

$$\lim_{i\omega_m\to 0}\lim_{B\to 0}\lim_{T\to 0} R_H(B, i\omega_m) = \lim_{\omega\to 0}\lim_{B\to 0}\lim_{T\to 0} R_H(B,\omega). \tag{1.12}$$

The assumption for this demonstration is that the Drude weight or charge stiffness does not vanish in the zero temperature zero field limit. The ordering of the limits are important, and this has consequences on the interpretation of the above quantity. Let us consider a Fermi liquid where the lifetime of the quasiparticles $1/\tau \sim T^2$ where T is the temperature. In the above equation, we first take the limit $T \to 0$ and only then the limit $\omega \to 0$. Thus we are always in a situation where, $1/\tau <<$

$\omega << U, t$. Hence in both limiting cases, we are dealing with a high frequency Hall coefficient in the sense that $\omega >> 1/\tau$ [1]. At those frequencies, and irrespective of the scattering processes, the Hall coefficient in a semiclassical picture may be interpreted as measure of the nature and density of charge carriers.

1.2 R_H for a non-spherical Fermi surface

We now show that for the non-interacting case, $U/t = 0$, our definition of the Hall coefficient yields correct results already on very small lattices. To show this, we will calculate $R_H(B, i\omega_m)$ with use of the Boltzmann transport equation as well as with the above Kubo formula and then compare results.

1.2.1 Kubo formula

It is convenient to work within the Landau gauge: $\vec{A}(\vec{l}) = -B(l_y, 0, 0)$. The boundary conditions are then given by:

$$c^\dagger_{\vec{j}+\vec{L}_x} = c^\dagger_{\vec{j}} \text{ and } c^\dagger_{\vec{j}+\vec{L}_y} = \exp(-2\pi i B L j_x/\Phi_0) c^\dagger_{\vec{j}}. \quad (1.13)$$

Within this subsection, we set the lattice constant to unity and omit the spin indices. One may now carry out a partial Fourier transform:

$$c^\dagger_{(p,j_y)} = \frac{1}{\sqrt{L}} \sum_{j_x=1}^{L} \exp(-ipj_x) c^\dagger_{(j_x,j_y)} \quad (1.14)$$

to obtain

$$H_t = -t \sum_{p,j_y} \left[2\cos(p + 2\pi B j_y/\Phi_0) c^\dagger_{(p,j_y)} c_{(p,j_y)} + c^\dagger_{(p,j_y)} c_{(p,j_y+1)} + c^\dagger_{(p,j_y+1)} c_{(p,j_y)} \right] \quad (1.15)$$

with the boundary condition:

$$c^\dagger_{(p,j_y+L)} = c^\dagger_{(p+2\pi N_\Phi/L, j_y)}. \quad (1.16)$$

Here, $p = 2\pi n_p/L$, $n_p : 1 \ldots L$ and N_Φ corresponds to the total number of flux quanta traversing the lattice. In our case, $N_\Phi = 1$. Thus, all momentum sectors defined by p, are connected via the boundary and H_t is given by $H_t = \sum_{s,t} c^\dagger_s T_{s,t} c_t$ where T is a symmetric matrix and $s \equiv (p, j_y)$. We diagonalize T numerically for small lattices to obtain: $\mathrm{diag}(\lambda_1 \ldots \lambda_N) = U^T T U$ where U is an orthogonal matrix. With the canonical transformation $\eta_r = \sum_s U^T_{r,s} c_s$, $H_t = \sum_s \lambda_s \eta^\dagger_s \eta_s$. We may now express

[1] We thank P. A. Lee for pointing this out to us

the current operator as $j_\alpha = \sum_{r,s} j^\alpha_{r,s} \eta^\dagger_r \eta_s$ where the matrix $j^\alpha_{r,s}$ is fully determined by the orthogonal transformation U. The current-current correlations are given by:

$$\int_0^\beta e^{i\omega_m \tau} \langle j_\alpha(\tau) j_\gamma(0) \rangle = \sum_{r,s} f^\alpha_{r,s} f^\gamma_{s,r} \frac{\langle \eta^\dagger_s \eta_s \rangle - \langle \eta^\dagger_r \eta_r \rangle}{i\omega_m + \lambda_r - \lambda_s} \tag{1.17}$$

where $\langle \eta^\dagger_s \eta_s \rangle = \left(1 + e^{\beta(\lambda_s - \mu)}\right)^{-1}$. β is the inverse temperature and μ the chemical potential. The sum over r, s is carried out numerically.

1.2.2 Boltzmann transport equation

In this approach, the starting point is the semiclassical motion of electrons in a magnetic field $\vec{B}$ [62]:

$$\hbar \frac{\mathrm{d}\vec{k}}{\mathrm{d}t} = \frac{e}{c} \vec{v} \times \vec{B} \tag{1.18}$$

where

$$\vec{v} = \frac{1}{\hbar} \vec{\nabla}_{\vec{k}} \cdot \epsilon(\vec{k}). \tag{1.19}$$

Here, $\epsilon(\vec{k})$ is the dispersion relation and $\vec{k}$ the crystal momentum. The lattice lies in the x, y plane and the B filed is along the z-direction. The energy $\epsilon(\vec{k})$ is a conserved quantity, so that the electrons move on constant energy contours. We consider only closed orbits. Since $\mathrm{d}\vec{\mathrm{k}}$ is perpendicular to the velocity, one has

$$\mathrm{d}t = \frac{\hbar c}{eB} \frac{|\mathrm{d}\vec{k}|}{|\vec{v}_\perp|} \tag{1.20}$$

where $\vec{v}_\perp = (-v_y, v_x)$. The time required to accomplish a revolution around a closed orbit of energy ϵ is given by

$$T_H = \oint_{\gamma_\epsilon} \frac{\hbar c}{eB} \frac{|\mathrm{d}\vec{k}|}{|\vec{v}_\perp|}. \tag{1.21}$$

We define the cyclotron frequency $\omega_H = \frac{2\pi}{T_H}$ and a phase variable $\phi = \omega_H t$. For a complete circuit, ϕ varies from 0 to 2π. Since ϵ is a constant of motion and ω_H depends only on ϵ one has

$$\frac{\mathrm{d}\phi}{\mathrm{d}t} = \omega_H. \tag{1.22}$$

It is convenient to write the Boltzmann transport equation in terms of the variables ϵ, ϕ and t. We consider an external electric field $\vec{E}(t) = \vec{E} e^{i\omega t}$ and denote by $f(\epsilon, \phi, t)$ ($f_0(\epsilon)$) the nonequilibrium (equilibrium) distribution of electrons. Here, $f_0(\epsilon) = \left(1 + e^{\beta(\epsilon - \mu)}\right)^{-1}$. In the relaxation time approximation, the out of equilibrium distribution function

$$g(\epsilon, \phi, t) = f(\epsilon, \phi, t) - f_0(\epsilon) \tag{1.23}$$

satisfies the differential equation $\frac{\mathrm{d}g}{\mathrm{d}t} = -g/\tau$. Keeping only terms linear to the electric field and noting that $\frac{\mathrm{d}\epsilon}{\mathrm{d}t} = \hbar\vec{v}\cdot\frac{\mathrm{d}\vec{k}}{\mathrm{d}t} = e\vec{v}\cdot\vec{E}(t)$ one obtains.

$$-e\frac{\partial f_0}{\partial\epsilon}\vec{v}\cdot\vec{E}(t) = g/\tau + \omega_H\frac{\partial g}{\partial\phi} + \frac{\partial g}{\partial t}. \tag{1.24}$$

The solution is given by:

$$g(\epsilon,\phi,t) = -\frac{e}{\omega_H}\frac{\partial f_0}{\partial\epsilon}e^{i\omega t}\int_{-\infty}^{\phi}\mathrm{d}\phi'\vec{v}(\epsilon,\phi',t)\cdot\vec{E}e^{(i\omega+1/\tau)(\phi'-\phi)/\omega_H} \tag{1.25}$$

The current is given by:

$$j_\alpha = \frac{e}{(2\pi)^2}\int\mathrm{d}\vec{k}v_\alpha(\vec{k},t)g(\vec{k},t) = \frac{e}{(2\pi\hbar)^2}\int\mathrm{d}\epsilon\ m_H\int_0^{2\pi}\mathrm{d}\phi v_\alpha(\epsilon,\phi,t)g(\epsilon,\phi,t) \tag{1.26}$$

with $m_H = eB/\omega_H c$. The $\vec{k}$ (ϵ) integration is over the Brillouin zone (band width). The conductivity tensor is determined by:

$$\sigma_{\alpha,\gamma} = -\left(\frac{e}{2\pi\hbar}\right)^2\int\mathrm{d}\epsilon\frac{m_H}{\omega_H}\frac{\partial f_0}{\partial\epsilon}\int_0^{2\pi}\mathrm{d}\phi v_\alpha(\phi)\int_0^{\infty}\mathrm{d}\phi' v_\gamma(\phi-\phi')e^{-(i\omega+1/\tau)\phi'/\omega_H} \tag{1.27}$$

The above Eq. corresponds to the Shockley tube-integral formula (See Ref. [62] Page. 301). Since $v_\gamma(\phi)$ is a periodic function of period 2π, the integral over ϕ' may be split into intervals of 2π to obtain:

$$\sigma_{\alpha,\gamma} = -\left(\frac{e}{2\pi\hbar}\right)^2\int\mathrm{d}\epsilon\frac{m_H}{\omega_H}\frac{\partial f_0}{\partial\epsilon}\frac{\int_0^{2\pi}\mathrm{d}\phi\int_0^{2\pi}\mathrm{d}\phi' v_\alpha(\phi)v_\gamma(\phi-\phi')e^{-(i\omega+1/\tau)\phi'/\omega_H}}{1-e^{-(i\omega+1/\tau)2\pi/\omega_H}} \tag{1.28}$$

Defining the Fourier transform:

$$v_\alpha(\phi) = \sum_n e^{-in\phi}v_{\alpha,n} \text{ with } v_{\alpha,n} = \frac{1}{2\pi}\int_0^{2\pi}\mathrm{d}\phi e^{in\phi}v_\alpha(\phi) \tag{1.29}$$

where n is an integer yields the final result:

$$\sigma_{\alpha,\gamma} = -\frac{e^2}{2\pi\hbar^2}\int\mathrm{d}\epsilon\ m_H\frac{\partial f_0}{\partial\epsilon}\sum_n\frac{v_{\alpha,n}v_{\gamma,-n}}{i\omega+1/\tau-in\omega_H}. \tag{1.30}$$

For a general dispersion relation we calculate the cyclotron frequency, ω_H, and Fourier coefficients, $v_{\alpha,n}$ numerically. At zero temperature, the integral over energy falls out since $\frac{\partial f_0}{\partial\epsilon} = \delta(\epsilon-\epsilon_F)$ where ϵ_F is the Fermi energy. For a circular Fermi line obtained with the dispersion $\epsilon(\vec{k}) = \hbar^2|\vec{k}|^2/2m$ the cyclotron frequency is given by $\omega_H = eB/mc$ and only $v_{\alpha,n=\pm1}$ does not vanish. In this simple case, Eq. (1.30) reduces to

$$\begin{aligned} \sigma_{xx} &= \frac{e^2 n}{m} \frac{i\omega + 1/\tau}{(i\omega + 1/\tau)^2 + \omega_H^2} \\ \sigma_{xy} &= \frac{e^2 n \omega_H}{m} \frac{1}{(i\omega + 1/\tau)^2 + \omega_H^2} \end{aligned} \tag{1.31}$$

and $R_H(B,\omega) \equiv 1/nec$ where n corresponds to the density of electrons.

We now compare the result of the two approaches, for the non-interacting case, $U/t = 0$ and band filling $\langle n \rangle = 0.8$. We consider essentially zero temperature, $\beta t \equiv t/T = 10^4$. The symbols in Fig. 1.1, correspond to Hall coefficient obtained within the Kubo formalism for different lattice sizes. For a given lattice size, the magnetic field is set to $Ba^2/\Phi_0 = 1/L^2$. Given this magnetic field, the solid lines correspond to the result obtained with the above described Boltzmann transport equation. As appropriate for the zero temperature limit, we have set $\tau = \infty$. There are no fitting parameters. Several points may be made:
i) Perfect agreement between both approaches is obtained except for the low frequency data for the 6×6 lattice where the discrepancy is due to energy gaps in finite size systems. This agreement on small lattice is surprising since the semiclassical picture applies only in the thermodynamic limit where the Fermi surface is well defined.
ii) The crossover between the high and low frequency values of R_H occurs at the cyclotron frequency, ω_H. As seen previously, in the special case of a circular Fermi surface, R_H is frequency independent. The high frequency value of R_H (1.10) converges to the prediction of the Boltzmann equation in the weak field limit (i.e. $\omega_H \tau \ll 1$). This may be shown explicitly by writing Eq. (1.11) as:

$$R_H^\star = \frac{(2\pi)^2}{ec} \frac{\int \mathrm{d}\vec{k} \frac{\partial f}{\partial \epsilon} \frac{\partial \epsilon}{\partial k_x} \left(\frac{\partial^2 \epsilon}{\partial k_x \partial k_y} \frac{\partial \epsilon}{\partial k_y} - \frac{\partial^2 \epsilon}{\partial k_y^2} \frac{\partial \epsilon}{\partial k_x} \right)}{\left(\int \mathrm{d}\vec{k} \frac{\partial f}{\partial \epsilon} \left(\frac{\partial \epsilon}{\partial k_x} \right)^2 \right)^2} \tag{1.32}$$

with $\epsilon(\vec{k}) = -2t(\cos(k_x) + \cos(k_y))$. This result may equally be obtained by expanding $v_\gamma(\phi - \phi')$ in Eq. (1.28) in ϕ' around ϕ. This expansion is valid for $|i\omega + 1/\tau|/\omega_H \gg 1$. That the high frequency value of R_H (1.10) converges to the prediction of the Boltzmann equation in the weak field limit may be understood by noting that if the frequency of the applied electric field is much larger than ω_H, the semi-classical motion of the electron on Fermi-surface will be perturbed before accomplishing a full revolution. The same picture applies in the weak field limit. As shown by this simple example, and as argued by Shastry et al. [59], R_H in the high frequency limit is related to the semi-classical Hall coefficient in the weak field

limit.
iii) $\lim_{B\to 0} R_H(B, i\omega_m)$ is independent of ω_m and corresponds to the result of the Boltzmann transport equation in the weak field limit.

1.3 Aspects of the QMC method for the computation of R_H

The details of the auxiliary field QMC method [46] applied to Hubbard models will we reviewed in Chap. 4. Here, we comment on some special aspects of the method for the calculation of the Hall coefficient. The first step is to incorporate the magnetic field in the finite temperature QMC simulations of the Hubbard model [12, 47]. This aspects has been discussed in detail in Ref. [63]. After a discrete Hubbard Stratonovitch (HS) transformation of the Hubbard interaction, one may integrate out the fermionic. The expectation value of an observables may be computed with

$$\langle O \rangle \equiv \frac{\mathrm{Tr}\left[e^{-\beta(H-\mu N)} O\right]}{\mathrm{Tr}\left[e^{-\beta(H-\mu N)}\right]} = \frac{\sum_x \det\left[M(x)\right] O(x)}{\sum_x \det\left[M(x)\right]}. \tag{1.33}$$

Here, x denotes a configuration of HS fields, $M(x)$ is an $N \times N$ matrix and $O(x)$ is the expectation value of the observable O for the a given HS configuration. The presence of the magnetic field renders the fermionic determinant $\det\left[M(x)\right]$ complex. We thus define a probability distribution:

$$\Pr(x) = \frac{|\det\left[M(x)\right]|}{\sum_x |\det\left[M(x)\right]|} \tag{1.34}$$

With the above definition,

$$\langle O \rangle = \frac{\sum_x \Pr(x) s(x) O(x)}{\sum_x \Pr(x) s(x)}, \quad s(x) = \frac{\det\left[M(x)\right]}{|\det\left[M(x)\right]|}. \tag{1.35}$$

Although $s(x)$ is complex, the average sign, $\langle s \rangle \equiv \sum_x \Pr(x) s(x)$ is real, and scales as $\exp(-\Delta N \beta)$ where Δ is a positive constant. Thus, the average sign decays exponentially with volume and inverse temperature thus making simulations exponentially unstable. This corresponds to the so-called minus-sign problem, which restricts grand canonical QMC simulation of the doped Hubbard model to *small* lattice sizes and *high* temperatures. With the above approach and when the average sign is not too small, one can compute imaginary time displaced correlation functions and directly determine the conductivity tensor at finite matsubara frequencies. However, at *low* temperatures and strong coupling ($U/t > 8$) uncontrollable fluctuations occur in $\sigma_{x,y}$ before the sign problem becomes serious.

We thus consider an alternative way of computing the current-current correlation functions at finite Matsubara frequencies. The starting point is to define the imaginary time propagator:

$$U_\epsilon(\beta,0) = T\exp\left(-\int_0^\beta \mathrm{d}\tau \;\left(H_\epsilon(\tau)-\mu N\right)\right) \;\text{ with }\; H_\epsilon(\tau) = H - \epsilon e^{i\omega_m\tau} j_\alpha. \quad (1.36)$$

Here, T denotes the time ordering. With this definition, one has:

$$\frac{\partial}{\partial\epsilon}\left.\frac{\mathrm{Tr}\left[U_\epsilon(\beta,0)j_\gamma\right]}{\mathrm{Tr}\left[U_\epsilon(\beta,0)\right]}\right|_{\epsilon=0} = \int_0^\beta e^{i\omega_m\tau}\langle j_\alpha(\tau)j_\gamma(0)\rangle. \quad (1.37)$$

As in Eq. (1.33), for a given value of ϵ one may carry out a HS transformation of the Hubbard interaction, integrate over the fermionic degrees of freedom to obtain:

$$\lim_{\epsilon\to 0}\frac{1}{\epsilon}\left[\frac{\sum_x \det\left[M(\epsilon,x)\right] j_\gamma(\epsilon,x)}{\sum_x \det\left[M(\epsilon,x)\right]} - \frac{\sum_x \det\left[M(x)\right] j(x)}{\sum_x \det\left[M(x)\right]}\right] = \int_0^\beta e^{i\omega_m\tau}\langle j_\alpha(\tau)j_\gamma(0)\rangle. \quad (1.38)$$

In principle one could carry out two independent QMC simulations to estimate the left hand side of the above equation. However, one notes that:

$$\sum_x \det\left[M(\epsilon,x)\right] \equiv \mathrm{Tr}\left[U_\epsilon(\beta,0)\right] = \mathrm{Tr}\left[U(\beta,0)\right] + O(\epsilon^2) \quad (1.39)$$

since the linear term in ϵ contains a prefactor $\int_0^\beta e^{i\omega_m\beta}$ which vanishes since $\omega_m = 2\pi m/\beta$. Thus, we can write:

$$\begin{aligned}\int_0^\beta e^{i\omega_m\tau}\langle j_\alpha(\tau)j_\gamma(0)\rangle &= \frac{\sum_x \det\left[M(x)\right] A(x)}{\sum_x \det\left[M(x)\right]} \;\text{ with}\\ A(x) &= \lim_{\epsilon\to 0}\frac{1}{\epsilon}\left[\frac{\det\left[M(\epsilon,x)\right]}{\det\left[M(x)\right]} j_\gamma(\epsilon,x) - j_\gamma(x)\right]. \end{aligned} \quad (1.40)$$

We then use Eq. (1.35) to calculate the above expression where we have identify $A(x)$ to the observable $O(x)$. In the case where both methods are stable identical results are obtained (See Fig. 1.2).

1.4 Numerical results and discussion

We first consider the weak coupling case, $U/t = 4$. Fig. 1.3 plots $R_H(B, i\omega_m)$ on a 6×6 lattice and at $\beta t = 5$ [2]. Similar results were obtained on 4×4 lattices.

[2] We have checked that presence of the magnetic field does not effect in a significant way the magnitude of the Hubbard gap and antiferromagnetic spin-spin correlations at half-band filling and $U/t = 4$.

Since the magnetic field is scaled as $Ba^2/\Phi_0 = 1/L^2$ no spurious are present due to a too large value of B. One may see that the QMC results compare well with the $U/t = 0$ value of R_H (solid lines) for all considered band fillings. At the considered temperature, R_H shows no singular behavior as the Mott transition is approached (i.e. $\langle n \rangle \rightarrow 1$). This stands in agreement with the QMC calculation of the charge susceptibility by Furukawa et al. [6] which supports the picture of a Mott transition driven by the divergence of the effective mass.

We now consider the strong coupling Hubbard model, $U/t > 8$, where the mapping onto the t-J model with $J = 4t^2/U$ is valid. Fig. 1.4a plots $R_H^\star$ for several choices of U/t and as a function of temperature. We consider the filling $\langle n \rangle = 0.95$. Although we cannot reach temperatures $T \ll J$ due to the sign problem, the general features of the data show that there is an intermediate temperature regime where $R_H^\star$ is positive (hole-like). At high and low temperatures, $R_H^\star$ is negative (electron-like). We may classify the data by considering three temperature regimes: i) $T > U$. Here, correlation effects may, to a first approximation, be neglected: $R_H^\star$ is negative and scales to its free electron value. ii) $J < T < U$. In this temperature regime, the energy scale J is hidden by thermal fluctuations. This may be confirmed by considering antiferromagnetic spin-spin correlations $S(\pi,\pi) = \frac{4}{3}\sum_{\vec{j}} \exp\left(i\vec{Q}\vec{j}\right) \langle \vec{S}(\vec{j}) \cdot \vec{S}(\vec{0}) \rangle$ where $\vec{Q} = (\pi,\pi)/a$ and $\vec{S}(\vec{j})$ is the spin operator on site $\vec{j}$. As may be seen from Fig. 1.4b $S(\pi,\pi)$ takes values independent of $J = 4t^2/U$ in the considered temperature regime. Hence, for $J < T < U$ the physics of the Hubbard model is related to that of the $U = \infty$ Hubbard model. We can make contact to the work of Shastry et al. [59] who have calculated $R_H^\star$ for the t-J model only in the region $T > J$ by a high temperature expansion. Before comparing results, we note that Shastry et al. [59] perform their calculations within the projected Hilbert space of no double occupancy. Hence, Eq. (1.10) corresponds to frequencies $\omega \gg J$ but $\omega \ll U$. Fig. 1.4a shows a hole-like $R_H^\star$ for $J < T < U$. One also notes that $R_H^\star$ decreases as $T \rightarrow J$. These results are consistent with Ref. [59]. As mentioned above, in the considered temperature range, we expect the Hubbard model to share some similarity with the $U = \infty$ model. For the latter model, the first contribution in a high temperature expansion of $R_H^\star$ yields,

$$R_H^\star = \frac{a}{ec}\left(\frac{1}{4}\frac{n}{1-n} - \frac{1-n}{n}\right) + O(\beta^4) \tag{1.41}$$

and thus a hole-like Hall coefficient for $n > 2/3$ [59]. We note that in the case of spinless fermions, the calculation which lead to the above result yields a very similar expression:

$$R_H^\star = \frac{a}{ec}\left(\frac{n}{1-n} - \frac{1-n}{n}\right) + O(\beta^4) \tag{1.42}$$

and thus a hole-like Hall coefficient for $n > 1/2$. iii) $T < J$. The energy scale J may be singled out by considering the antiferromagnetic spin-spin correlations (Fig.

3b). As apparent from Figs. 1.4a and 1.4b, the reduction of $R_H^\star$ is directly related to the enhancement of $S(\pi,\pi)$ at $T \lesssim J$. A natural extrapolation of the results in Fig. 1.4 yields an electron-like $R_H^\star$ in the considered temperature regime.

Due to Eq. (1.11) we have an alternative way of computing $R_H^\star$ via the momentum distribution $n(\vec{k})$ at zero magnetic field. Fig. 1.5a plots $n(\vec{k})$ at $U/t = 10$ on a 10×10 lattice at band-filling $\langle n \rangle = 0.95$ and for temperatures ranging from $T/t > J$ to $T/t < J$. From this data, and the use of equation (1.11) we may estimate $R_H^\star$ (triangles in Fig. 1.5b). For comparison we plot (solid circle in Fig. 1.5b) $R_H^\star$ as obtained on a 6×6 lattice at finite magnetic field (see Eq. 1.10). Within the errorbars, the results are identical thus showing that our calculations are not plagued by uncontrolled finite-size effects. Strictly speaking, both approaches yield identical results only in the thermodynamic limit.

The density dependence of $R_H^\star$ is given in Fig. 1.6 at $U/t = 16$, $\beta t = 1$ ($J < T < U$), $U/t = 12$, $\beta t = 1.35$ ($J < T < U$), $\beta t = 3.5$ ($T < J, U$), and $U/t = 12$, $\beta t = 5$ ($T < J, U$). At those temperatures, no finite size effects are observed. Since we have not projected out the upper-Hubbard band, particle-hole symmetry present at half-band filling leads to the vanishing of the Hall coefficient at any frequency. At small densities, $R_H^\star$ scales to it's free electron value: $R_H^\star \sim -1/n$. The maximal value of $R_H^\star$ is approximately located at $\langle n \rangle = 0.95$ which is the density considered in Fig. 3. As the temperature is lowered, the density interval for which $R_H^\star$ is hole-like, as well as the magnitude of $R_H^\star$ diminishes. At lower temperatures, we expect $R_H^\star$ to be negative. Apart from the vanishing of $R_H^\star$ at half-band filling due to particle-hole symmetry, the data in the temperature regime $J < T < U$ show the same overall structure as observed in Ref. [59].

We have up till now considered frequencies $\omega_m \gg U, t$. Figs. 1.7 to 1.9 plot R_H as well as D_{xx} in Eq. (1.8) at finite Matsubara frequencies for several choices of U/t and temperatures. The data is organized as follows. In Fig. 1.7 we are well in the temperature range $T > J$. Fig. 1.8 corresponds to temperature slightly larger than J and Fig. 1.9 to $T < J$. Upon analysis of low temperature data, (see Figs. 1.8 and 1.9) one may see that no finite size effects are observable within the obtained accuracy. Since the magnetic field is scaled as $Ba^2/\Phi_0 = 1/L^2$, no spurious effects due to too large values of B are present. Several points may be made: i) Extrapolating $D_{xx}(i\omega_m)$ to zero frequency yields $D\hbar^2/\pi e^2$ where D is the Drude weight [3,4]. Taking our lowest temperature data (see Fig. 1.9) a linear extrapolation yields a Drude weight in agreement with independent zero temperature calculations of Dagotto et al. [64]. ii) The temperature dependence of the Hall coefficient, is much larger than for D_{xx}. In the temperature regime $T < J$ (Fig. 1.9) R_H is negative for all considered Matsubara frequencies. R_H decreases with decreasing ω_m but retains small amplitude comparable to $a^2/\langle n \rangle |e| c$. A similar behavior is seen at slightly higher temperature (see Fig. 1.8). iii) On the contrary, in the temperature regime $J < T < U$, R_H is positive and increases considerably with decreasing Matsubara frequencies ($U/t = 16$, $T/t = 1$ in Fig 1.7). It is interesting to consider the data for $U/t = 12$. At $T/t = 1$ (Fig. 1.7) R_H is positive. As the temperature is lowered to $T/t = 1/2$ (Fig. 1.8) one may see an explicit sign change in R_H at small Matsubara frequencies. From Figs. 1.7 to 1.9, one may conclude that at lower Matsubara frequencies the overall temperature dependence of the sign of R_H is similar to $R_H^\star$. However, the quantitative magnitude of R_H is frequency dependent.

The comparison of the present results with experiments on cuprates relies on the assumption that the Hall coefficient at high ($\omega > 1/\tau$) and low ($\omega < 1/\tau$) frequencies show similar behaviors. This assumption fails, in the interpretation of recent AC Hall measurements on high-T_c cuprates [65] in terms of two relaxation rates [66] or in terms of $\vec{k}$ dependent relaxation rate [67]. Under the above assumption, our results at $T < J$ are consistent with experiments on cuprates at *high* temperatures. At low temperatures, the Hall coefficient in $La_{2-x}Sr_xCuO_4$ is hole-like and scales as $1/x$ for $x < 0.3$ [68, 69]. When the temperature is increased, R_H, is strongly suppressed at an energy scale T_H which coincides roughly with T_χ [70]. Here, T_χ corresponds to the temperature scale where the uniform spin susceptibility shows a maximum. Both T_χ and T_H have the same x dependence. Above T_H, the Hall coefficient scales to a small temperature independent value satisfying the Luttinger volume [71,72]. T_χ as well as T_H are temperature scales we have not yet reached with numerical simulations of the Hubbard model. The role of the spin-gap on the Hall coefficient has been examined in Ref. [73] for ladder topologies. Below the spin-gap temperature, a Hall coefficient with large magnitude is observed.

In summary, we have presented numerical results which support that the high frequency Hall coefficient for the weak-coupling Hubbard model is electron like with small amplitude at small hole-doping. In the strong-coupling regime where the Hubbard model may be approximately mapped onto the t-J model, the sign of the Hall coefficient was found to be strongly temperature dependent at small hole-doping: hole-like for $J < T < U$, electron-like with small amplitude for $T < J$ and $T > U$. The overall features of those results were found to be valid at infinite and finite Matsubara frequencies, thus lending support that in the limit $\omega << U, t, J$ but $\omega > 1/\tau$ the Hall coefficient shows a similar temperature and doping behavior as $R_H^\star$. Our results are consistent with the high temperature expansion of Shastry et al. [59] for the t-J model at $i\omega_m \to \infty$ and in the temperature region $J < T < U$. We have been able to reach lower temperatures, $T < J = 4t^2/U$ for values of $U/t > 8$, and found R_H to change from hole-like to electron-like as the temperature scale J is crossed.

From the above, we conclude that our results are in agreement with the picture of a Mott transition driven by the divergence of the effective mass as opposed to the vanishing of the density of charge carriers.

1.5 Figures

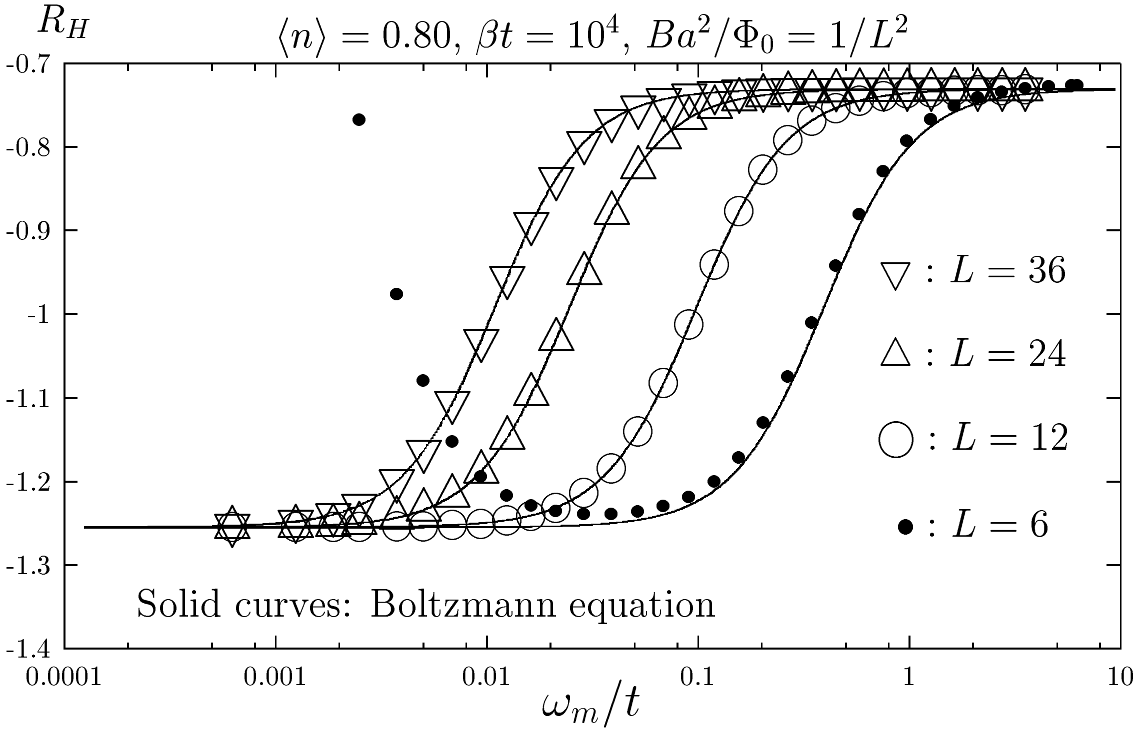

Figure 1.1: $R_H(B, i\omega_m)$ in units of $a^2/|e|c$ for free electrons. Solid curves show solutions of the Boltzmann transport equation for magnetic fields set to $Ba^2/\phi_0 = 1/L^2$ where from right to left, $L = 6, 12, 24, 36$. The symbols correspond to R_H obtained within the Kubo formalism on an $L \times L$ lattice. Here, the magnetic field is scaled as $Ba^2/\phi_0 = 1/L^2$.

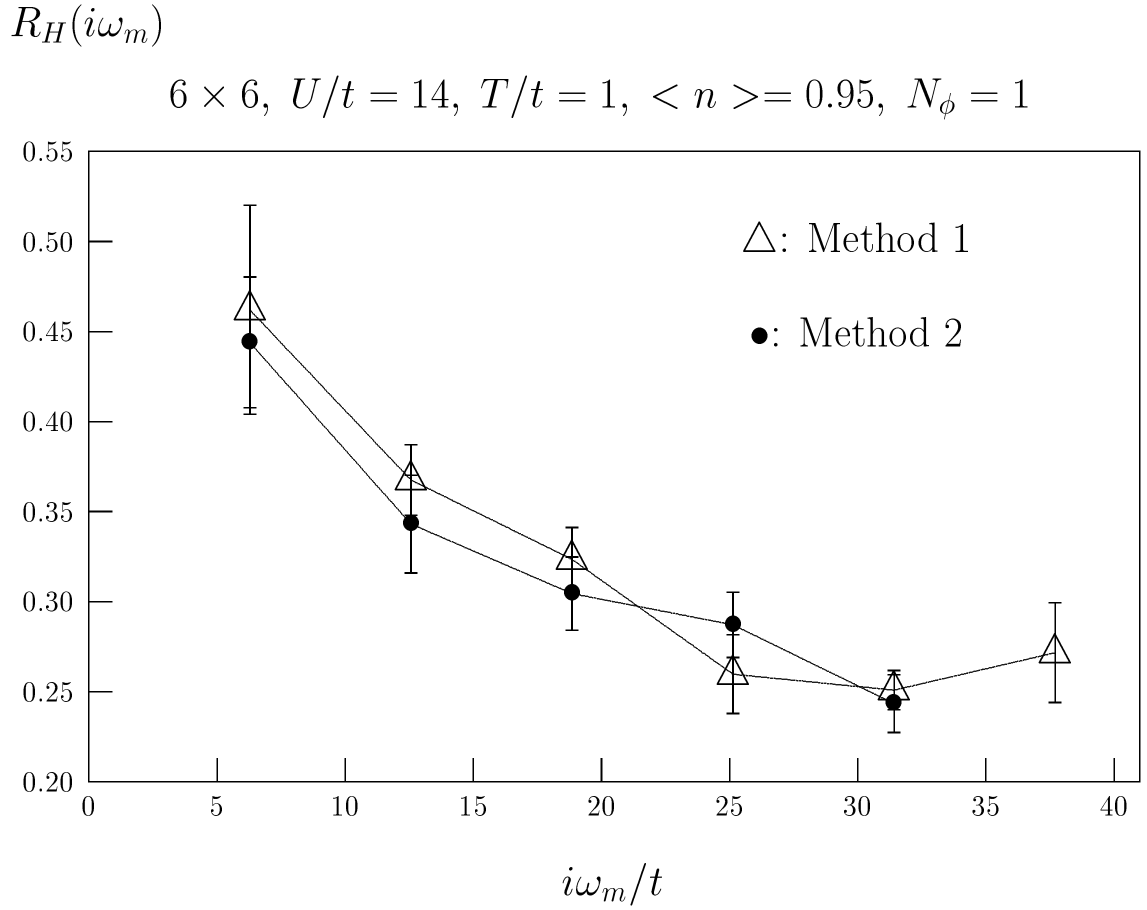

Figure 1.2: Hall coefficient in units of $a^2/|e|c$ computed in two different ways. Method 1) explicit calculation of imaginary time displaced correlation functions. Method 2) is based on Eq. (1.40). At lower temperatures, Method 1) shows uncontrollable fluctuations, whereas Method 2) is stable.

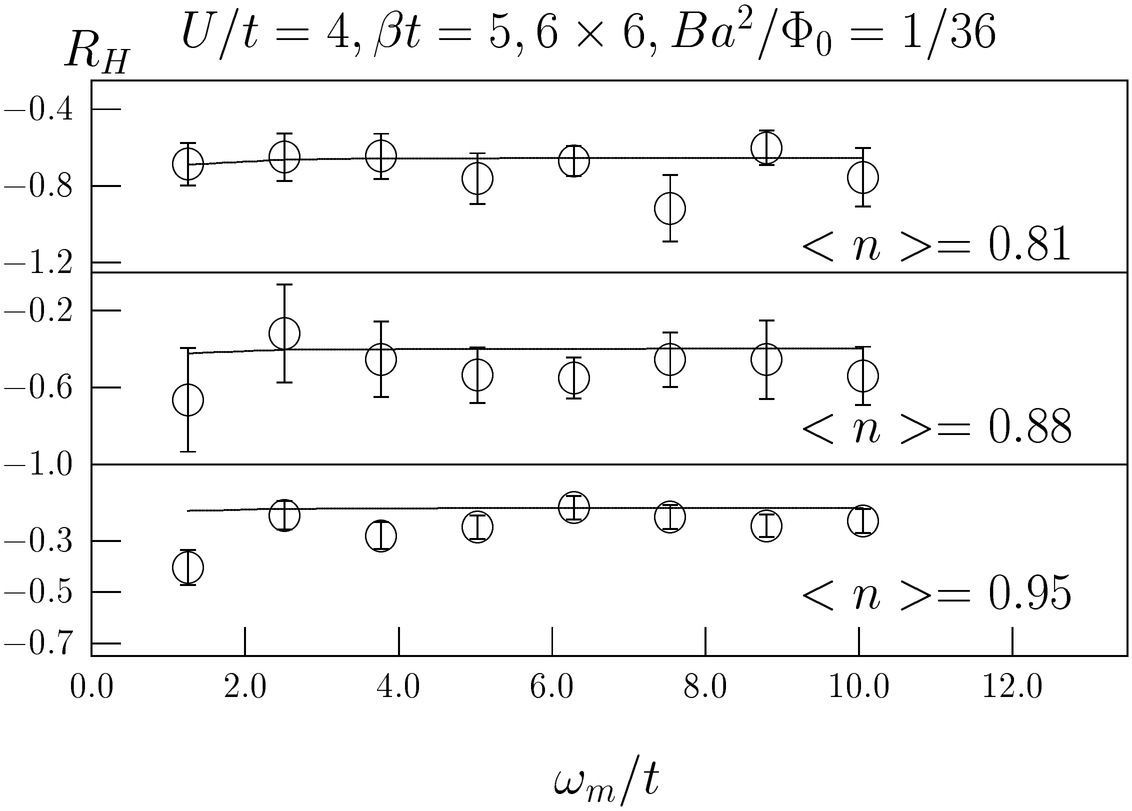

Figure 1.3: $R_H(B, i\omega_m)$ in units of $a^2/|e|c$ for the weak coupling Hubbard model (open circles). Solid lines correspond to the $U/t = 0$ values of $R_H(B, i\omega_m)$.

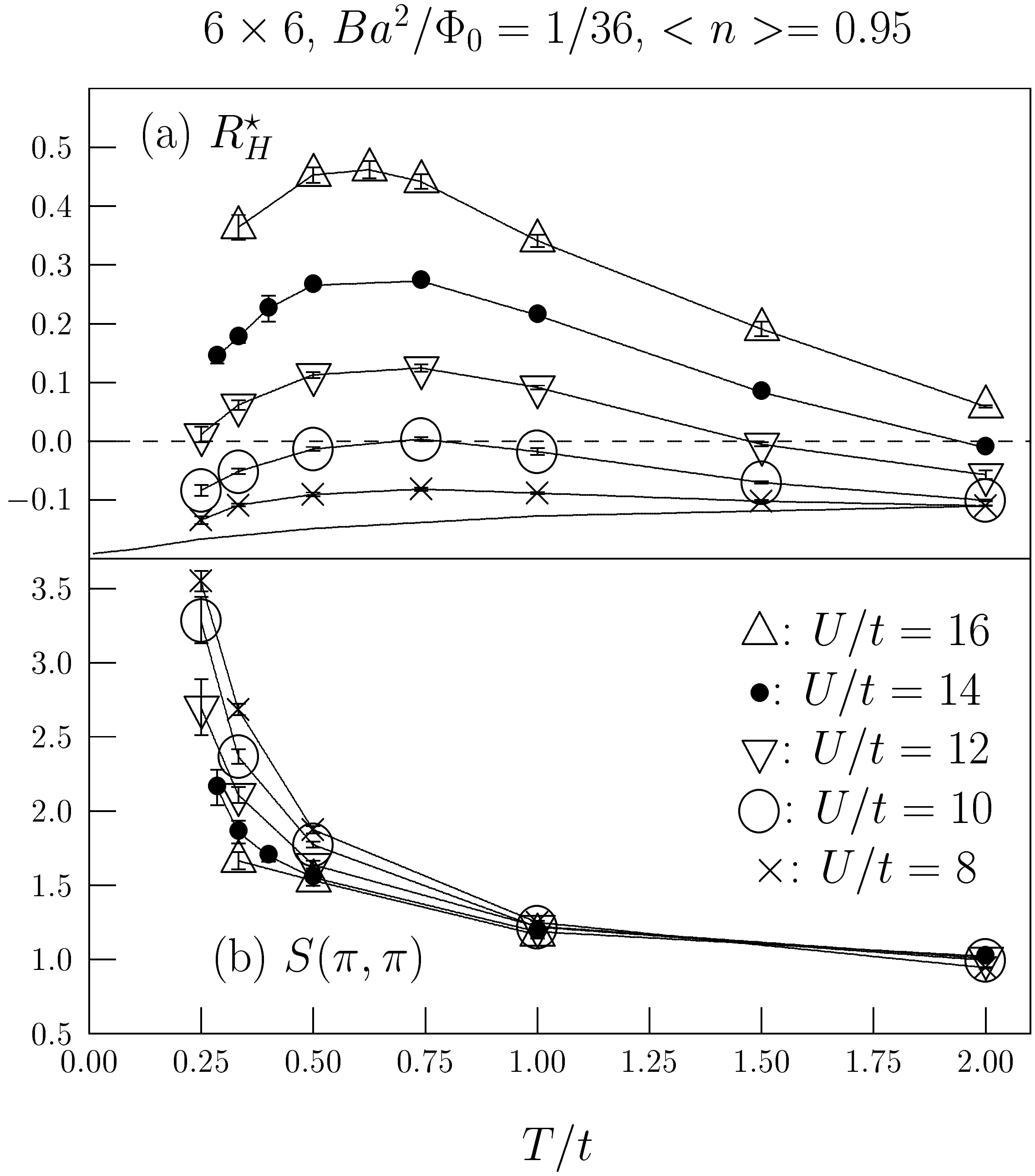

Figure 1.4: a) $R_H^\star$ as a function of temperature for the strong coupling Hubbard model. Solid line with no symbols corresponds to the $U/t = 0$ value of $R_H^\star$. b) Antiferromagnetic spin-spin correlations for the Hubbard model as a function of temperature.

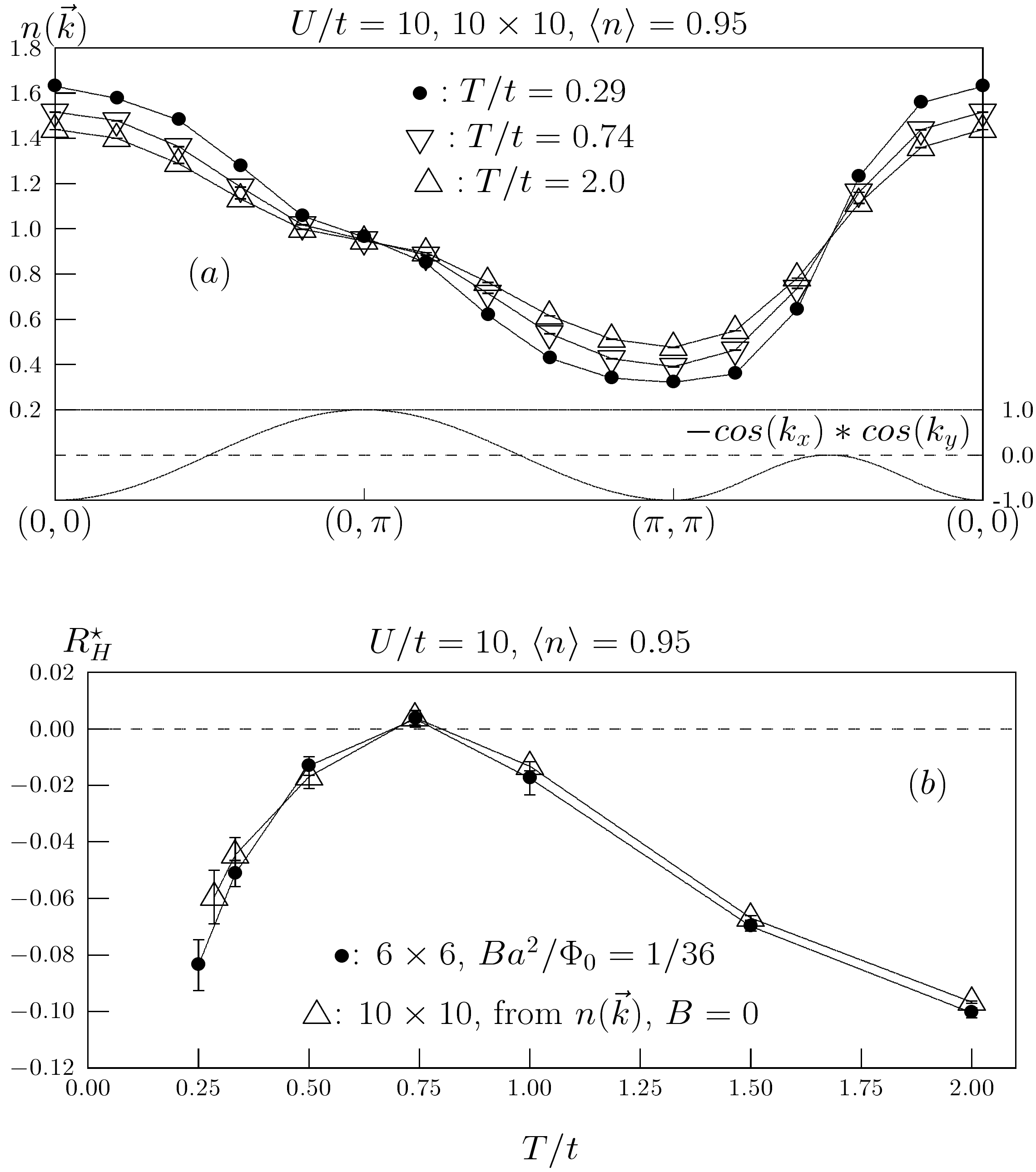

Figure 1.5: (a) Momentum distribution, $n(\vec{k})$, for the Hubbard model at $U/t = 10$, $\langle n \rangle = 0.95$, on a 10×10 lattice for temperatures ranging from $T > J$ to $T < J$. We also plot the function $cos(k_x)cos(k_y)$ which determines the positive and negative contributions to $R_H^\star$ (see Eq. (1.11)). (b) $\bullet$: $R_H^\star$ as obtained on a 6×6 lattice at finite magnetic field (see Eq. (1.10)). $\triangle$: $R_H^\star$ as obtained from $n(\vec{k})$ with the use of Eq. (1.11)

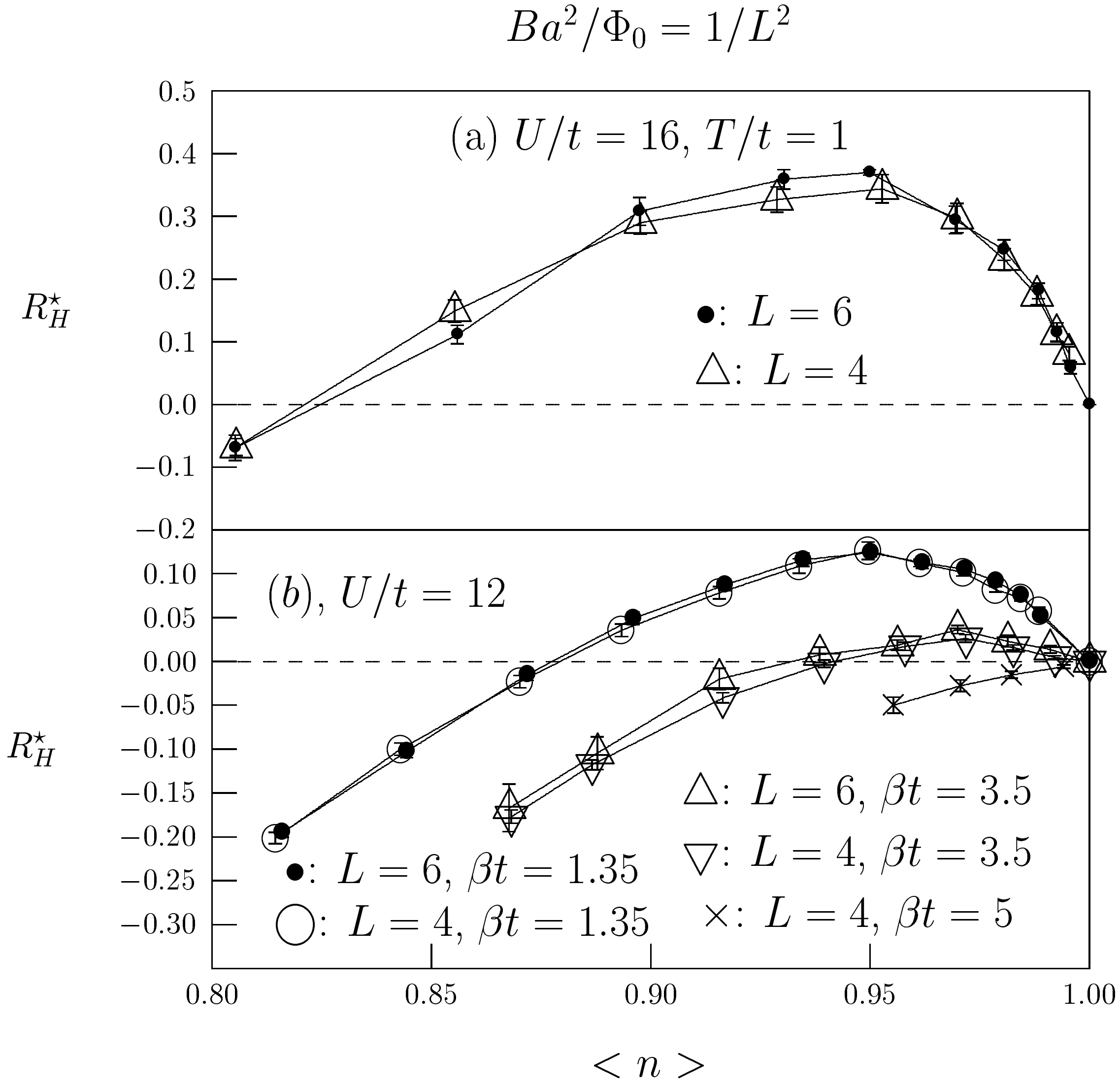

Figure 1.6: Density dependence of $R_H^\star$ for the strong coupling Hubbard model. Apart from the lowest temperature data we consider 4×4 and 6×6 lattices to show the absence of size effects. In terms of T/J, the data corresponds to (a) $T/J = 4$ (b) $\bullet$,$\bigcirc$: $T/J = 2.2$, $\triangle$,$\bigtriangledown$: $T/J = 0.86$, $\times$: $T/J = 0.6$.

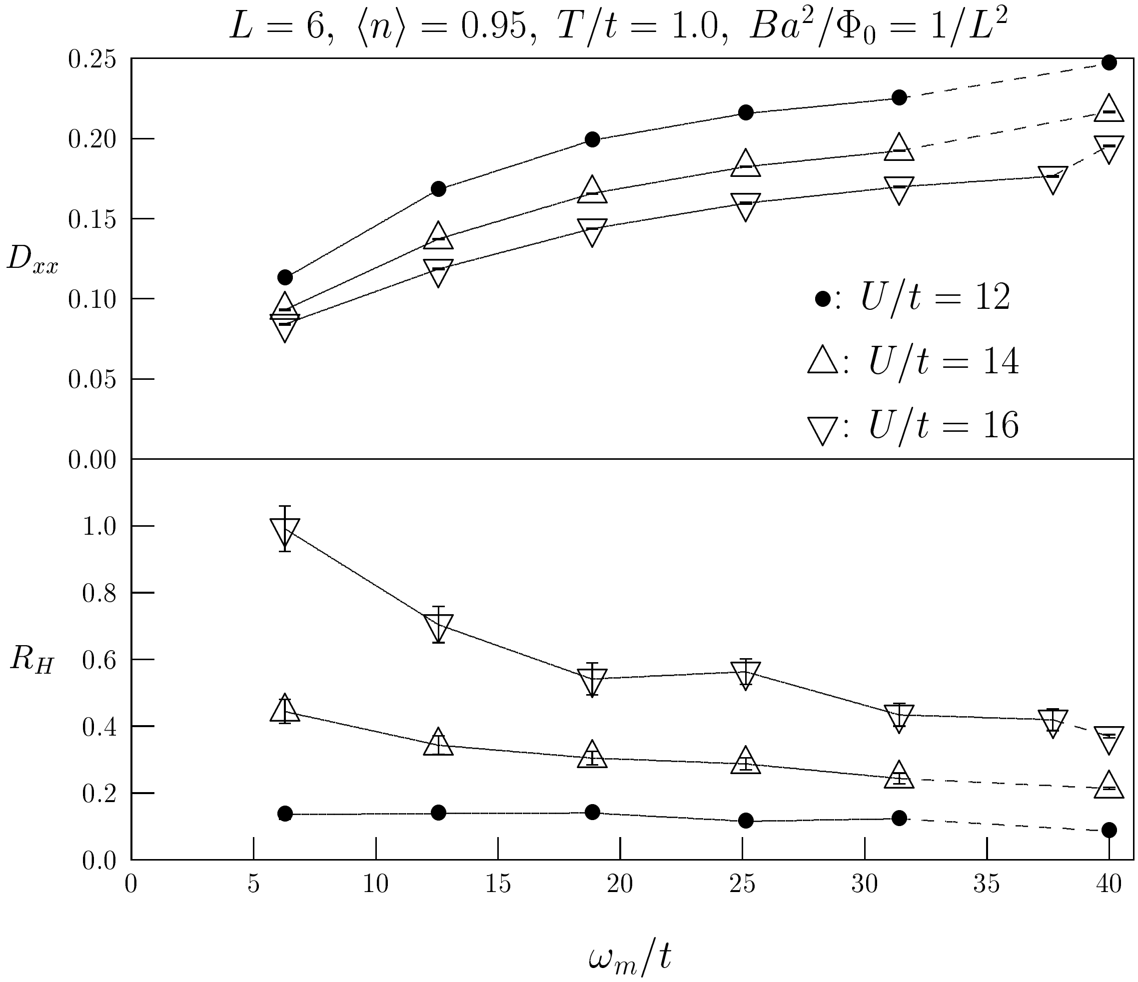

Figure 1.7: D_{xx} and R_H in the strong coupling regime. Here we fix the temperature to $T/t = 1$ and consider various values of U/t. As a function of T/J where $J = 4t^2/U$ the data corresponds to $\bullet$: $T/J = 3$, $\triangle$: $T/J = 3.5$, and ∇: $T/J = 4$.

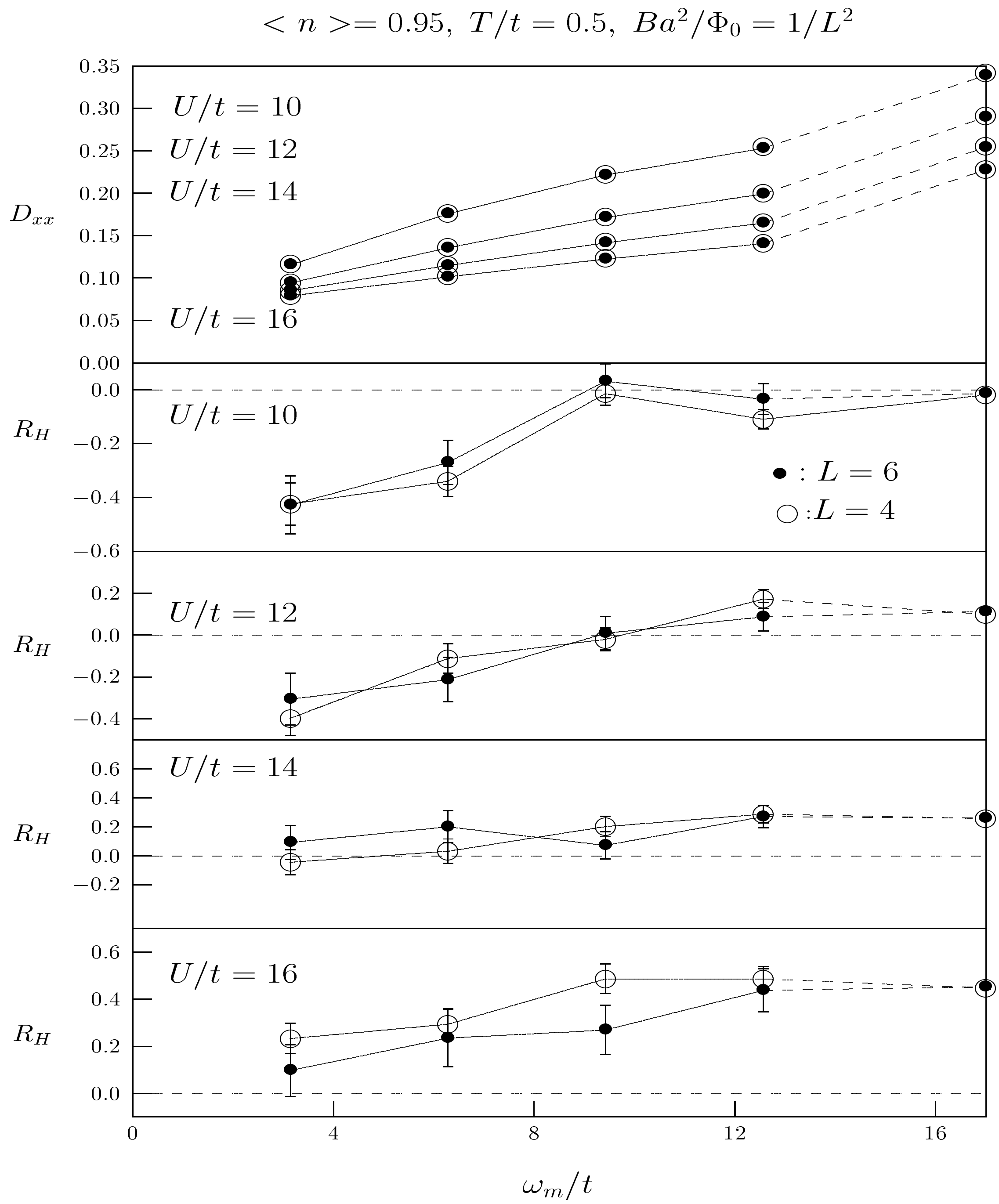

Figure 1.8: D_{xx} and R_H in the strong coupling regime. As seen from the figure, the data does not suffer from size effects since the both the 4×4 and 6×6 lattices produce indistinguishable results. In terms of T/J where $J = 4t^2/U$ the data corresponds to $T/J = 2$ ($U/t = 16$), $T/J = 1.75$ ($U/t = 14$), $T/J = 1.5$ ($U/t = 12$) and $T/J = 1.25$ ($U/t = 10$).

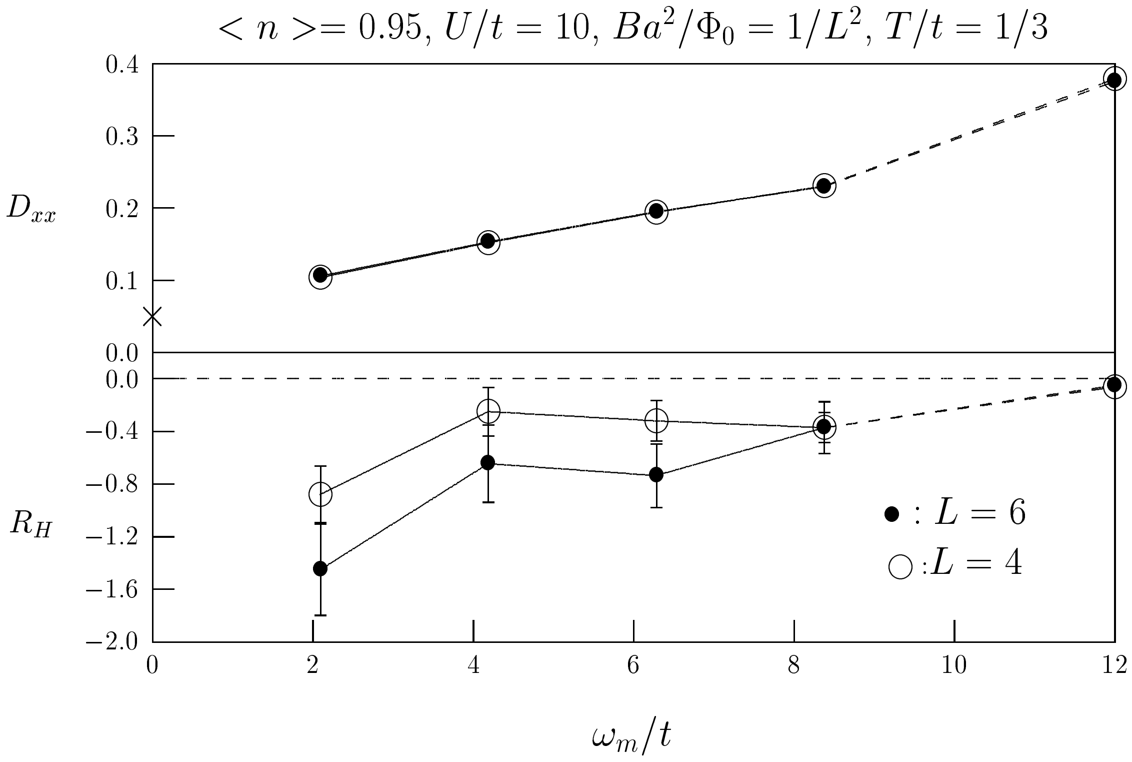

Figure 1.9: D_{xx} and R_H in the strong coupling regime. The cross at $i\omega_m = 0$ corresponds to $D\hbar^2/\pi e^2$ as obtained from Ref. [64]. In terms of T/J where $J = 4t^2/U$ the data corresponds to $T/J = 0.83$.

Chapter 2

Insulator-Metal Transition in the One and Two-Dimensional Hubbard Models

At zero-temperature a continuous metal-insulator transition driven by a change in chemical potential may be characterized by the critical behavior of the compressibility, χ_c, or of the Drude weight, D. In the Mott insulating phase both D and χ_c vanish while they remain finite in the metallic phase [2, 40]. In order to describe the metal-insulator transition from the insulator side, we propose to consider the zero-temperature Green function:

$$iG(\vec{r},\omega) = \sum_{\sigma} \int \mathrm{d}t e^{i\omega t} \langle \Psi_0 | T c_{\sigma,\vec{r}}(t) c^{\dagger}_{\sigma,\vec{0}}(0) | \Psi_0 \rangle \tag{2.1}$$

where $|\Psi_0\rangle$ corresponds to the ground state of the insulator. The notation is standard [74]. At *long* distances, $|\vec{r}|$, and for frequencies ω within the charge gap the Green function is real and satisfies:

$$G(\vec{r},\omega) \sim e^{-|\vec{r}|/\xi_l}. \tag{2.2}$$

The insulator-metal transition may then be characterized by the critical behavior of ξ_l as the critical chemical potential, μ_c, is approached from the insulating phase:

$$\xi_l \sim |\omega - \mu_c|^{-\nu}. \tag{2.3}$$

The advantage of this approach, lies in the fact that ξ_l may be computed with QMC methods free of the minus-sign problem (see Sec. 1.3). This enables us to reach lattice sizes up to 16×16 at zero temperature. In order calculate the Green function in the insulating state, we have generalized the PQMC algorithm to compute imaginary time zero temperature Green in a numerically stable way for *large* imaginary times. This algorithm will be reviewed in Chap. 4. The central result of this chapter is summarized by:

$$\nu = 0.26 \pm 0.05 \text{ and } \mu_c/t = 0.67 \pm 0.015 \tag{2.4}$$

for the two-dimensional Hubbard model, at $U/t = 4$. Here, the Hubbard model is defined by:

$$H = -t \sum_{\langle \vec{i},\vec{j} \rangle,\sigma} \left(c^{\dagger}_{\vec{i},\sigma} c_{\vec{j},\sigma} + \text{H.c.} \right) + U \sum_{\vec{i}} (n_{\vec{i},\uparrow} - \frac{1}{2})(n_{\vec{i},\downarrow} - \frac{1}{2}) \tag{2.5}$$

and energy values are measured from the particle-hole symmetric point: $\mu = 0$. We consider periodic boundary conditions. In contrast, the generic band insulator-metal transition [1] in all dimensions as well as the Mott transition in the 1D Hubbard model satisfies $\xi_l \sim |\omega - \mu_c|^{-\nu}$ with $\nu = 1/2$ [40]. This result points out the anomalous character of the metal-insulator transition in the two-dimensional Hubbard model. The chapter is organized as follows. In the next section, we discuss the implicit assumptions involved in defining the localization length and give some explicit examples as well as a simple physical interpretation of ξ_l. We will then in section 2.2 describe in detail our numerical calculation of ξ_l for the one and two-dimensional Hubbard models. Section 2.3 will be devoted to a toy-model capable of reproducing the the numerical result. The essential ingredient of this toy model is the occurrence of flat bands with dispersion $|\vec{k}|^4$. In Sec. 2.4 we will present numerical results for $A(\vec{k}, \omega) \equiv \text{Im}G(\vec{k}, \omega)$ on a 16×16 lattice which support the existence of the above mentioned flat bands. Our results are summarized and put into the context of a scaling assumption in the last section.

2.1 The localization length: ξ_l

The localization length is based on the knowledge of the zero temperature single-particle Green function in the insulating state. That $G(\vec{r}, \omega) \sim \exp -|\vec{r}|/\xi_l$ with $\xi_l \sim |\omega - \mu_c|^{-\nu}$ for values of ω within the charge gap relies on some assumptions.
i) The insulating state, is defined by the vanishing of the Drude weight or charge stiffness, D. The models we consider are particle-hole symmetric at $\mu = 0$ and thus, the critical chemical potential, μ_c, at which the transition occurs is defined by:

$$D(\mu) = 0 \text{ for } |\mu| < \mu_c \tag{2.6}$$

For the range of chemical potentials for which the Drude weight vanishes, we will assume that the charge susceptibility equally vanishes:

$$\chi_c(\mu) \equiv \frac{\partial n(\mu)}{\partial \mu} = 0 \text{ for } |\mu| < \mu_c. \tag{2.7}$$

[1] Our working definition of the generic band metal-insulator transition is the one realized at $\mu = \pm\delta$ in the band structure given by Eq. 1 in the Introduction

This excludes the possibility of localized states within the charge gap as defined by the vanishing of the Drude weight. The occurrence of localized states within the charge gap could happen in the presence of disorder.
ii) Our approach is based on the knowledge of the single-particle Green function. Thus, we have to assume that the quasiparticle gap, $\Delta_{qp} = \lim_{N\to\infty} E_0^{N+1} - E_0^N$, satisfies:

$$\Delta_{qp} = \mu_c \tag{2.8}$$

Here, N denotes the number of sites of the considered square lattice and E_0^N is the ground state energy in the N-particle Hilbert space. In the case of an insulator to s-wave superconductor transition, the difference between Δ_{qp} and μ_c is of the order of the superconducting gap at the critical chemical potential. In this case, the insulator-superconductor transition, should be studied with the two-particle Green function. In the case of a transition between an insulator and d-wave superconductor the nodes in the superconducting gap lead to $\Delta_{qp} = \mu_c$. In the case of a insulator-metal transition where the metallic state is described by a Fermi liquid, the relation $\mu_c = \Delta_{qp}$ clearly holds.

We now give some explicit examples. The tight-binding model

$$H = -t \sum_{\langle \vec{i},\vec{j}\rangle,\sigma} c^{\dagger}_{\vec{i},\sigma} c_{\vec{j},\sigma} \tag{2.9}$$

is diagonal in Fourier space, and has single particle energies given by $\epsilon_{\vec{k}} = -2t(\cos(\vec{k}\vec{a}_x) + \cos(\vec{k}\vec{a}_y))$, $\vec{a}_x$, $\vec{a}_y$ being the lattice constants. We consider the filled band, $\langle n \rangle = 2$. At zero temperature, an insulator-metal transition will occur at $\mu_c = 4t$. For frequencies $\omega > \mu_c = 4t$, the zero-temperature Green function (see Eq. 2.1) is given by:

$$G(\vec{r},\omega) = \frac{2}{N} \sum_{\vec{k}} \frac{e^{i\vec{k}\vec{r}}}{\epsilon_{\vec{k}} - \omega} \tag{2.10}$$

where N denotes the number of sites of the square lattice and the factor 2 corresponds to the summation over the spin degrees of freedom. Numerically, one obtains: $G(\vec{r},\omega) \sim e^{-|\vec{r}|/\xi_l}$ with $\xi_l \sim |\omega - \mu_c|^{-1/2}$. For the generic dispersion relation $\epsilon_{\vec{k}} = \frac{\vec{k}^2}{2m}$ the integration may be done analytically to obtain the result $\xi_l \sim |\omega - \mu_c|^{-1/2}$, with $\mu_c = 0$. This result is valid in all dimensions.

The physical interpretation of ξ_l is facilitated by considering the single impurity Hamiltonian (Fano-Anderson model) [74, 75]:

$$H = \sum_{\vec{k}} \epsilon_k c^{\dagger}_{\vec{k}} c_{\vec{k}} + \epsilon_b b^{\dagger} b + \frac{t_b}{\sqrt{N}} \sum_{\vec{k}} \left(c^{\dagger}_{\vec{k}} b + b^{\dagger} c_{\vec{k}} \right). \tag{2.11}$$

Here, $b^{\dagger}$ creates an electron in the impurity state at the origin and energy ϵ_b. The hybridization between the localized state and the band electrons alters the energy of the impurity level to the value: $E_b = \epsilon_b + \frac{t_b^2}{N}\sum_{\vec{k}} \frac{1}{E_b - \epsilon_{\vec{k}}}$. We will assume $E_b > \epsilon_{\vec{k}}$ for all $\vec{k}$. When all single particle states of the valence band are filled and the impurity single particle state empty, the probability amplitude of transferring a band electron at site $\vec{r}$ to the impurity state is:

$$\frac{\langle \Psi_0 | b^\dagger c_{\vec{r}} | \Psi_0 \rangle}{\langle \Psi_0 | \Psi_0 \rangle} = -\alpha(E_b) \frac{t_b}{N} \sum_{\vec{k}} \frac{e^{i\vec{k}\vec{r}}}{\epsilon_{\vec{k}} - E_b} \tag{2.12}$$

where the normalization factor is given by $\alpha^{-1}(E_b) = 1 + \frac{t_b^2}{N}\sum_{\vec{k}} \frac{1}{(E_b - \epsilon_{\vec{k}})^2}$. Comparison between equations (2.12) and (2.10) show that the spatial dependence of the two quantities is identical. ξ_l may thus be interpreted as the localization length involved in transferring a particle over a distance $\vec{r}$ from the top of the valence band to an impurity state lying at energy E_b in the gap (i.e. $E_b > 4t$ in the above example).

We now consider the Hubbard model (Eq. 2.5) in a Hartree-Fock (HF) approximation with a spin density wave (SDW) ansatz. At half-band filling, QMC simulations show long-range antiferromagnetic order thus justifying:

$$\langle n_{\vec{i},\uparrow} \rangle + \langle n_{\vec{i},\downarrow} \rangle = 1 \ \text{ and } \ \langle n_{\vec{i},\uparrow} \rangle - \langle n_{\vec{i},\downarrow} \rangle = (-m)^{i_x + i_y}. \tag{2.13}$$

Writing $n_{\vec{i},\sigma} = \langle n_{\vec{i},\sigma} \rangle + \left(n_{\vec{i},\sigma} - \langle n_{\vec{i},\sigma} \rangle \right)$ and neglecting fluctuations terms: $\left(n_{\vec{i},\sigma} - \langle n_{\vec{i},\sigma} \rangle \right)$ $\left(n_{\vec{i},\sigma'} - \langle n_{\vec{i},\sigma'} \rangle \right)$ yields the mean-field Hamiltonian

$$\begin{aligned} H_{HF} &= \sum_{\vec{k} \epsilon MBZ, \sigma} E_+(\vec{k}) \gamma^\dagger_{\vec{k},\sigma} \gamma_{\vec{k},\sigma} + E_-(\vec{k}) \eta^\dagger_{\vec{k},\sigma} \eta_{\vec{k},\sigma} \\ \begin{pmatrix} c^\dagger_{\vec{k},\sigma} \\ c^\dagger_{\vec{k}+\vec{Q},\sigma} \end{pmatrix} &= \begin{pmatrix} \cos(\Theta_{\vec{k},\sigma}) & \sin(\Theta_{\vec{k},\sigma}) \\ -\sin(\Theta_{\vec{k},\sigma}) & \cos(\Theta_{\vec{k},\sigma}) \end{pmatrix} \begin{pmatrix} \gamma^\dagger_{\vec{k},\sigma} \\ \eta^\dagger_{\vec{k},\sigma} \end{pmatrix}, \\ \mathrm{tg}(2\Theta_{\vec{k},\sigma}) &= \frac{Um\sigma}{2\epsilon_{\vec{k}}}, \quad E_\pm = \pm\sqrt{\Delta^2 + \epsilon^2_{\vec{k}}}, \quad \Delta = \frac{Um}{2}. \end{aligned} \tag{2.14}$$

where the $\vec{k}$ summation runs over the magnetic Brillouin zone (MBZ). Self consistency yields the gap equation at $T = 0$,

$$1 = \frac{U}{2N} \sum_{\vec{k} \epsilon MBZ, \sigma} \frac{1}{\sqrt{\Delta^2 + \epsilon^2_{\vec{k}}}}. \tag{2.15}$$

$\Delta = \frac{Um}{2}$ corresponds to the charge gap and the ground state is an insulator for

$$|\mu| < \mu_c \equiv \Delta \tag{2.16}$$

The single particle Green function at distance $\vec{R} = (L/2, L/2)$ on an $L \times L$ lattice and at $-\mu_c < \omega < \mu_c$ is given by:

$$G(\vec{R} = (L/2, L/2), \omega) = \frac{2}{N} \sum_{\vec{k} \epsilon MBZ} e^{i\vec{k}\vec{R}} \left(\frac{1}{E_+(\vec{k}) - \omega} + \frac{1}{E_-(\vec{k}) - \omega} \right) \tag{2.17}$$

Numerically and as shown in Fig. 2.1 $G(\vec{R} = (L/2, L/2), \omega) \sim e^{-|R|/\xi_l}$ with $\xi_l \sim |\omega - \mu_c|^{-1/2}$. This result is independent on the presence of perfect-nesting: $\epsilon(\vec{k}) = -\epsilon(\vec{k} + (\pi, \pi))$. Adding a hopping matrix element between sites separated by the vector (a, a) where a denotes the lattice constant yields the same exponent for the localization length.

2.2 Numerical calculation of ξ_l for the 1D and 2D Hubbard models

To obtain an estimate of the critical exponent ν for the Hubbard model, we require an accurate determination of the critical chemical potential, μ_c, as well as of the localization length, ξ_l. Both quantities may be obtained from the knowledge of:

$$G_\sigma(\vec{r}, \tau) = \Theta(\tau) \frac{\langle \Psi_0 | c_{\vec{r},\sigma}(\tau) c^\dagger_{\vec{0},\sigma} | \Psi_0 \rangle}{\langle \Psi_0 | \Psi_0 \rangle} - \Theta(-\tau) \frac{\langle \Psi_0 | c^\dagger_{-\vec{r},\sigma}(-\tau) c_{\vec{0},\sigma} | \Psi_0 \rangle}{\langle \Psi_0 | \Psi_0 \rangle}, \tag{2.18}$$

where $c_{\vec{r},\sigma}(\tau) = e^{\tau H} c_{\vec{r},\sigma} e^{-\tau H}$. Here $|\Psi_0\rangle$ denotes the ground state of the half-filled ($\mu = 0$) Hubbard Hamiltonian (2.5). The above quantity may be efficiently calculated with QMC methods. Since we are at half-band filling, the sign problem does not occur and we are able to consider lattice sizes up to linear dimension $L = 16$, namely $N = 16 \times 16$ without any serious difficulties. The calculation of imaginary time Green function in the zero-temperature auxiliary field QMC algorithm [48–50] was first reported by Deisz et al. [76]. However, their approach does not incorporate a numerical stabilization scheme and they are thus restricted to small values of τ (i.e. $\tau t \sim 2.5$). Based on ideas used for the stabilization of finite temperature QMC algorithms [12], we have developed a numerically stable QMC algorithm for the calculation of $G_\sigma(\vec{r}, \tau)$. The details of this algorithm may be found Chap. 4.

From the knowledge of $G_\sigma(\vec{r}, \tau)$ on an N-site lattice, we may obtain an estimate of the charge gap. We denote by $|\Psi_n^N\rangle$ the eigenvector of the Hamiltonian H with eigenvalue E_n^N in the N-particle Hilbert space. With this notation,

$$G(\vec{r} = 0, \tau) \equiv \sum_\sigma G_\sigma(\vec{r} = 0, \tau) = \frac{1}{N} \sum_{n, \vec{i}, \sigma} |\langle \Psi_0^N | c_{\vec{i},\sigma} | \Psi_n^{N+1} \rangle|^2 \exp\left(-\tau \left(E_n^{N+1} - E_0^N\right)\right). \tag{2.19}$$

for $\tau > 0$. Fig. 2.2, plots $G(\vec{r}=0,\tau)$ for a 16×16 lattice at $U/t=4$. We may obtain a reliable estimate of the charge gap for this lattice size by fitting $G(\vec{r}=0,\tau)$ to the form $e^{-\Delta_{qp}\tau}$ with $\Delta_{qp} \equiv E_0^{N+1} - E_0^N$ for *large* values of τ. Fig. 1b shows Δ_{qp} as a function of linear lattice size. The data points for lattice sizes ranging from 4×4 to 16×16 fit very well a $1/L$ form which we use to extrapolate to the thermodynamic limit to obtain: $\Delta_{qp}/t = 0.67 \pm 0.015$. This result stands in good agreement with the quoted result of Furukawa and Imada [6]: $\Delta_{qp}/t = 0.58 \pm 0.08$. Since in the notation of equation (2.5) the Hubbard model satisfies particle-hole symmetry at $\mu = 0$, the critical chemical potential is nothing but the charge gap: $\mu_c \equiv \Delta_{qp}$.

For frequencies within the charge gap, $|\omega| < \mu_c$, the zero temperature Green function is real and may be obtained through the relation:

$$G(\vec{r},\omega) = -\int_{-\infty}^{\infty} \mathrm{d}\tau G(\vec{r},\tau)e^{\tau\omega}. \tag{2.20}$$

The Green function $G(\vec{r},\tau)$ is computed at half-band filling where the sign problem is not present and the statistical uncertainty does not grow exponentially with lattice size. However, since we are multiplying the QMC data by the factor $e^{\tau\omega}$, the statistical uncertainty will grow exponentially with increasing values of τ for $\tau\omega > 0$. For each lattice size L, we have considered the largest distance $\vec{r} = (L/2, L/2)$. For this distance, $G(\vec{r} = (L/2, L/2), \tau)$ is plotted in Fig. 2.3. Due to particle-hole symmetry at $\mu = 0$, $G(\vec{r} = (L/2, L/2), \tau) = -G(\vec{r} = (L/2, L/2), -\tau)$. For the imaginary time integration, (see equation (2.20)) and frequencies $|\omega| < 0.65t$, a cutoff of $\tau t = 10$ proved to be sufficient for the determination of the Green function (see Fig. 2.4). $G(\vec{r} = (L/2, L/2), \omega)$ as a function of lattice size is plotted in Fig. 2.4 for several values of ω. For lattice sizes ranging from $L = 6$ to $L = 16$, an exponential decay may be seen within the quoted statistical uncertainty. From this data, we obtain an estimate of the localization length ξ_l. With the above determined value of μ_c, we plot $|\omega - \mu_c|$ versus ξ_l (see Fig. 2.5) on a log-log plot. For all considered chemical potentials, $\xi_l/a < 8\sqrt{2}$ which corresponds to our largest considered distance ($L = 16$). The slopes in Fig. 2.5 correspond to values of the critical exponent $\nu = 1/2$ and $\nu = 1/4$. The QMC data is consistent with $\nu = 1/4$ and seems to rule out the possibility $\nu = 1/2$. A statistical analysis yields: $\nu = 0.26 \pm 0.05$.

To confirm the validity of our approach, we consider the Mott transition in the 1D Hubbard model at $U/t = 4$. A similar QMC calculation as described above for the 2D case yields a value of the correlation length exponent consistent with $\nu = 1/2$ (see Fig. 2.6). We obtain $\mu_c/t = 0.66 \pm 0.015$ which is consistent with the exact result of Lieb and Wu [1]: $\mu_c/t = 0.643$. Chains of linear length up to $L = 24$ were considered.

2.3 A toy model.

In a single particle picture, the above result, $\xi_l \sim |\omega - \mu_c|^{-1/4}$ for the two-dimensional Hubbard model may be understood by assuming that doped holes initially occupy regions in the Brillouin zone which are governed by a $|\vec{k}|^4$ dispersion relation. Here, we construct a toy model which produces those flat bands around the $(\pm\pi, 0)$, $(0, \pm\pi)$, points in the Brillouin zone, as well as hole-pockets at the $(\pm\pi/2, \pm\pi/2)$ $\vec{k}$-vectors. Depending upon which structure dominates the low energy physics, the nature of the metal-insulator transition will be radically altered.

The toy model we consider describes the motion of a hole in an antiferromagnetic background:

$$H(R) = H_t(R) + J \sum_{\langle \vec{i}, \vec{j} \rangle} S^z_{\vec{i}} S^z_{\vec{j}}. \tag{2.21}$$

$H_t(R)$ corresponds to single particle processes and we impose the constraint of no double occupancy. In the limit of large J/t and at half-band filling, Ising antiferromagnetic order is generated. In this limit, a doped hole can only hop within the same sublattice since hopping between different sublattices will frustrate the magnetic background and thus cost an energy J. For purposes of discussion, we consider the special form:

$$\begin{aligned} -H_t(R) = \quad & \frac{5}{2} H_{(1,1)} - \frac{1}{4} H_{(1,3)} + (2R-1) H_{(2,0)} + (\frac{3}{8} - R\frac{6}{8}) H_{(2,2)} + (\frac{1}{16} - \frac{R}{8}) H_{(4,0)} \\ + \quad & N(\frac{41}{4} - R\frac{18}{4}) \end{aligned} \tag{2.22}$$

where,

$$\begin{aligned} H_{(1,1)} = \sum_i \quad & (c_i^\dagger c_{i+a_x+a_y} + h.c.) + (c_i^\dagger c_{i+a_x-a_y} + h.c.) \\ H_{(1,3)} = \sum_i \quad & (c_i^\dagger c_{i+3a_x+a_y} + h.c.) + (c_i^\dagger c_{i+3a_x-a_y} + h.c.) + \\ & (c_i^\dagger c_{i+a_x+3a_y} + h.c.) + (c_i^\dagger c_{i-a_x+3a_y} + h.c.) \\ H_{(2,0)} = \sum_i \quad & (c_i^\dagger c_{i+2a_x} + h.c.) + (c_i^\dagger c_{i+2a_y} + h.c.) \\ H_{(2,2)} = \sum_i \quad & (c_i^\dagger c_{i+2a_x+2a_y} + h.c.) + (c_i^\dagger c_{i+2a_x-2a_y} + h.c.) \\ H_{(4,0)} = \sum_i \quad & (c_i^\dagger c_{i+4a_x} + h.c.) + (c_i^\dagger c_{i+4a_y} + h.c.). \end{aligned} \tag{2.23}$$

Here we have omitted the spin indices and set the hopping matrix element to unity. The dispersion relation of the doped hole is then given by:

$$\begin{aligned} -E(R, \vec{k}) \;=\; & (2 - \cos(k_x) - \cos(k_y + \pi))^2 \, (2 - \cos(k_x + \pi) - \cos(k_y))^2 - \\ & R\left((\sin(k_x) - \sin(k_y))^4 + (\sin(k_x) + \sin(k_y))^4 \right) \end{aligned} \tag{2.24}$$

and is plotted at three different values of R in Fig. 2.7. Several points may be made.
i) $R < 1$. In this case $E(R, \vec{k})$ takes its maximum at the $(0, \pm\pi)$, $(\pm\pi, 0)$ points in the Brillouin zone. A doped hole will initially occupy those regions and the dispersion relation around those points satisfies a $|\vec{k}|^4$ law. One may check explicitly that this leads to the exponent $\nu = 1/4$ as observed in our QMC calculations.
ii)$R > 1$. $E(R, \vec{k})$ takes is maximum at $\vec{k} = (\pm\pi/2, \pm\pi/2)$ so that doped holes will initially occupy those regions. Around those points the dispersion relation is quadratic leading to an exponent $\nu = 1/2$. (This corresponds to the the hole-pocket scenario [35, 77])
iii) $R = 1$. $E(\vec{k})$ is maximal and vanishes on the line defined by: $\cos(k_x) + \cos(k_y) = 0$. This situation is very similar to the case of the Hartree-Fock approximation with a SDW ansatz discussed in section 2.1. In fact, expanding $E(R = 1, \vec{k})$ around $\vec{k} = (0, \pi)$ yields,

$$E(R = 1, (0, \pi) + (\Delta k_x, \Delta k_y)) \sim [(\Delta k_x + \Delta k_y)(\Delta k_x - \Delta k_y)]^2 . \qquad (2.25)$$

Precisely the same result is obtain from the quasiparticle energy $E(\vec{k})$ obtained in the HF-SDW approximation. As in the HF-SDW approximation at $R = 1$, we obtain $\nu = 1/2$.

2.4 Single particle excitations in the half-filled Hubbard model

With the Maximum Entropy method [51, 52] method, we can invert the equation

$$\sum_\sigma G_\sigma(\vec{k}, \tau) = \frac{1}{\pi} \int_{-\infty}^{0} \mathrm{d}\omega e^{-\tau\omega} A(\vec{k}, \omega) \quad \tau < 0, \qquad (2.26)$$

to obtain the spectral function $A(\vec{k}, \omega) \equiv \mathrm{Im}G(\vec{k}, \omega)$ from the zero temperature QMC data $G_\sigma(\vec{k}, \tau)$. At half-band filling, due to particle-hole symmetry $A(\vec{k}, \omega) \equiv A(\vec{k} + \vec{Q}, -\omega)$ with $\vec{Q} = (\pi, \pi)$. In Fig. 2.8 we plot $A(\vec{k}, \omega)$ at half-band filling, zero temperature, 16×16 lattice and $U/t = 4$. For each considered $\vec{k}$ we have normalized the data so as to set the maximum value of the spectral function to one. The normalization factor is listed on the right hand side of the figure. We note that around the $\vec{k} = (0, 0)$ point, the data of Fig. 2.8 shows a two peak structure observed at higher values of U/t, and at finite temperature by Preuss et al. [78]. Assuming the validity of the quasiparticle picture, we can define a quasiparticle energy, $E(\vec{k})$ via the peak position in $A(\vec{k}, \omega)$. One then recognizes a very flat dispersion relation around the $\vec{k} = (0, \pm\pi), (\pm\pi, 0)$ points. To illustrate this we have plotted in Fig. 2.9 $E(\vec{k})$ around $\vec{k} = (0, \pi)$ in the $(0, 1)$ direction. It is possible to fit the data over an acceptable range to a $|\vec{k}|^4$ form. For comparison, we have plotted the $U/t = 0$ dispersion relation. Similar results are found when scanning in the $(0,\pi)$ to (π,π) direction. The data is however less clear cut since in that direction, the single particle occupation number decreases rapidly thus leading to a signal with small amplitude. Some care has to be taken when trying to combine the concept of quasiparticles and flat bands with dispersion relation $|\vec{k}|^4$. Such flat bands produce substantial phase space for scattering processes which in turn may invalidate the concept of quasiparticles. In fact, photoemission data on insulating copper oxide $Sr_2CuO_2Cl_2$ [79, 80] shows a broad shoulder at wave vectors around $\vec{k} = (0,\pi)$ (See Fig. 2a in Ref. [80]). In contrast, at wave vectors $\vec{k} = (\pi/2, \pi/2)$ a well defined peak is observed. In trying to interpret the experimental data in terms of quasiparticles, one is lead to a very flat dispersion relation around $(0,\pi)$. However, this flat band lies $\sim 0.2eV$ below the value of $E(\vec{k} = (\pi/2, \pi/2))$. The origin of this effect is not clear, especially if one takes into account the uncertainty in assigning the peak value of the dispersion relation at $k = (0,\pi)$. An interpretation of this effect in terms of the interplay between short range antiferromagnetic correlations and hopping matrix elements has been proposed [80, 81].

2.5 Discussion and scaling theory of the metal-insulator transition

The central result of this chapter is summarized by the critical exponent $\nu = 1/4$ for the localization length in the two-dimensional Hubbard model. This stands in contrast to the generic band-metal insulator transition where $\nu = 1/2$ irrespective of dimensionality. In the framework of a single-particle picture, the exponent $\nu = 1/4$ may be understood by the existence of flat bands, with dispersion relation $|\vec{k}|^4$ around the $\vec{k} = (0, \pm\pi)$, $(\pm\pi, 0)$ points in the Brillouin zone. Doped holes predominantly occupy those regions which govern the low energy physics. With the use of the Maximum Entropy method to analytically continue the zero temperature Monte-Carlo data, we have computed $A(\vec{k}, \omega)$ for the half-filled case and obtained numerical support for the occurrence of those flat bands. The evolution of those flat bands under doping is a delicate issue. Finite temperature QMC calculation of $A(\vec{k}, \omega)$ in the doped phase show that the band structure evolves continuously with doping [36, 78]. There is considerable spectral weight transfer form the upper Hubbard band to the lower Hubbard band. Flat bands, flatter than the usual Van-Hove singularity, are still seen at finite doping around the $(0, \pm\pi)$, $(\pm\pi, 0)$ points in the Brillouin zone. Flat bands may in part be caused by strong scattering of the quasiparticle between $(\pi, 0)$ and $(0, \pi)$ by the antiferromagnetic fluctuation carrying momentum transfer (π, π) [82]. The flat dispersion thus generated further enhances this scattering channel in a consistent fashion. The experimental observation of flat bands, in high-T_c cuprates is documented in [37, 38, 83] [2].

Our results are best described under the assumption of hyperscaling [22,40] where it is postulated that the singular part of the free energy scales as $f_s(\Delta) = \Delta^{\nu(d+z)}$ and that there is a single relevant length scale ξ. Here, $\Delta \equiv |\mu - \mu_c|$ is related to the length scale $\xi \sim \Delta^{-\nu}$, d is the dimensionality and z the dynamical exponent. (For a recent review on continuous quantum phase transitions we refer the reader to Ref. [84]). Under the above assumptions, the charge susceptibility χ_c, charge stiffness D, and localization length ξ_l, satisfy:

$$\xi_l \sim \Delta^{-\nu}, \quad \chi_c \sim \Delta^{\nu(d-z)}, \quad D \sim \Delta^{\nu(d+z-2)}, \tag{2.27}$$

Since the control parameter, Δ, corresponds to the chemical potential, one obtains the additional constraint $\nu z = 1$ as well as $\delta \sim \Delta^{\nu(d+z)-1}$, δ being the doping concentration. Thus, in the case of a doping induced metal-insulator transition, there is only one free parameter. The generic band metal-insulator transition does satisfy the above assumption and belongs to the $z = 2$, $\nu = 1/2$ universality class. This is valid in all dimensions. The doping induce metal-insulator transition in the one-dimensional Hubbard model is characterized by: $\chi_c \sim |\mu - \mu_c|^{-1/2}$ [31], $D \sim \delta$ [32] and as shown numerically in this chapter $\xi_l \sim |\omega - \mu_c|^{-1/2}$. Those result are consistent with the hyperscaling assumption with exponents $\nu = 1/2$ and $z = 2$ for $d = 1$. For the two-dimensional Hubbard model at $U/t = 4$, we have two numerical results. The here presented localization length, $\xi_l \sim |\omega - \mu_c|^{-1/4}$ as well as the charge susceptibility which satisfies $\chi_c \sim |\mu - \mu_c|^{-1/2}$ [6]. Those results are consistent with the above scaling relations provided that $\nu = 1/4$ and $z = 4$. This novel universality class is characterized by a Drude weight satisfying $D \sim \delta^2$. On the other hand, the optical conductivity

$$\mathrm{Re}\sigma_{xx}(\omega) = D\delta(\omega) + \sigma_{xx}^{reg}(\omega) \tag{2.28}$$

(see Eq. 2 of the Appendix) satisfies the sum-rule

$$\int_{-\infty}^{\infty} \mathrm{Re}\sigma_{xx}(\omega) \sim -\langle K \rangle \tag{2.29}$$

where $\langle K \rangle$ denotes the kinetic energy. In the strong coupling limit one expects $\langle K \rangle \sim \delta$. Since $D \sim \delta^2$, most of the weight in the optical conductivity is not located in the low frequency coherent Drude response but in the incoherent response at higher frequencies. Recently, Tsunetsugu and Imada [39] have computed the quantity $D/\langle K \rangle$ for the t-J model on small clusters. Their result is consistent with $D/\langle K \rangle \sim \delta$ thus confirming the above scenario.

[2] The flat bands observed experimentally, are much flatter than the usual Van-Hove singularity. In Ref. [83] it has been argued that they yield a powerlaw singularity in the density of states.

Incoherence is one of the central properties of the metallic state in the vicinity of the metal-insulator transition. The toy model we have presented can indeed generate a $|\vec{k}|^4$ dispersion relation and thus satisfies the hyperscaling assumption with dynamical exponent $z = 4$. It however produces coherent transport since the current commutes with the Hamiltonian. [3] In trying to understand the metal-insulator transition in terms of a single-particle picture one is lead to further contradictions with the numerical data. In Chap. 1 we concluded that the *low* temperature high-frequency Hall coefficient showed no divergence at the metal-insulator transition. To reproduce this result in terms in our toy model, we have to assume $R = 1$ (See. Eq. 2.21 and Fig. 2.7). [4] This however yields $\nu = 1/2$ in contrast to the numerically observed $\nu = 1/4$.

[3]The toy model at $R < 1$ (See. Eq. 2.21) does produce, $D \sim \delta^2$. However, $\langle K \rangle \sim \delta^2$.

[4]For a dispersion relation $\epsilon(\vec{k}) = \alpha|\vec{k}|^\eta$ one may check within the Boltzmann transport equation that $R_H = 1/nec$ (See Eq. 1.30). Thus the toy model of Eqn. 2.21 produced a diverging Hall coefficient at the metal insulator transition for $R \neq 1$.

2.6 Figures

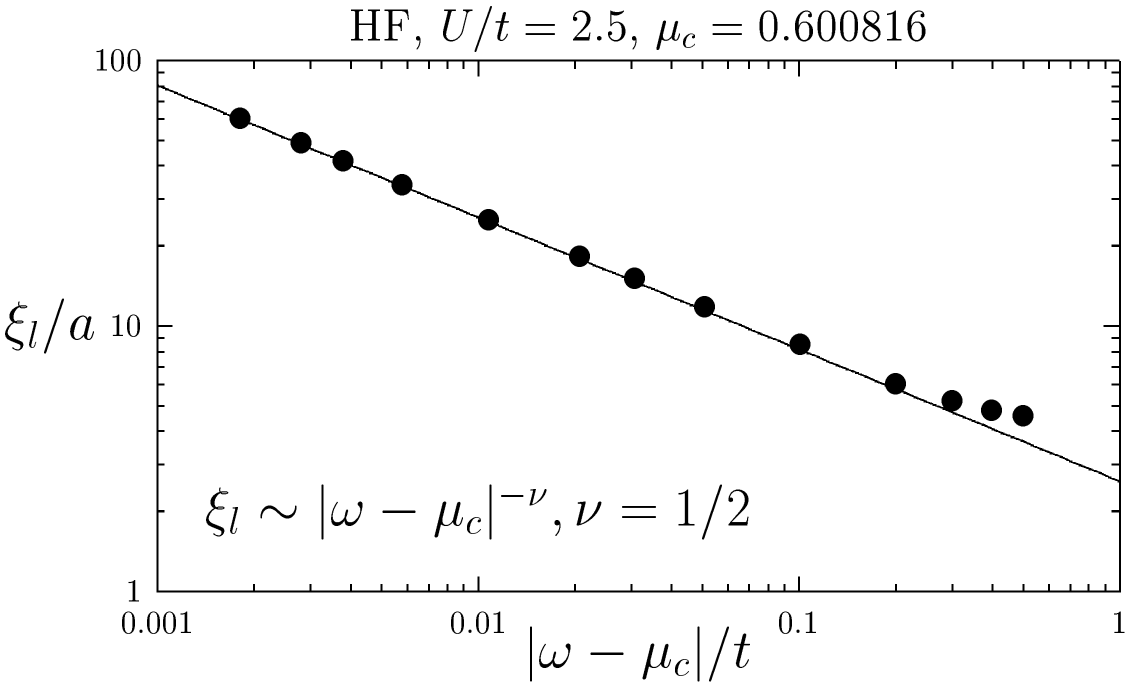

Figure 2.1: Localization lenght for the two-dimensional Hubbard model in the SDW approximation. The result is consistent with: $\xi_l \sim |\omega - \mu_c|^{-1/2}$.

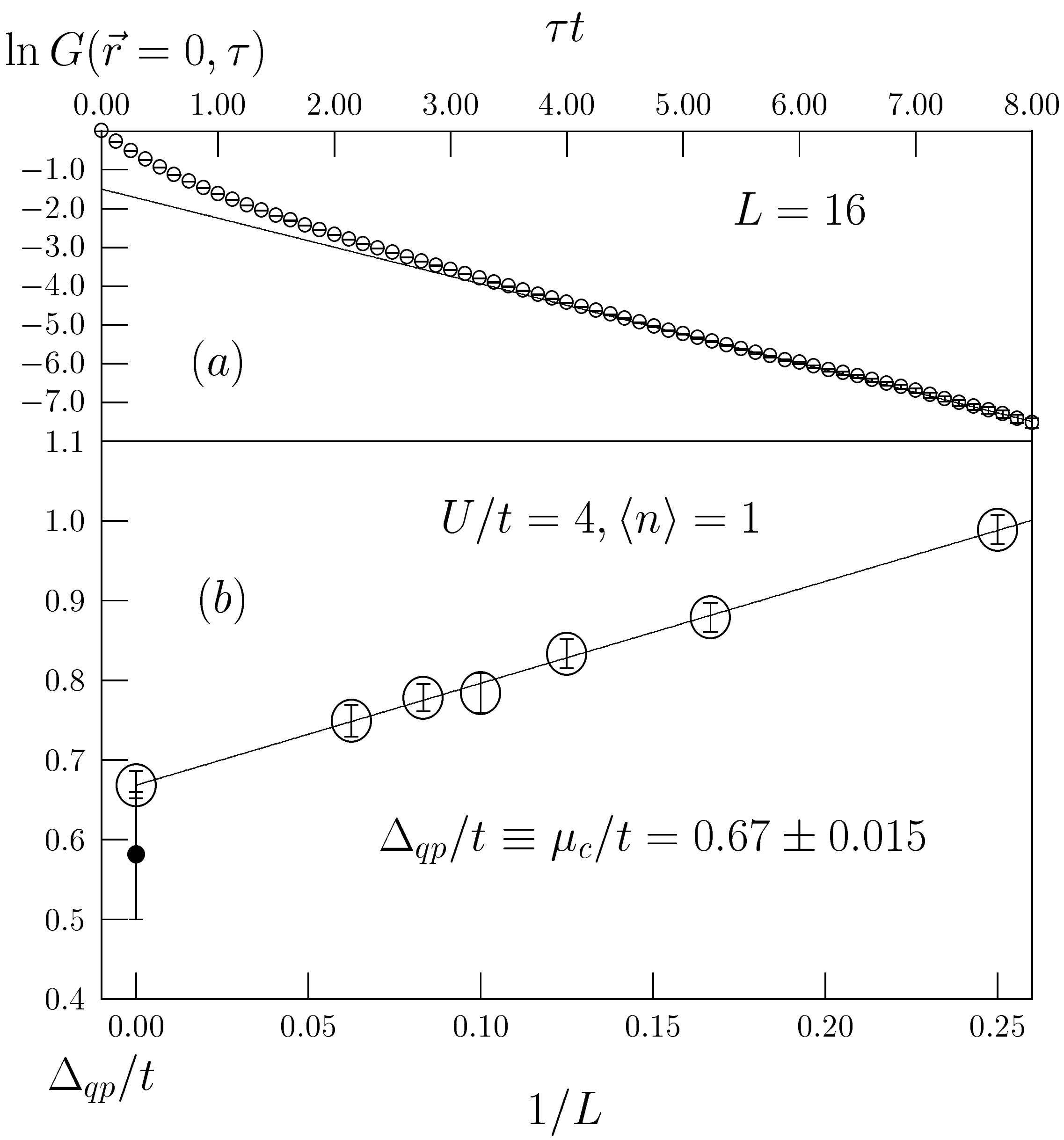

Figure 2.2: a) $\ln G(\vec{r}=0,\tau)$ as a function of τ for the half-filled ($\mu = 0$) 2D Hubbard model at $U/t = 4$ on a 16×16 lattice. The solid line corresponds to a least square fit of $G(\vec{r}=0,\tau)$ to the form $\exp(-\Delta_{qp}\tau)$ at *large* values of τ. b) Δ_{qp} as a function of linear lattice size L. The solid circle at $1/L = 0$ corresponds to Δ_{qp} as obtained in reference [6].

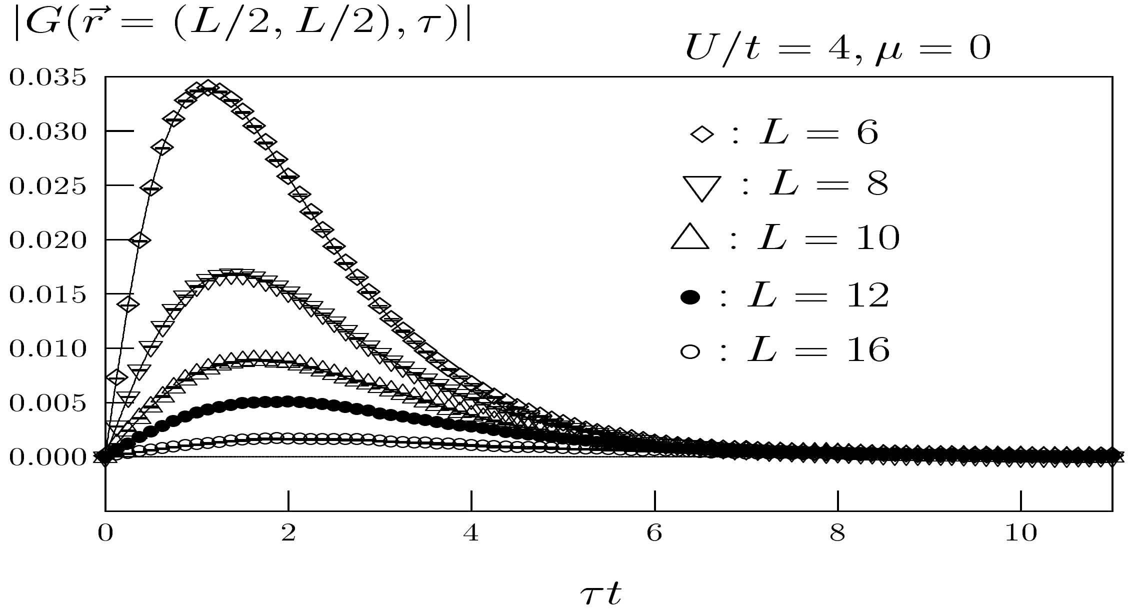

Figure 2.3: $|G(\vec{r} = (L/2, L/2), \tau)|$ as a function of system size and imaginary time τ for the 2D Hubbard model.

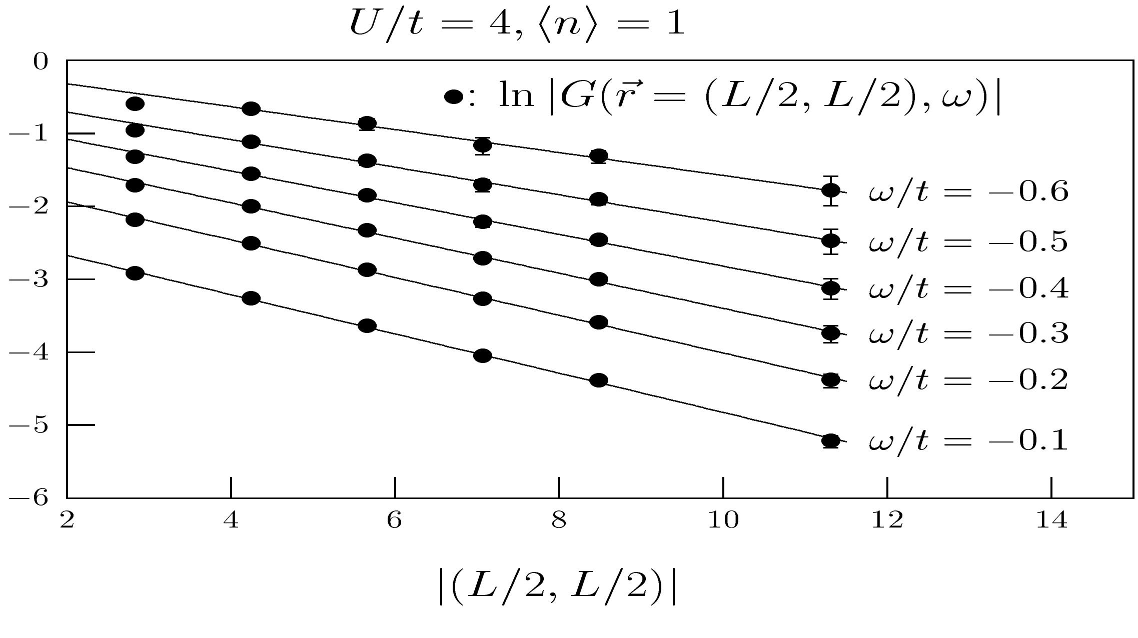

Figure 2.4: $\ln |G(\vec{R} = (L/2, L/2), \omega)|$ as a function of distance and chemical potential for the 2D Hubbard model. The solid lines correspond to a least square fit of $|G(\vec{R} = (L/2, L/2), \omega)|$ to the form $\exp\left(-|\vec{R}|/\xi_l\right)$ for $L > 4$.

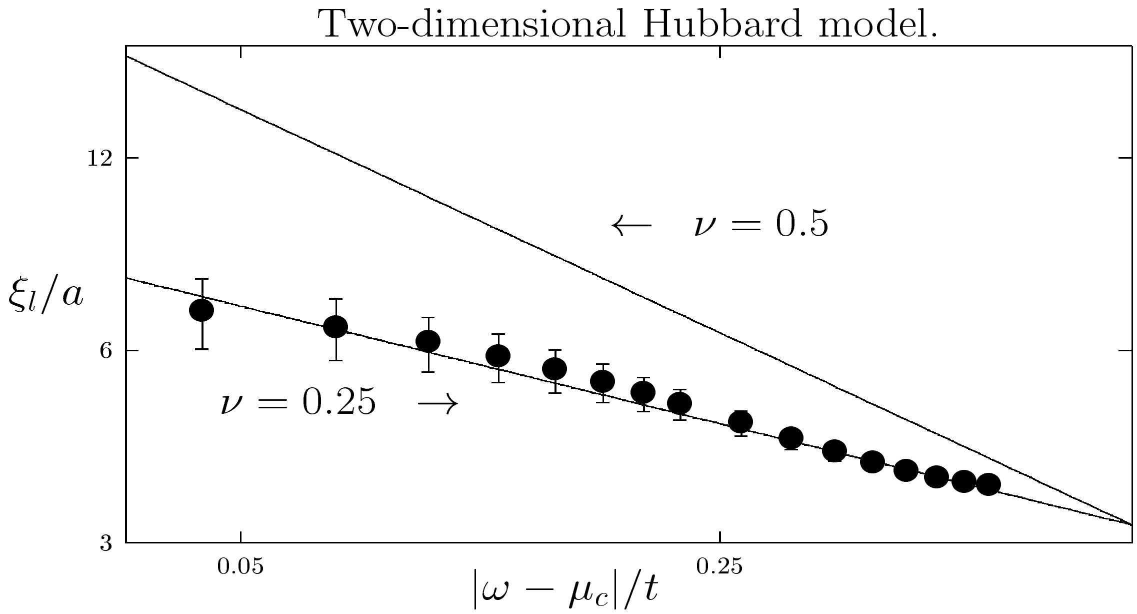

Figure 2.5: Localization length ξ_l versus $|\omega - \mu_c|$ for the 2D Hubbard model. The solid lines correspond to two values of the correlation length exponent: $\nu = 1/4$ and $\nu = 1/2$. The solid circles correspond to the QMC data.

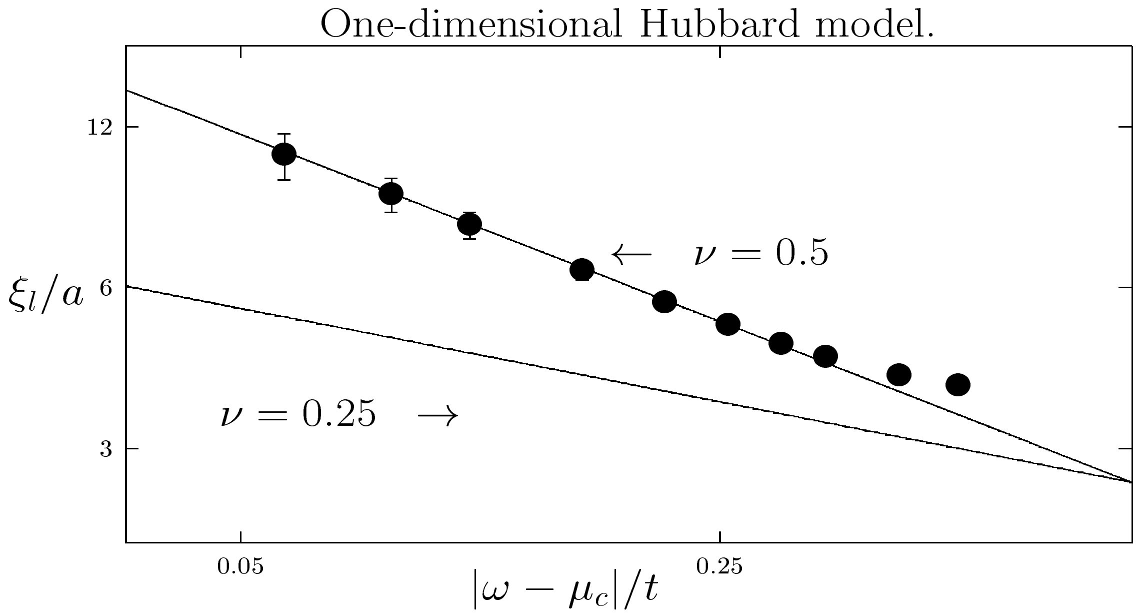

Figure 2.6: Same as Fig. 2.5 but for the 1D Hubbard model.

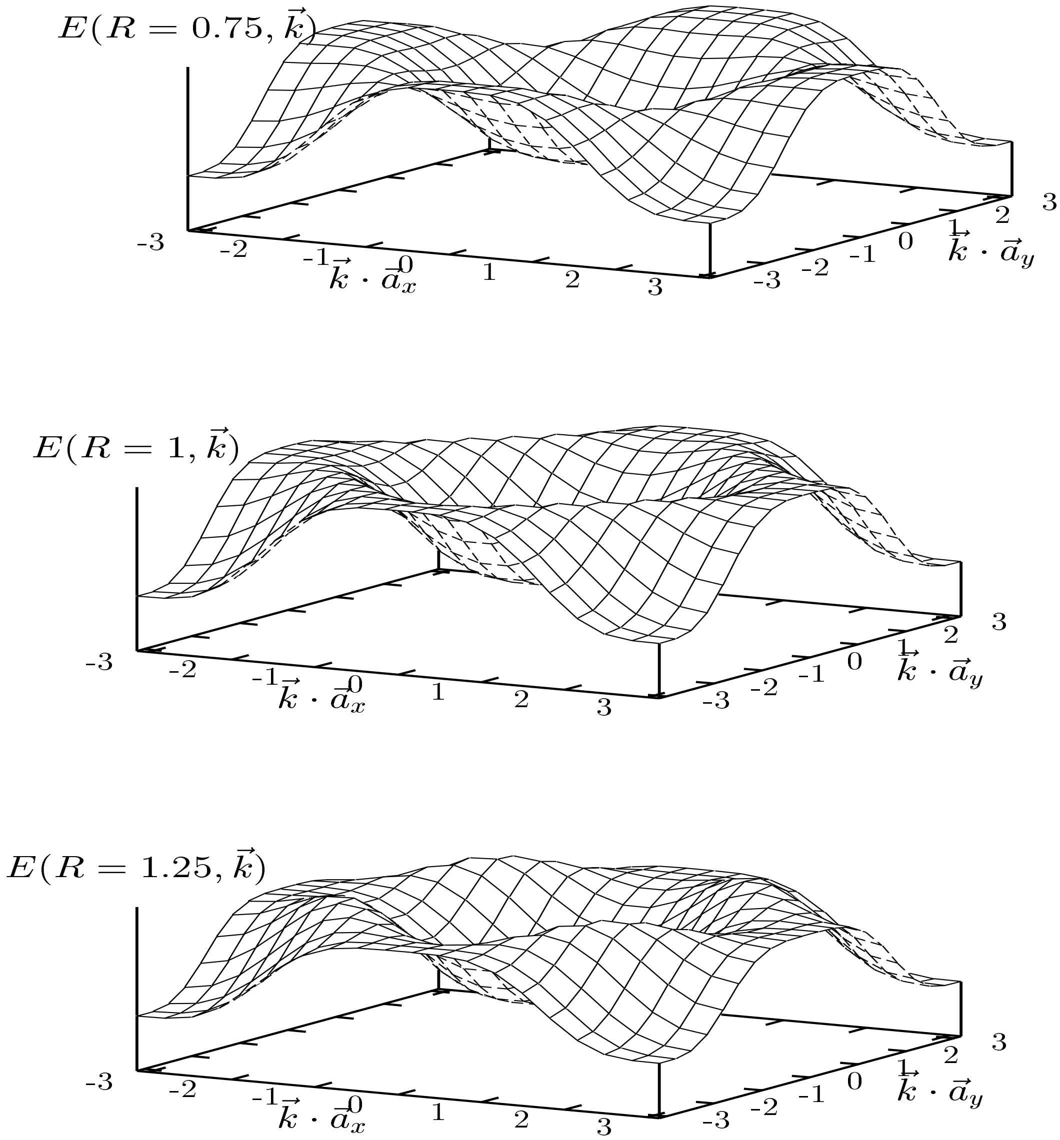

Figure 2.7: The dispersion relation $E(R, \vec{k})$ for the toy model of Eq. 2.21. At $R < 1$ the flat bands at $\vec{k} = (0, \pm\pi)$, $\vec{k} = (\pm\pi, 0)$ dominate the low energy physics. At $R > 1$ the hole pockets at at $\vec{k} = (\pm\pi/2, \pm\pi/2)$ dominate. At $R = 1$ both structures are degenerate.

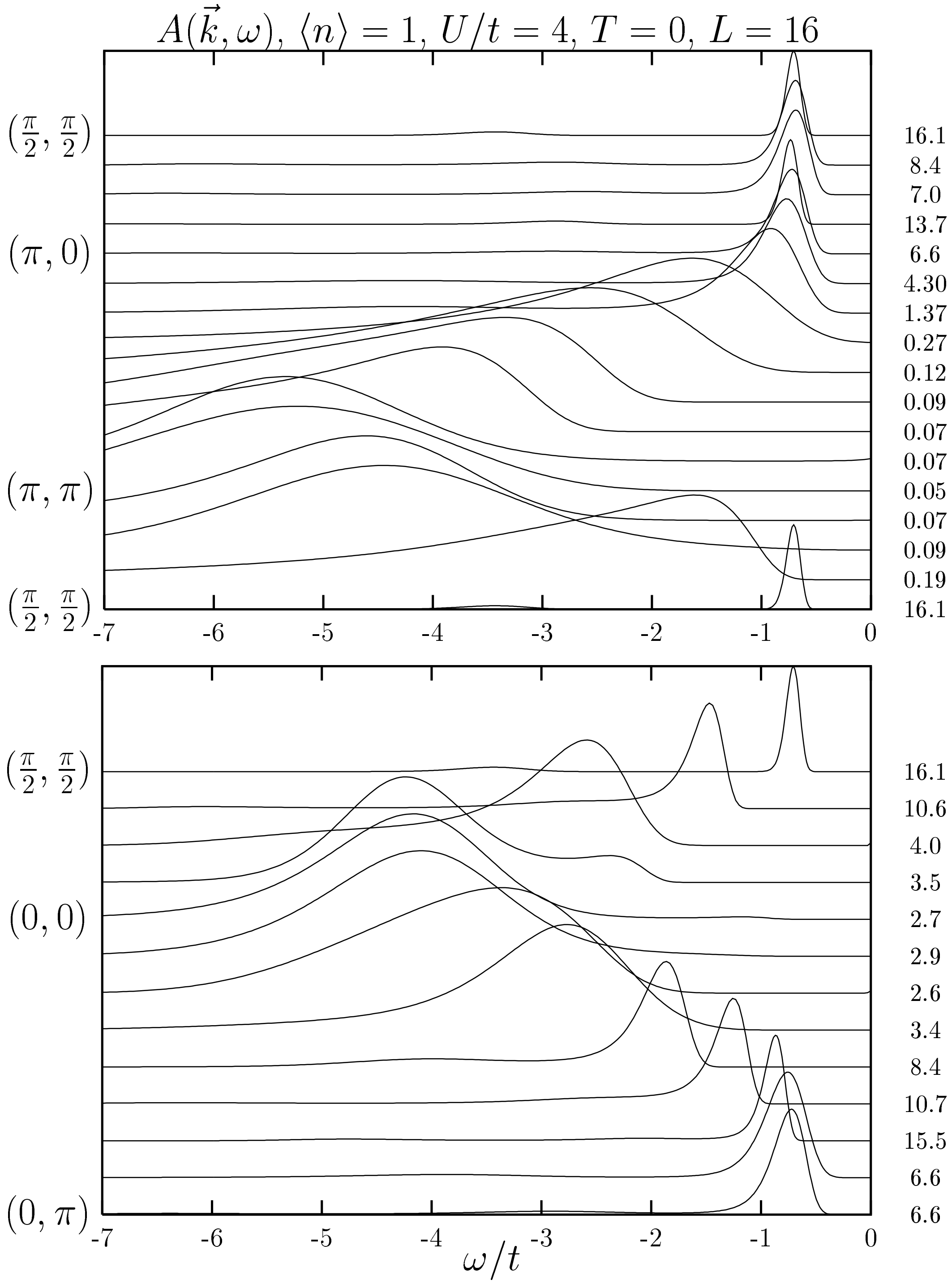

Figure 2.8: $A(\vec{k},\omega)$ at $T = 0$ for the half-filled Hubbard model at $U/t = 4$ on a 16×16 lattice. The considered $\vec{k}$ points in the Brillouin zone are listed on the left hand side of the figure. We have normalized the raw data by the factor listed on the right hand side of the figure. This normalization sets the peak value of $A(\vec{k},\omega)$ to unity for all considered $\vec{k}$ vectors.

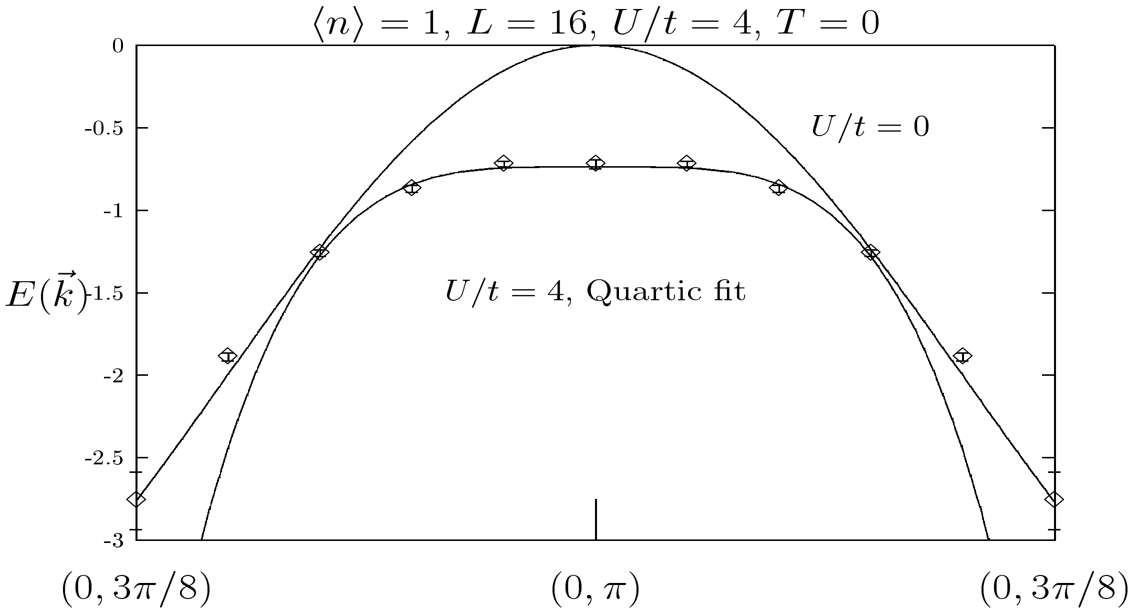

Figure 2.9: Symbols denote the dispersion relation $E(\vec{k})$ as obtained from the the peak position of the $A(\vec{k}, \omega)$ data presented in Fig. 2.8. The data is compatible with a quartic fit over an acceptable range. For comparison, we have plotted the dispersion relation at $U/t = 0$. For this dispersion relation, the vanishing of the Fermi velocity at $\vec{k} = (0, \pi)$ generates a logarithmic (Van-Hove) singularity in the single particle density of states. The quartic dispersion relation yields a square-root divergence in the single particle density of states.

Chapter 3

Quantum Transition Between a Mott Insulator and $d_{x^2-y^2}$ Superconductor in Two-Dimensions

In this Chapter, we consider the two-dimensional repulsive Hubbard model with an additional term which essentially contains pair hopping processes. The motivations for adding this term are two-fold:
i) The occurrence of superconductivity in the doped two-dimensional Hubbard model is an open issue. It is fair to say that at energy scales accessible to numerical simulations, no convincing sign of superconductivity has been found in the Hubbard, t-J, or 3-bands Hubbard models [30, 34, 63, 85–88]. The model introduced in this section shows large (in comparison to the Hubbard model) d-wave paring fluctuations at finite doping. It thus provides us with a model to study the interplay between magnetism and d-wave superconductivity at energy scales accessible to numerical simulations.
ii) In the previous chapters we have studied numerically the nature of the doping induced metal-insulator transition in the two-dimensional Hubbard model. An interpretation of the Monte-Carlo data as well as exact diagonalization results [39] leads to the concept of an incoherent metallic state in the vicinity of the Mott insulator. Within a scaling assumption this is described by an anomalously large dynamical exponent, $z = 4$ [22, 40]. Such a metallic state should be unstable to a perturbation capable of restoring coherence. Adding single particle terms is not sufficient. This statement is based on numerical data which show that adding a next-nearest neighbor hopping matrix element does not alter the critical behavior of the compressibility [6]. However, pair hopping is a relevant perturbation, since, as we will see, it changes the very nature of the metal-insulator transition.

Both motivations are clearly linked and one may view motivation i) as a consequence of motivation ii). More generally the metallic state in the vicinity of the Mott insulator is close to a host of potential instabilities. In this context, we note the occurrence of stripe ordering in the t-J [89] when open boundary conditions are imposed along one lattice direction. By adding a pair-hopping term we generate an instability towards a d-wave superconductor.

The chapter is organized as follows. In the next section, we describe the model. In Sec. 3.1 we will study the doping induced metal-insulator transition at finite W. Here W denotes the magnitude of the added term. We will give numerical evidence that doping the model at finite values of W leads to a $d_{x^2-y^2}$ superconductor. In Sec. 3.3 we will consider the model at half-filling, and show that at fixed values of the Hubbard repulsion U, W drives the antiferromagnetic Mott insulator to a $d_{x^2-y^2}$ superconductor.

3.1 The t-U-W model

Our starting point is the Hubbard model on a square lattice which we write in the form:

$$H_{tU} = -\frac{t}{2}\sum_{\vec{i}} K_{\vec{i}} + U\sum_{\vec{i}}(n_{\vec{i},\uparrow} - \frac{1}{2})(n_{\vec{i},\downarrow} - \frac{1}{2}) \tag{3.1}$$

where

$$K_{\vec{i}} = \sum_{\sigma,\vec{\delta}} \left(c^{\dagger}_{\vec{i},\sigma} c_{\vec{i}+\vec{\delta},\sigma} + c^{\dagger}_{\vec{i}+\vec{\delta},\sigma} c_{\vec{i},\sigma} \right). \tag{3.2}$$

Here $\vec{\delta} = \pm\vec{a}_x, \pm\vec{a}_y$. The term we add is given by the square of the local kinetic energy:

$$H_W = -W\sum_{\vec{i}} K^2_{\vec{i}}. \tag{3.3}$$

That this term contains pair hopping processes will be explicitly shown below. The precise choice of this form finds its origin in technical considerations. At half-band filling ($\mu = 0$) the Hamiltonian:

$$H_{tUW} = H_{tU} + H_W \tag{3.4}$$

is particle-hole invariant. Furthermore, the W term has a simple Hubbard Stratonovitch transformation. This has for important consequence that the sign problem may be avoided in QMC approaches at half-filling. This statement is valid for the twisted boundary conditions:

$$c_{\vec{i}+L\vec{a}_x,\sigma} = \exp\left(2\pi i\Phi/\Phi_0\right) c_{\vec{i},\sigma} \quad \text{and} \quad c_{\vec{i}+L\vec{a}_y,\sigma} = c_{\vec{i},\sigma}, \tag{3.5}$$

where L denotes the linear length of the square lattice and $\Phi_0 = hc/e$ the flux quanta. Those boundary conditions account for a magnetic flux threading a torus on which lies the electronic system. The details of the algorithm will be reviewed in Chap. 4.

The W term may be written as

$$H_W = H_W^{(1)} + H_W^{(2)} + H_W^{(3)} + H_W^{(4)} \tag{3.6}$$

with

$$H_W^{(1)} = -8WN \tag{3.7}$$

where N denotes the number of sites.

$$H_W^{(2)} = -W \sum_{\vec{i},\sigma,\vec{\delta},\vec{\delta}'} \left(c^\dagger_{\vec{i},\sigma} c^\dagger_{\vec{i},-\sigma} c_{\vec{i}+\vec{\delta}',-\sigma} c_{\vec{i}+\vec{\delta},\sigma} + \text{H.c.} \right) \tag{3.8}$$

$$H_W^{(3)} = +W \sum_{\vec{i},\vec{\delta},\vec{\delta}',m=-1,0,1} \left(T^\dagger_{\vec{i},\delta',m} T_{\vec{i},\delta,m} + T_{\vec{i},\delta',m} T^\dagger_{\vec{i},\delta,m} \right) \tag{3.9}$$

and

$$H_W^{(4)} = -W \sum_{\vec{i},\vec{\delta},\vec{\delta}'} \left(\Delta^\dagger_{\vec{i},\delta'} \Delta_{\vec{i},\delta} + \Delta_{\vec{i},\delta'} \Delta^\dagger_{\vec{i},\delta} \right). \tag{3.10}$$

Here, $T^\dagger_{\vec{i},\delta,1} = c^\dagger_{\vec{i},\uparrow} c^\dagger_{\vec{i}+\vec{\delta},\uparrow}$, $T^\dagger_{\vec{i},\delta,-1} = c^\dagger_{\vec{i},\downarrow} c^\dagger_{\vec{i}+\vec{\delta},\downarrow}$, $T^\dagger_{\vec{i},\delta,0} = \left(c^\dagger_{\vec{i},\uparrow} c^\dagger_{\vec{i}+\vec{\delta},\downarrow} + c^\dagger_{\vec{i},\downarrow} c^\dagger_{\vec{i}+\vec{\delta},\uparrow} \right)/\sqrt{2}$, and $\Delta^\dagger_{\vec{i},\delta} = \left(c^\dagger_{\vec{i},\uparrow} c^\dagger_{\vec{i}+\vec{\delta},\downarrow} - c^\dagger_{\vec{i},\downarrow} c^\dagger_{\vec{i}+\vec{\delta},\uparrow} \right)/\sqrt{2}$. In the presence of the Hubbard U with $U > W$, $H_W^{(2)}$ may be neglected since it involves processes containing double occupied sites costing an energy U. $H_W^{(3)}$ describes triplet pair-hopping. The fact that this term comes with a positive sign, and that local triplet configurations are not favored by the superexchange generated by the Hubbard U, gives us arguments to conclude that it will not affect the low energy physics. $H_W^{(4)}$ is clearly a relevant term. It may be rewritten as:

$$\begin{aligned}
H_W^{(4)} &= 2W \sum_{\vec{i},\vec{\delta}} \left(\vec{S}_{\vec{i}} \cdot \vec{S}_{\vec{i}+\vec{\delta}} - \frac{1}{4} \left(n_{\vec{i}} - 1\right) \left(n_{\vec{i}+\vec{\delta}} - 1\right) \right) \\
&- \frac{W}{2} \sum_{\vec{i},\vec{\delta}\neq\vec{\delta}',\sigma} \left(c^\dagger_{\vec{i}+\vec{\delta},\sigma} n_{\vec{i},-\sigma} c_{\vec{i}+\vec{\delta}',\sigma} - c^\dagger_{\vec{i}+\vec{\delta},\sigma} c^\dagger_{\vec{i},-\sigma} c_{\vec{i},\sigma} c_{\vec{i}+\vec{\delta}',-\sigma} \right) \\
&- \frac{W}{2} \sum_{\vec{i},\vec{\delta}\neq\vec{\delta}',\sigma} \left(c_{\vec{i}+\vec{\delta},\sigma} \left(1 - n_{\vec{i},-\sigma}\right) c^\dagger_{\vec{i}+\vec{\delta}',\sigma} - c_{\vec{i}+\vec{\delta},\sigma} c_{\vec{i},-\sigma} c^\dagger_{\vec{i},\sigma} c^\dagger_{\vec{i}+\vec{\delta}',-\sigma} \right)
\end{aligned}$$

The first term in the above equation is obtained by setting $\delta = \delta'$ in $H_W^{(4)}$ and corresponds to a superexchange. Here $\vec{S}_{\vec{i}}$ denotes the spin operator on site $\vec{i}$. The second term of the above equation corresponds precisely to the three site term obtained in a strong coupling expansion of the Hubbard model [41]. The third term is just the particle hole transform of the three site term.

The precise physical origin of the W term is unclear. We note however, that starting from a Su-Schrieffer-Heeger [90] type term with Einstein oscillators:

$$\sum_{\vec{i},\sigma} \vec{\lambda} \cdot \vec{Q}_{\vec{i}} K_{\vec{i}} + \sum_{\vec{i}} \left(\frac{\vec{P}_{\vec{i}}^{2}}{2M} + \vec{Q}_i^{\dagger} \frac{D}{2} \vec{Q}_i \right), \tag{3.11}$$

and taking the antiadiabatic limit ($M \to 0$), generates H_W with $W = \vec{\lambda}^{\dagger} D^{-1} \vec{\lambda}/2$. Pairing mechanism along those lines were considered in [91]. Here, however, we view this simply as a Hubbard Stratonovitch transformation which is useful in constructing the Monte-Carlo simulation. As mentioned at the beginning of this chapter, our aim is to add pair-hopping processes. The W term does this in a way which avoids the minus sign problem inherent to QMC methods at half-band filling.

3.2 Doping induced metal-insulator transition in the t-U-W model

At half-band filling, $U/t = 4$ and $W < W_c \sim 0.3t$ the t-U-W model remains a Mott insulator with long range antiferromagnetic order. This statement will be show in the next section. Here we study the metal-insulator transition obtained by doping the t-U-W model for $W < W_c$. The calculations presented in this section were carried out at with periodic boundary conditions (i.e. $\Phi = 0$ in Eq. 3.5).

3.2.1 The localization length and single particle excitations at half-band filling

The calculation of the localization length for the t-U-W model, is very similar to that of the Hubbard model (see Chap. 2). The details of the calculations may be found in [58]. We consider the parameter set: $U/t = 4$ and $W/t = 0.05$. For this parameter set, the quasiparticle gap is plotted as a function of system size in Fig. 3.1. Extrapolation to the thermodynamic limit yields: $\Delta_{qp}/t \equiv \mu_c = 0.62 \pm 0.02$. The localization length obtained from simulations on cluster sizes up to 12×12 is plotted in Fig. 3.2. For comparison, we have included the data for the Hubbard model at $U/t = 4$. The numerical data are consistent with

$$\begin{aligned} \xi_l \sim |\omega - \mu_c|^{-1/4} \ \text{at} \ U/t = 4, W/t &= 0 \\ \xi_l \sim |\omega - \mu_c|^{-1/2} \ \text{at} \ U/t = 4, W/t &= 0.05 \end{aligned} \tag{3.12}$$

Thus, we are lead to the important conclusion that switching on W alters the nature of the metal-insulator transition.

In the previous chapter, we had argued that the origin of the exponent $\nu = 1/4$ for the two dimensional Hubbard model could be traced back to the existence of flat *bands* around the $(\pm\pi, 0)$, $(0, \pm\pi)$ points in the Brillouin zone. If this is the case, the transition from $\nu = 1/4$ to $\nu = 1/2$ observed upon switching on W should be reflected in the dispersion relation. With the use of the Maximum Entropy method, we compute $A(\vec{k}, \omega)$ at $W/t = 0.15$, $U/t = 4$, half-band filling, zero temperature and on a 16×16 lattice. The results are plotted in Fig. 3.3. The following points are of importance.
i) The band width. Upon inspection of Fig. 3.3 one notices that the band width is substantially enhanced by the inclusion of the W term. This high energy phenomena may be captured at a mean-field level. We follow the case of the half-filled Hubbard model and carry out the spin-density wave Ansatz:

$$\langle n_{\vec{i},\uparrow} \rangle + \langle n_{\vec{i},\downarrow} \rangle = 1, \ \langle n_{\vec{i},\uparrow} \rangle - \langle n_{\vec{i},\downarrow} \rangle = (-m)^{i_x + i_y} \ \text{ and } \ \langle K_{\vec{i}} \rangle = K. \tag{3.13}$$

Writing $n_{\vec{i},\sigma} = \langle n_{\vec{i},\sigma} \rangle + \left(n_{\vec{i},\sigma} - \langle n_{\vec{i},\sigma} \rangle \right)$, $K_{\vec{i}} = K + (K_{\vec{i}} - K)$ and neglecting fluctuations yields the mean-field Hamiltonian:

$$\begin{aligned} H_{HF} &= \sum_{\vec{k} \epsilon MBZ, \sigma} E_+(\vec{k}) \gamma^\dagger_{\vec{k},\sigma} \gamma_{\vec{k},\sigma} + E_-(\vec{k}) \eta^\dagger_{\vec{k},\sigma} \eta_{\vec{k},\sigma} \qquad (3.14) \\ E_\pm &= \pm \sqrt{\Delta^2 + \epsilon^2_{\vec{k}}}, \ \ \Delta = \frac{Um}{2}, \ \text{ and } \ \epsilon(\vec{k}) = -2\left[t + 4WK\right](\cos k_x + \cos k_y) \end{aligned}$$

The $\vec{k}$ summation runs over the magnetic Brillouin zone (MBZ) and the γ and η operators are given by Eq. 2.14. At $T = 0$, self-consistency requires:

$$1 = \frac{U}{2N} \sum_{\vec{k} \epsilon MBZ, \sigma} \frac{1}{\sqrt{\Delta^2 + \epsilon^2_{\vec{k}}}} \ \text{ and } \ K = \frac{8}{N} \sum_{\vec{k} \epsilon MBZ} \left(\cos(k_x) + \cos(k_y) \right). \tag{3.15}$$

Setting $W/t = 0.15$, $U/t = 4$ one obtains, $t + 4WK = 2.9t$ and $\Delta = 0.43t$ thus leading to a band-with of $11.9t$ which is compatible with the Monte-Carlo data. That this approximation does not capture the low energy physics may be seen by considering the quotient $\Delta(U/t = 4, W/t = 0)/\Delta(U/t = 4, W/t = 0.15)$. The mean field approximation yields the value 3.2 whereas the QMC the value 1.2 (Fig. 3.1).
ii) The dispersion relation. Around the $(\pi, 0)$ point, the dispersion relation as defined by the peak position in $A(\vec{k}, \omega)$ is not as flat as in the case of the Hubbard model. This is shown explicitly in Fig. 3.4 where we consider the direction $(0, 0)$ to $(0, \pi)$. The data is compatible with a quadratic fit. For comparison, we have plotted the dispersion relation obtained within the paramagnetic phase (i.e. $m = 0$) of the above mean-field equations. To fit better the data, we have used an effective hopping parameter set by $2.4t$ rather the value $2.9t$ predicted by the above mean-field equations. Thus, the flat *band* observed in the Hubbard model disappears upon

switching on W/t. To be more precise, domain in $\vec{k}$-space around the $(0, \pm\pi)$ $(\pm\pi, 0)$ points which is compatible with a $|\vec{k}|^4$ fit is quickly suppressed when W is switched on.

To further check the above statements, we have computed the single particle density of states:

$$N(\omega) \equiv \frac{1}{N} \sum_{\vec{k}} \mathrm{Im} G(\vec{k}, \omega) \tag{3.16}$$

At zero-temperature and $\tau t > 0$, this quantity is related to the imaginary time QMC data via

$$G(\vec{r} = \vec{0}, \tau) = \frac{1}{\pi} \int_0^\infty \mathrm{d}\omega e^{-\tau\omega} N(\omega). \tag{3.17}$$

$N(\omega)$ is extracted from the above equation with the use of the Maximum-Entropy method. A flat band picture results in a large value of $N(\omega)$ for frequencies close to the quasiparticle gap. In comparison, at finite values of W/t where we obtain the correlation length exponent $\nu = 1/2$, we expect no anomalous enhancement of $N(\omega)$ at frequencies equal to the quasiparticle gap. In fact, for the generic metal-insulator transition in two-dimensional systems for which one obtains the exponent $\nu = 1/2$, $N(\omega)$ remains a finite constant until it jumps to zero at the band-edge. Fig. 3.5 plots $N(\omega)$ for lattice sizes ranging from $L = 6$ to $L = 16$ at $U/t = 4$, $T = 0$ and for both $W/t = 0$ and $W/t = 0.15$. Due to particle-hole symmetry, $N(\omega) = N(-\omega)$. It is clear that as W/t is enhanced, the large density of states present at $\omega \sim \Delta_{qp}$ vanishes.

3.2.2 Spin-susceptibility and pairing correlations at finite doping

We now consider finite doping. Here we are confronted with a sign problem which leads for a given accuracy to an exponential increase of CPU time as the lattice size and inverse temperature grows (see Sec. 1.3). We will show that both the spin susceptibility and pairing correlations are consistent with the interpretation that doping the Mott insulator at finite values of W/t leads to a $d_{x^2-y^2}$ superconductor.

We start by considering pairing correlations. The vertex contribution to the equal time pair-field correlations is given by:

$$P^v_{d,s}(\vec{r}) = P_{d,s}(\vec{r}) - \sum_{\sigma,\vec{\delta},\vec{\delta}'} f_{d,s}(\vec{\delta}) f_{d,s}(\vec{\delta}') \left(\langle c^\dagger_{\vec{r},\sigma} c_{\vec{\delta}',\sigma} \rangle \langle c^\dagger_{\vec{r}+\vec{\delta},-\sigma} c_{\vec{0},-\sigma} \rangle + \langle c^\dagger_{\vec{r},\sigma} c_{\vec{0},\sigma} \rangle \langle c^\dagger_{\vec{r}+\vec{\delta},-\sigma} c_{\vec{\delta}',-\sigma} \rangle \right) \tag{3.18}$$

where

$$P_{d,s}(\vec{r}) = \langle \Delta^\dagger_{d,s}(\vec{r}) \Delta_{d,s}(\vec{0}) \rangle \tag{3.19}$$

with

$$\Delta^\dagger_{d,s}(\vec{r}) = \sum_{\sigma,\vec{\delta}} f_{d,s}(\vec{\delta}) \sigma c^\dagger_{\vec{r},\sigma} c^\dagger_{\vec{r}+\vec{\delta},-\sigma}. \tag{3.20}$$

Here, $f_s(\vec{\delta}) = 1$ and $f_d(\vec{\delta}) = 1(-1)$ for $\vec{\delta} = \pm\vec{a_x}$ $(\pm\vec{a_y})$. Per definition, $P^v_{d,s}(\vec{r}) \equiv 0$ in the absence of interactions. Fig. 3.6 plots $P^v_{d,s}(L/2, L/2)$ at $\langle n \rangle = 0.78$, and $U/t = 4$ as a function of temperature. We consider an 8×8 lattice with $W/t = 0$, $W/t = 0.05$ and $W/t = 0.15$. As W/t grows, there is a substantial increase in $P^v_d(L/2, L/2)$. This stands in contrast to the signal obtained in the extended s-wave channel where virtually no enhancement as a function of W/t is seen. It is important to note that the W term does not explicitly favor d-wave symmetry. We will argue below that this symmetry is stabilize due to the magnetic degrees of freedom.

We now consider the spin susceptibility. It is defined by

$$\begin{aligned} \mathrm{Re}\chi\left(\vec{q}, \omega = 0\right) &\equiv \int_0^\beta \mathrm{d}\tau \langle m_z\left(\vec{q}, \tau\right) m_z\left(-\vec{q}, 0\right)\rangle \\ m_z\left(\vec{q}, \tau\right) = e^{\tau H} m_z\left(\vec{q}\right) e^{-\tau H} \quad &\text{and} \quad m_z\left(\vec{q}\right) = \frac{1}{\sqrt{N}} \sum_{\vec{r}} e^{i\vec{q}\vec{r}} \left(n_{\vec{r},\uparrow} - n_{\vec{r},\downarrow}\right). \end{aligned} \tag{3.21}$$

We again consider the band-filling $\langle n \rangle = 0.78$, and scan as a function of temperature. In the absence of interactions, (U = W = 0) the uniform $(\vec{q} = 0)$ spin susceptibility is plotted in Fig. 3.7 (solid line). At $U/t = 4$ we observe an enhancement of the spin susceptibility over its non-interacting value. This may be understood through the Stoner enhancement in a random phase approximation (RPA). As W/t increases at constant $U/t = 4$ one sees a strong suppression the uniform spin susceptibility. There is a temperature window where it is reduced over the non-interacting value. At $W/t = 0.05$, the temperature value at which the susceptibility is reduced in comparison to the non-interacting value corresponds to the temperature scale at which d-wave paring is enhanced over s-wave paring (see Fig. 3.6). This energy scale grows rapidly with W/t.

The spin structure factor,

$$S(\vec{q}) \equiv \langle m_z(\vec{q}) m_z(-\vec{q})\rangle \tag{3.22}$$

is plotted in Fig. 3.8 at $\langle n \rangle = 0.78$, $U/t = 4$ as a function of temperature. We consider $W/t = 0$ and $W/t = 0.15$ on an 8×8 lattice. The different temperature behaviors of $S(\vec{q})$ at $\vec{q} = 0$ may be traced back to our discussion of the spin susceptibility since $\beta S(\vec{q} = 0)$ is nothing but the uniform spin susceptibility. In the case of an s-wave superconductor, one would expect the spin-spin correlations to be suppressed at all wave vectors when the pairing occurs. Precisely the contrary is seen in Fig. 3.8. The overall structure around $\vec{q} = (\pi, \pi)$ is sharper at $W/t = 0.15$ than at $W/t = 0$. We note that we are considering the same energy scale as in Fig. 3.6 where a strong enhancement pair field correlations was observed with growing values of W/t. The W term does contain an exchange interaction so that we do expect the magnetic length scale associated with antiferromagnetic fluctuations to grow as a function of W. The fact that $P^v(L/2, L/2)$ grows at same energy scale shows the compatibility between antiferromagnetic fluctuations and d-wave superconductivity. We will return to this point in the next section.

3.3 The t-U-W model at half-band filling

In this section, we show that at half-band filling fixed values of U the W term drives the ground state from Mott insulator with long-range antiferromagnetic order to a $d_{x^2-y^2}$ superconductor.

3.3.1 Charge degrees of freedom at $T = 0$

An efficient and general method to distinguish between an insulator and superconductor is to compute the ground state energy as a function of a twist Φ in the boundary condition along one lattice direction: $E_0(\Phi)$. In the case of an insulator the wave function is localized and hence, an exponential decay of $\Delta E_0(\Phi) \equiv E_0(\Phi) - E_0(\Phi_0/2)$ as a function of lattice size is expected [2]. In the spin density wave (SDW) approximation for the half-filled Hubbard model, one obtains $\Delta E_0(\Phi) = \alpha(\Phi) L \exp(-L/\xi)$ where ξ is the localization length of the wavefunction. On the other hand, for a superconductor (i.e off-diagonal long-range order (ODLRO)), $\Delta E_0(\Phi)$ shows anomalous flux quantization: $\Delta E_0(\Phi)$ is a periodic function of Φ with period $\Phi_0/2$ and a non vanishing energy barrier is to be found between the flux minima [5, 63, 92, 93] so that $\Delta E_0(\Phi_0/4)$ remains finite as $L \to \infty$. In general, this functional form of $\Delta E_0(\Phi)$ should occur only in the thermodynamic limit.

Fig. 3.9 shows $\Delta E_0(\Phi)$ at $W/t = 0.1$ and $W/t = 0.5$. At $W/t = 0.1$, and as expected for an insulator $\Delta E_0(\Phi)$ is suppressed with growing lattice sizes for all values of Φ. In contrast, at $W/t = 0.5$ one notes that for values of $1/4 < \frac{\Phi}{\Phi_0} < 1/2$, $\Delta E_0(\Phi_0)$ is very stable against growing lattice sizes. On the other hand, at $\Phi = 0$, $\Delta E_0(\Phi)$ decreases with growing lattice sizes. We interpret the data as a finite size indication of anomalous flux quantization. However, we have not firmly established the existence of a flux minima at $\Phi = 0$. Very similar results were obtained in the case of the repulsive and attractive Hubbard models at half-filling [5, 63]. In the case of the half-filled attractive Hubbard model no clear sign of a local flux minima at $\Phi = 0$ was observed up to lattice size $L = 10$ [5].

With the above in mind, we consider the size scaling of the quantity $\Delta E_0(\Phi_0/4)$ for various values of W/t (Fig. 3.10a). One observes a change in the size-scaling of $\Delta E_0(\Phi_0/4)$ as W/t decreases from $W/t = 0.5$ to $W/t = 0.22$. From these measurements, we estimate that the change occurs in the vicinity of $W/t = 0.3$. For values of $W/t < 0.3$, $\Delta E_0(\Phi_0/4)$ is consistent with the SDW form whereas for $W/t \geq 0.33$ $\Delta E_0(\Phi_0/4)$ may be extrapolated to a finite value with finite size corrections proportional to $1/L$. The extrapolated value of $\Delta E_0(\Phi_0/4)$ versus W/t is plotted in Fig. 3.10b. The quantum transition between the Mott insulator and superconductor occurs at $W/t \sim 0.3$.

In order to determine the symmetry of the superconducting order parameter we have computed the vertex contribution to equal time pair-field correlations in the extended s-wave and $d_{x^2-y^2}$ channels. Those quantities are defined in Eq. (3.18). In order to be able to reach large lattices, we have have set $W/t = 0.35$, $\Phi/\Phi_0 = 0.5$ and reduced the Hubbard repulsion to $U/t = 2$. For this choice of parameters the $\Delta E_0(\Phi_0/4)$ criterion (data not shown) shows that we are well within the superconducting state. Fig. 3.11 plots $P_d^v(\vec{r})$ along the diagonal of the lattice. We consider lattices ranging up to $L = 24$. For a fixed lattice size, one notices a plateau structure as a function of distance. The extrapolation of this plateau value to the thermodynamic limit is hard. We note however that it decays slower than $1/L$. In comparison to the d-wave signal, the extended-s wave signal at *large* distances, P_s^v (data not shown) may not be distinguished from zero within our accuracy. At short distances extended s-wave pair-field correlation dominate. The data confirming this statement may be found in the table. The W term, contains no processes which explicitly favor d-wave superconductivity. On the contrary, one would expect the W term to favor extended s-wave symmetry, and this shows up at high energies or equivalently short length scales. The fact that d-wave symmetry dominates the long-range can be traced back to the spin degrees of freedom.

To summarize, at $U/t = 4$, W triggers a zero temperature transition between a Mott insulating state and $d_{x^2-y^2}$ superconducting state. This transition occurs at $W_c/t \sim 0.3$.

3.3.2 Spin degrees of freedom at $T = 0$

To detect the existence of long-range magnetic order, we compute the real space spin-spin correlations,

$$S(\vec{r}) = \frac{4}{3}\langle \vec{S}(\vec{r})\vec{S}(\vec{0})\rangle \tag{3.23}$$

where $\vec{S}(\vec{r})$ denotes the spin operator on site $\vec{r}$. For values of $W/t < 0.3$ and lattice sizes ranging from $L = 4$ to $L = 12$, $S(L/2, L/2)$, may be fitted to a $1/L$ form and scales to a finite value as shown in Fig. 3.12a. We therefore conclude that long-range antiferromagnetic order is present for $W/t < 0.3$. The associated staggered moment, $m = \lim_{L\rightarrow\infty}\sqrt{3S(L/2, L/2)}$, is plotted in Fig. 3.12b. The data is consistent with a continuous decay of m as W/t increases towards 0.3. At $W/t = 0.3$, we were unable to distinguish m from zero within our statistical uncertainty. Hence, we conclude that long-range antiferromagnetic order vanishes at $W/t \sim 0.3$ for $U/t = 4$. Within our numerical resolution, the magnetic and superconductor-insulator transitions occur simultaneously.

Well within the $d_{x^2-y^2}$ superconducting phase the spin-spin correlations remain sizable. In fact, at $W/t = 0.6$, lattice sizes ranging from $L = 4$ to $L = 16$, $S(L/2, L/2)$ scales as $L^{-\alpha}$ with $\alpha = 1.16 \pm 0.01$ as shown in the inset of Fig. 3.12a. To further study the spin-spin correlations in the superconducting phase, we fix $W/t = 0.35$ and vary the value of U from $U/t = 1$ to $U/t = 4$. For all those parameter values, we are in the superconducting phase. In Fig. 3.13 $S(L/2, L/2)$ is plotted versus $1/L$. The data are consistent with,

$$\begin{aligned} S(L/2, L/2) &\sim L^{-1.49} \text{ for } U/t = 1 \\ S(L/2, L/2) &\sim L^{-1.32} \text{ for } U/t = 2 \\ S(L/2, L/2) &\sim L^{-1.17} \text{ for } U/t = 3 \\ S(L/2, L/2) &\sim L^{-1.01} \text{ for } U/t = 4. \end{aligned} \tag{3.24}$$

The statement in Eq. (3.24) deserves confirmation. If the exponent α reflects bulk properties, it should be independent on the choice of the boundary. Fig. 3.14 plots $S(L/2, L/2)$ at $U/t = 1$ and $U/t = 2$ for $W/t = 0.35$. At $\Phi = 0$, the solid lines corresponds to least square fits to the form $c(\Phi = 0)L^{-\alpha}$. This fit determines the exponent α. Since the data at $\Phi = \Phi_0/2$ is consistent at large distances with the form $c(\Phi = \Phi_0/2)L^{-\alpha}$ we conclude that the exponent α is independent on the choice of the boundary. For the $\Phi = \Phi_0/2$ simulations we were able to reach lattices up to 24×24. The spin structure factor, $S(\vec{q})$ is plotted in Fig. 3.15. Although there is a steady growth of $S(\vec{Q} = (\pi, \pi))$ as a function of lattice size, we were not able to reproduce the value of the above mentioned exponent through a finite size scaling of this quantity.

The fact that spin-spin correlations decay as a powerlaw is not surprising, in the case of a $d_{x^2-y^2}$ superconductor. Following Ref. [94], one can approximate the spin susceptibility, $\chi(\vec{q}, i\omega_m)$, in the superconducting state by inserting the irreducible BCS spin susceptibility, $\chi_0^{BCS}(\vec{q}, i\omega_m)$, in the random phase approximation (RPA) form of $\chi(\vec{q}, i\omega_m)$: $\chi_{RPA}(\vec{q}, i\omega_m) = \chi_0^{BCS}(\vec{q}, i\omega_m)/(1 - U\chi_0^{BCS}(\vec{q}, i\omega_m))$. Here, ω_m corresponds to Matsubara frequencies. Within this approximation and at half-band filling, the spin-spin correlations for a $d_{x^2-y^2}$ superconducting order parameter show a power-law decay: $S^{RPA}(L/2, L/2) \sim L^{-3.5}$. The value of the exponent is independent of U. In contrast, the spin-spin correlations in an s-wave superconductor decay exponentially. Thus, the fact that the spin-spin correlations decay as a power-law in the superconducting state, may be attributed to the node and phase factors of the $d_{x^2-y^2}$ superconducting gap.

The very slow decay of the spin-spin correlations in the superconducting state revealed by the QMC data shows the extreme compatibility between a $d_{x^2-y^2}$ superconductor and substantial short-range antiferromagnetic spin-spin correlations. We summarize with the following points.

i) Long range spin-spin correlations are not present in the superconducting phase. However, since $S(\vec{r})$ decays slower than $\cos(\vec{Q}\vec{r})/|\vec{r}|^2$ and the dimension is equal to two, $S(\vec{Q}) \sim \sum_{\vec{r}} e^{i\vec{Q}\vec{r}} S(\vec{r})$ diverges.

ii) The exponent α depends on the coupling constants U and W. This is a common feature in one-dimensional quantum systems such as the t-J or Hubbard models at $T = 0$. In two dimensions, and to the author's knowledge, this is novel.

3.3.3 Finite temperature spin dynamics in the superconducting phase

Here, we consider the parameter set $U/t = 4$ and $W/t = 0.35$. This puts us in superconducting state close to the quantum transition. We will compare our results to the case of the Mott insulator obtained at $U/t = 4$, $W/t = 0$.

We first consider the static spin susceptibility defined in Eq. (3.21). Let us start by briefly summarizing the temperature dependence of $\mathrm{Re}\chi(\vec{q}, \omega = 0)$ at wave vectors $\vec{q} = 0$ and $\vec{q} = \vec{Q} \equiv (\pi, \pi)$ for the Hubbard model at $U/t = 4$. The results are plotted in Fig. 3.16. One expects the physics of the half-filled Hubbard model to be well described by a Heisenberg model in the renormalized classical regime [18, 19]. Hence, an exponential divergence of $\mathrm{Re}\chi(\vec{Q}, \omega = 0)$ as a function of temperature is expected. The data (see Fig. 3.16b) shows a sharp increase at a temperature scale $T \sim 0.25t$. We use this criterion to define the magnetic energy scale $J \sim 0.25t$ at $W/t = 0$. At temperatures $T > J$ the uniform static susceptibility $\mathrm{Re}\chi(\vec{q} = 0, \omega = 0)$ increases monotonically with decreasing temperature. In this temperature regime, the overall scale of $\mathrm{Re}\chi(\vec{q} = 0, \omega = 0)$, is greater than its non-interacting value. This enhancement can be understood by the Stoner enhancement in the RPA. In the low temperature limit $\mathrm{Re}\chi(\vec{q} = 0, \omega = 0)$ scales to a finite value due to the existence of gapless spin-wave excitations. One notices that $\mathrm{Re}\chi(\vec{q} = 0, \omega = 0)$ shows a maximum at approximately $T \sim J$.

At $W/t = 0.35$ $\mathrm{Re}\chi(\vec{Q}, \omega = 0)$ diverges in the low temperature limit (see Fig. 3.17b). This divergence is weaker than at $W/t = 0$, and reflects the slow decay of the real space spin-spin correlations. In the superconducting state the spin stiffness vanishes, and one expects a power-law divergence of $\mathrm{Re}\chi(\vec{Q}, \omega = 0)$ as a function of temperature. From this data, we may identify a magnetic energy scale $J \sim 0.5t$ at $W/t = 0.35$. Being a local quantity, J is to first approximation insensitive to lattice size. That J is greater at $W/t = 0.35$ than at $W/t = 0$ may be traced back to the fact that the H_W contains terms of the form $2W \sum_{\vec{i},\vec{\delta}} \vec{S}_{\vec{i}} \cdot \vec{S}_{\vec{i}+\vec{\delta}}$. See Eq. (3.11). At $W/t = 0.35$, and over the entire considered temperature region, $\mathrm{Re}\chi(\vec{q} = 0, \omega = 0)$ is suppressed in comparison to its free electron value (see Fig. 3.17a). We interpret this overall suppression as a signature of pairing fluctuations. For our two largest lattice sizes, $L = 6$ and $L = 8$, $\mathrm{Re}\chi(\vec{q} = 0, \omega = 0)$ shows a maximum at $T \sim 0.5t$ which coincides with our previously determined J scale. The fact that this maximum does not scale with system size (at least for our two largest lattices) makes us believe that it is related to the J scale. In the low temperature limit, and as expected for a superconducting state, the QMC data is consistent with the vanishing of $\mathrm{Re}\chi(\vec{q} = 0, \omega = 0)$. We note that in BCS theory and for a $d_{x^2-y^2}$ order parameter, one obtains: $\mathrm{Re}\chi(\vec{q} = 0, \omega = 0) \sim T$ in the low temperature limit.

We now consider the dynamical structure factor:

$$S(\vec{q},\omega) = \frac{\mathrm{Im}\chi(\vec{q},\omega)}{1-e^{-\beta\omega}} \tag{3.25}$$

where

$$\chi(\vec{q},\omega) = -i\int_0^\infty \mathrm{d}t e^{i(\omega+i\delta)t}\langle[m_z(\vec{q},t),m_z(-\vec{q},0)]\rangle \;\text{ and }\; m_z(\vec{q},t) = e^{itH}m_z(\vec{q})\,e^{-itH}. \tag{3.26}$$

In the above, we have set $\hbar = 1$ and δ is a positive infinitesimal number. $\mathrm{Im}\chi(\vec{q},\omega)$ is obtained by analytically continuing the imaginary time QMC data with the use of the Classic Maximum Entropy method. We have used a flat default model for $S(\vec{q},\omega)$ and imposed the sum rules:

$$\begin{aligned}
&\int_{-\infty}^{\infty}\mathrm{d}\omega\frac{\mathrm{Im}\chi(\vec{q},\omega)}{\omega} = \pi\mathrm{Re}\chi(\vec{q},\omega=0)\\
&\int_{-\infty}^{\infty}\mathrm{d}\omega\mathrm{Im}\chi(\vec{q},\omega)\coth(\beta\omega/2) = 2\pi\langle m_z(\vec{q})\,m_z(-\vec{q})\rangle \;\text{ and}\\
&\int_{-\infty}^{\infty}\mathrm{d}\omega\mathrm{Im}\chi(\vec{q},\omega)\omega = \pi\langle[m_z(-\vec{q}),[H,m_z(\vec{q})]]\rangle.
\end{aligned} \tag{3.27}$$

Fig. 3.18 plots $S(\vec{Q},\omega)$ as a function of temperature at $W/t = 0.35$ on 6×6 and 8×8 lattices. For comparison, we have plotted at the lowest considered temperature, $\beta = 0.1t$, $S(\vec{Q},\omega)$ for the Hubbard model (i.e. $W/t = 0$). $S(\vec{q},\omega)$ satisfies the sum rule:

$$\int_{-\infty}^{\infty}\mathrm{d}\omega S(\vec{q},\omega) = \pi\langle m_z(\vec{q})\,m_z(-\vec{q})\rangle \equiv \pi S(\vec{q}). \tag{3.28}$$

At $W/t = 0$, $S(\vec{Q})$ diverges as L^2 in the zero temperature limit. This weight is centered at $\omega = 0$. At $W/t = 0.35$, and at a scale set by $J \sim 0.5t$, we observe a buildup of spectral weight centered around $\omega = 0$. At a lower temperature scale, which we will identify below, spectral weight is shifted from lower frequencies to form a peak at finite frequency. We define ω_0 by the peak value of $S(\vec{Q},\omega)$ at the lowest considered temperature. Since the equal time spin-spin correlations in the superconducting state decay slower than $\cos(\vec{Q}\vec{r})/|\vec{r}|^2$ at zero temperature, the spectral weight under the peak at ω_0 diverges in the thermodynamic and low temperature limits.

The relaxation rate we consider is defined by,

$$\frac{1}{T_1T} = \lim_{\omega\to 0}\frac{1}{N}\sum_{\vec{q}}\frac{\mathrm{Im}\chi(\vec{q},\omega)}{\omega}, \tag{3.29}$$

where a $\vec{q}$-independent nuclear form factor is assumed. Fig. 3.19 plots $1/T_1$ both in the superconducting and antiferromagnetic insulating state. The *error bars* are obtained in the following way. Let v_τ be a set of imaginary time data, and $C_v(\tau,\tau_1)$ the accompanying covariance matrix. Here $\tau,\tau_1 : 1 \ldots m$. In the basis where the covariance matrix is diagonal, $U^\dagger C_v U = \mathrm{diag}(d_1.....d_m)$, we can add independent noise to the the data in the following way: $\vec{v}_{\vec{\eta}} = U\left(U^\dagger \vec{v} + \vec{\eta}\right)$ where η_τ are Gaussian distributed random variables satisfying $\langle \eta_\tau \rangle = 0$ and $\langle \eta_\tau \eta_{\tau'} \rangle = \delta_{\tau,\tau'} d_\tau$. We carry out the analytical continuation with the data set $\vec{v}_{\vec{\eta}}$ and repeat the procedure for several realizations of $\vec{\eta}$. The *error bars* in Fig. 3.19 correspond to the variance of the so obtained values of $1/T_1$. $1/T_1$ is a delicate quantity to compute with QMC methods. To check the reliability of our calculations we first consider the $W/t = 0$ case. At temperatures $T < J$ as determined from $\mathrm{Re}\chi(\vec{Q}, \omega = 0)$, an increase in $1/T_1$ is observed. This is an expected feature since in the renormalized classical regime of quantum antiferromagnets, $1/T_1$ diverges exponentially with decreasing temperature [18, 19]. In the superconducting state at $W/t = 0.35$, we plot $1/T_1$ as a function of T/ω_0 (see Fig. 3.19a). The overall scale of $1/T_1$ is reduced in the superconducting state as compared to the antiferromagnetic Mott insulating state. For both considered lattice sizes, $1/T_1$ shows a maximum at $T \sim 0.6\omega_0$ which allows us to define a cross-over temperature scale: T_1^{cr}. At temperatures lower than T_1^{cr}, the QMC data is consistent with the vanishing of the relaxation rate $1/T_1$. In BCS theory with a $d_{x^2-y^2}$ order parameter, $1/T_1 \sim T^3$ in the low temperature limit. At temperatures above T_1^{cr}, $1/T_1$ grows with decreasing temperature. One expects $1/T_1$ to start increasing at the magnetic scale J as determined from $\mathrm{Re}\chi(\vec{Q}, \omega = 0)$. Since in Fig. 3.19a we set the temperature scale by ω_0 large size effects are now present in J/ω_0 which takes the values 1.25 (1.92) for the $L = 6$ ($L = 8$) lattice. The so determined cross-over temperature coincides well with the temperature scale at which spectral weight in $S(\vec{Q}, \omega)$ is shifted from low frequencies to form the peak centered at ω_0 (see Fig. 3.18).

3.4 Discussion

The relation of the t-U-W model to high-T_c cuprates is intriguing. We mention the following points.

i) There is substantial evidence that the superconducting state obtained by doping high-T_c cuprates has an order parameter of $d_{x^2-y^2}$ symmetry (For a review see Ref [95]). A similar situation is obtained here by doping the t-U-W model at finite values of W/t. It is important to note that the W term does not explicitly favor d-wave over s-wave symmetry. d-wave is naturally selected due to the underlying spin degrees of freedom.

ii) Photoemission studies of cuprates show a very broad line shape at wave vector $\vec{k} = (0, \pi)$ and at temperatures above T_c. Below T_c a coherent *quasiparticle* like response is observed [96]. Within a numerical approach it is extremely challenging

to obtain line-shapes. We expect the Hubbard model to show a broad line-shape in $A(\vec{k} = (0,\pi), \omega)$ due to the numerically observed flat bands. As W/t is enhanced, we expect, along with the vanishing of those flat bands a more coherent response. The data presented in Figs. 2.8 and 3.3 are not incompatible with the above.
iii) How the magnetic degrees of freedom evolve from the superconducting state at half-filling to the superconducting phase at finite doping is an important open question. In $La_{2-\delta}Sr_\delta CuO_4$, $S(\vec{q},\omega)$, below T_c shows a sharp peak in momentum space centered at the incommensurate wave-vector, $\vec{Q}_\delta = (\pi,\pi) + \delta(\pi,0)$ and at relatively high energies: $\omega > 7meV$ [97]. This indicates that, the magnetic length scale at relatively high energies becomes large ($> 50\mathring{A}$) as the temperature is lowered below T_c. In $YBa_2Cu_3O_{7-\delta}$, a sharp peak in frequency at $30-40$ meV is observed in the superconducting phase [98–100]. There is a possibility that those features are connected to the peak observed numerically at finite frequency in the dynamical spin structure factor. In nuclear magnetic resonance studies of $YBa_2Cu_4O_8$ and $HgBa_2Ca_2Cu_3O_{8+\delta}$, T_{2G} of Cu-sites, which measures predominantly $\mathrm{Re}\chi(\vec{q} = (\pi,\pi), \omega = 0)$ continues to grow monotonically with decreasing temperature even below the temperature scale at which $1/T_1T$ starts decreasing [101, 102]. An extreme case of this feature is seen in our numerical calculations in the superconducting state at $\langle n \rangle = 1$ where in the low temperature limit, $1/T_1T$ scales to zero while $\mathrm{Re}\chi(\vec{q} = (\pi,\pi), \omega = 0)$ diverges.

3.5 Tables and Figures

$\vec{r}$	$P_s^v(\vec{r})$	$P_d^v(\vec{r})$
$(0,0)$	0.2950 ± 0.0018	0.1304 ± 0.0011
$(0,1)$	0.0932 ± 0.0009	0.0238 ± 0.0006
$(0,2)$	0.0076 ± 0.0002	0.0252 ± 0.0003

Table 3.1: Short range vertex contribution to pair-field correlations in the extended-s and d-wave channels. Here we consider an $L = 24$ lattice at $W/t = 0.35$, $U/t = 2$ and $\langle n \rangle = 1$. The boundary conditions are set by $\Phi = \Phi_0/2$. The distance $\vec{r}$ is in units of the lattice constant.

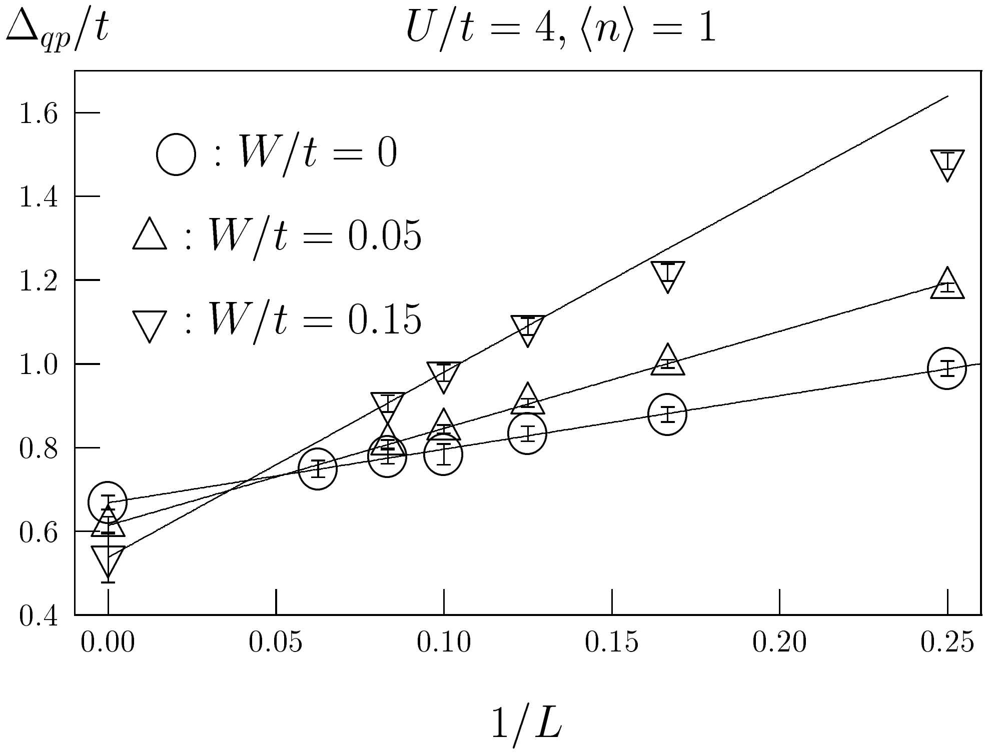

Figure 3.1: The quasiparticle gap $\Delta_{qp} = E_0^{N+1} - E_0^N$ as a function of inverse linear lattice length L at $U/t = 4$ and three values of W/t. The solid lines correspond to least square fits to the form $a + b/L$. The data points at $1/L = 0$, are the so extrapolated values of the quasiparticle gap. At $W/t = 0.15$ the lattice sizes $L = 12, 10$ and 8 were taken into account for the fit.

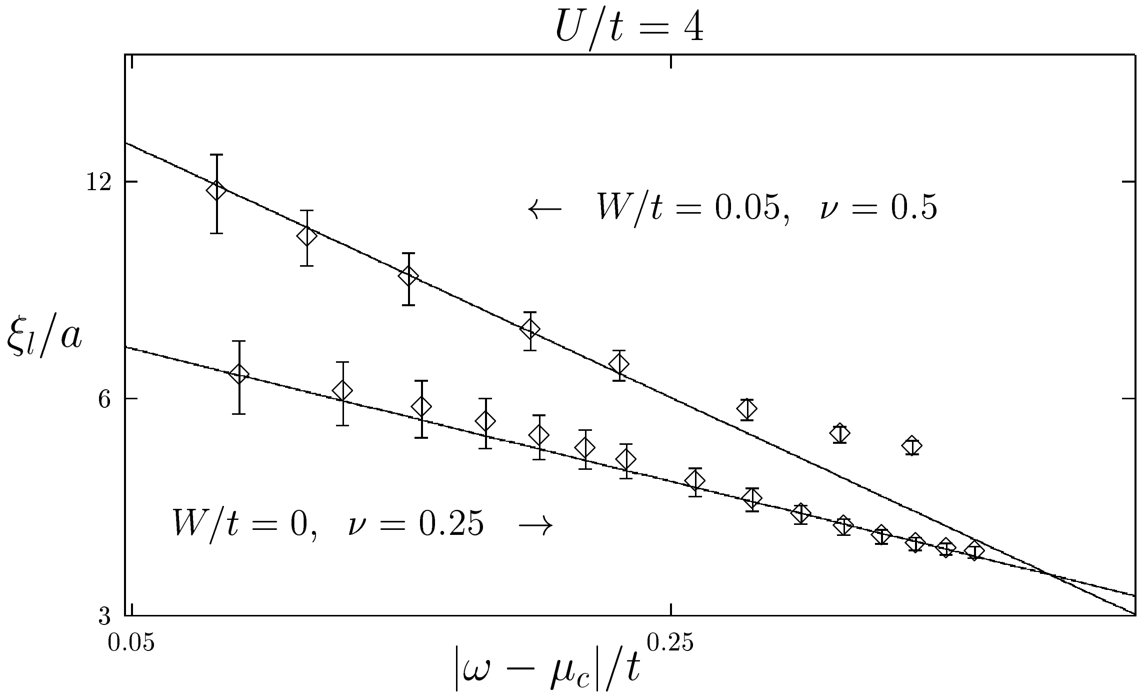

Figure 3.2: The localization length as a function of $|\omega - \mu_c|$. The data at $W/t = 0$, $U/t = 4$ is reproduced from the previous chapter. The solid lines correspond to the form $|\omega - \mu_c|^{-\nu}$ for $\nu = 0.5$ and $\nu = 0.25$. The data is consistent with $|\omega - \mu_c|^{-1/2}$ at $W/t = 0.05$ and $|\omega - \mu_c|^{-1/4}$ at $W/t = 0$.

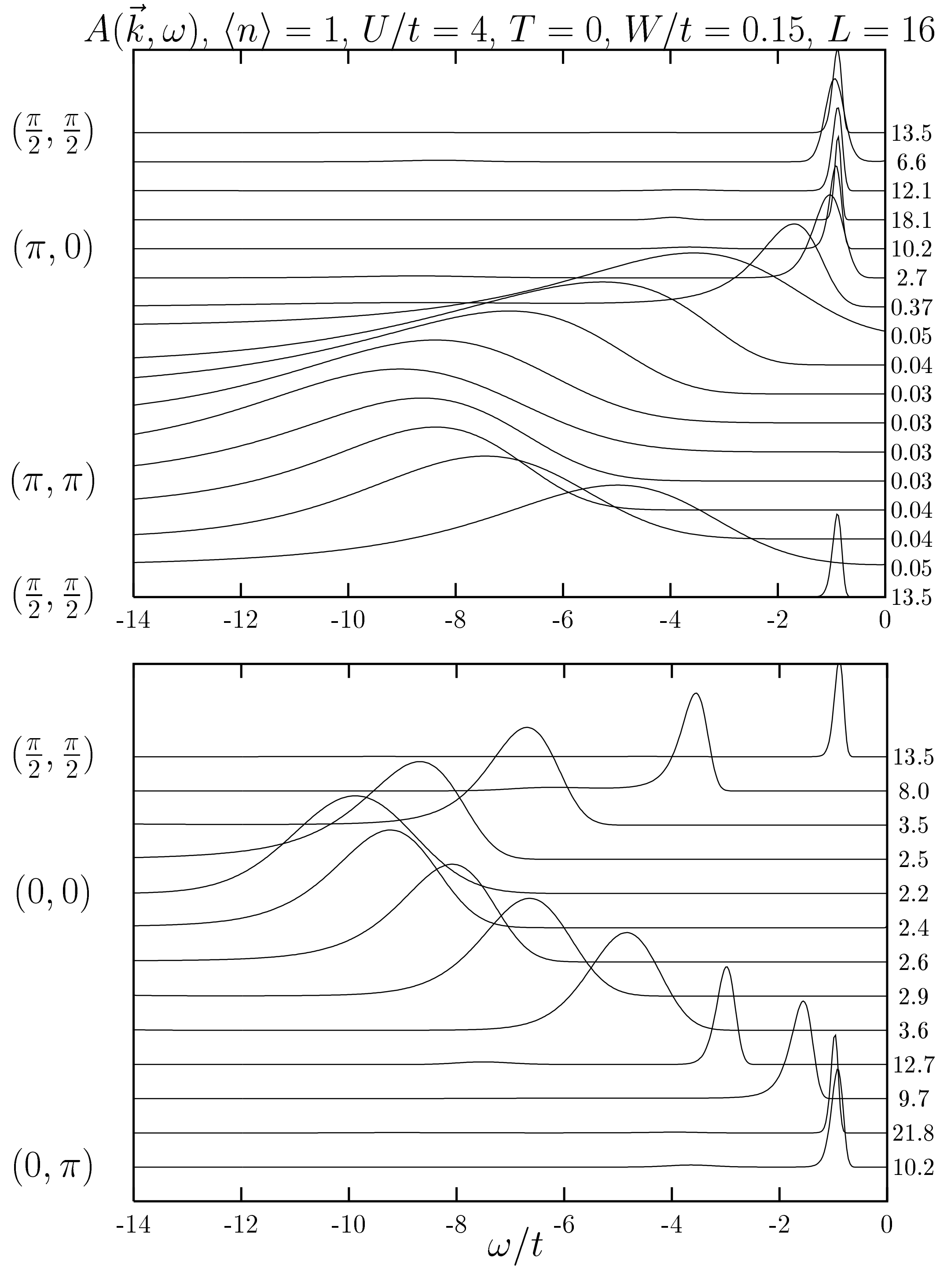

Figure 3.3: $A(\vec{k},\omega)$ at $T=0$ for the half-filled t-U-W model at $U/t=4$, $W/t=0.15$ and on a 16×16 lattice. The considered $\vec{k}$ points in the Brillouin zone are listed on the left hand side of the figure. We have normalized the raw data by the factor listed on the right hand side of the figure. This normalization sets the peak value of $A(\vec{k},\omega)$ to unity for all considered $\vec{k}$ vectors.

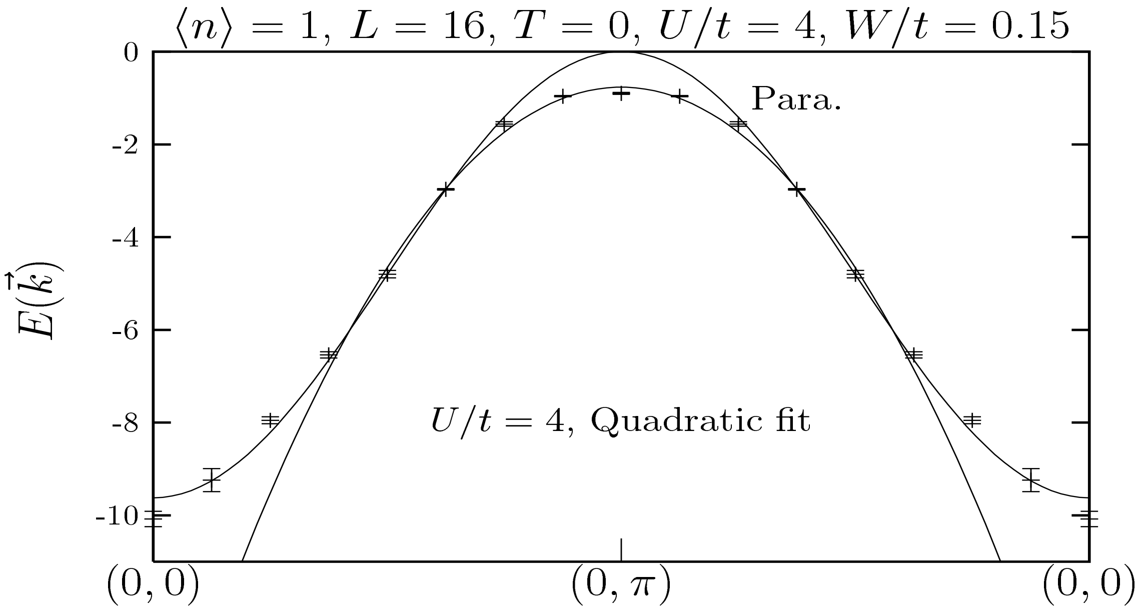

Figure 3.4: Symbols denote the dispersion relation $E(\vec{k})$ as obtained from the the peak position of $A(\vec{k}, \omega)$ presented in Fig. 3.3. The data is compatible with a quadratic fit. For comparison, we have plotted the dispersion relation obtained within the paramagnetic phase (i.e. $m = 0$) of the mean-field approximation presented in Eq. 3.14. To fit better the data, we have used an effective hopping parameter set by $2.4t$ rather the value $2.9t$ predicted by the mean-field approximation.

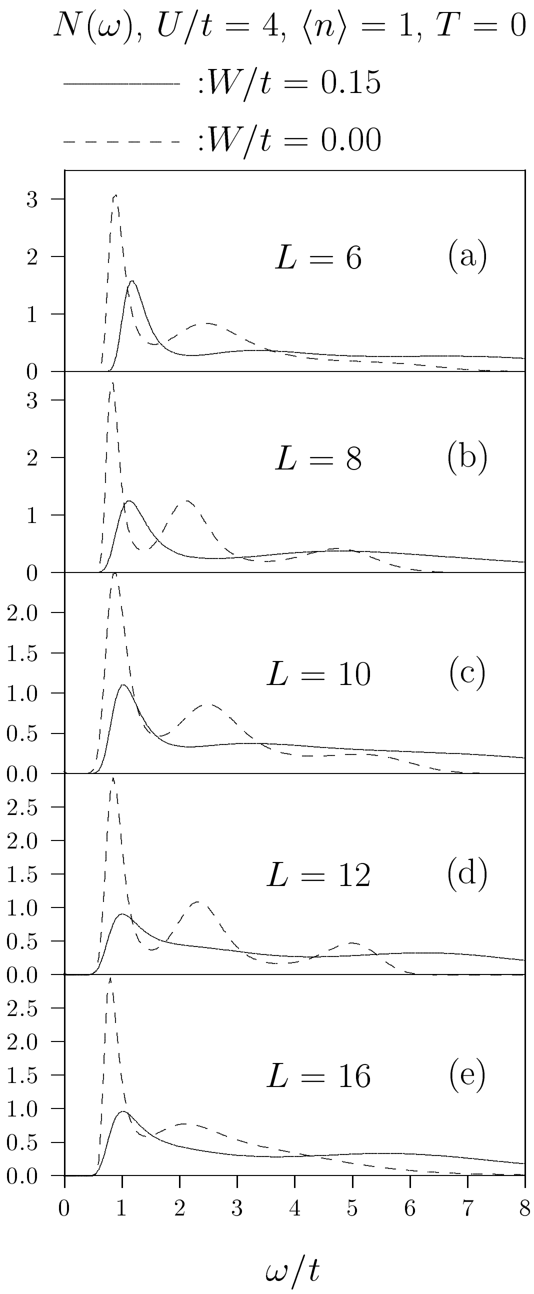

Figure 3.5: $T = 0$ density of states, $N(\omega)$ at half-band filling (i.e. $\mu = 0$), $T = 0$, $U/t = 4$ for lattice sizes ranging from $L = 6$ to $L = 16$. Dashed lines: $W/t = 0$, Solid lines: $W/t = 0.15$.

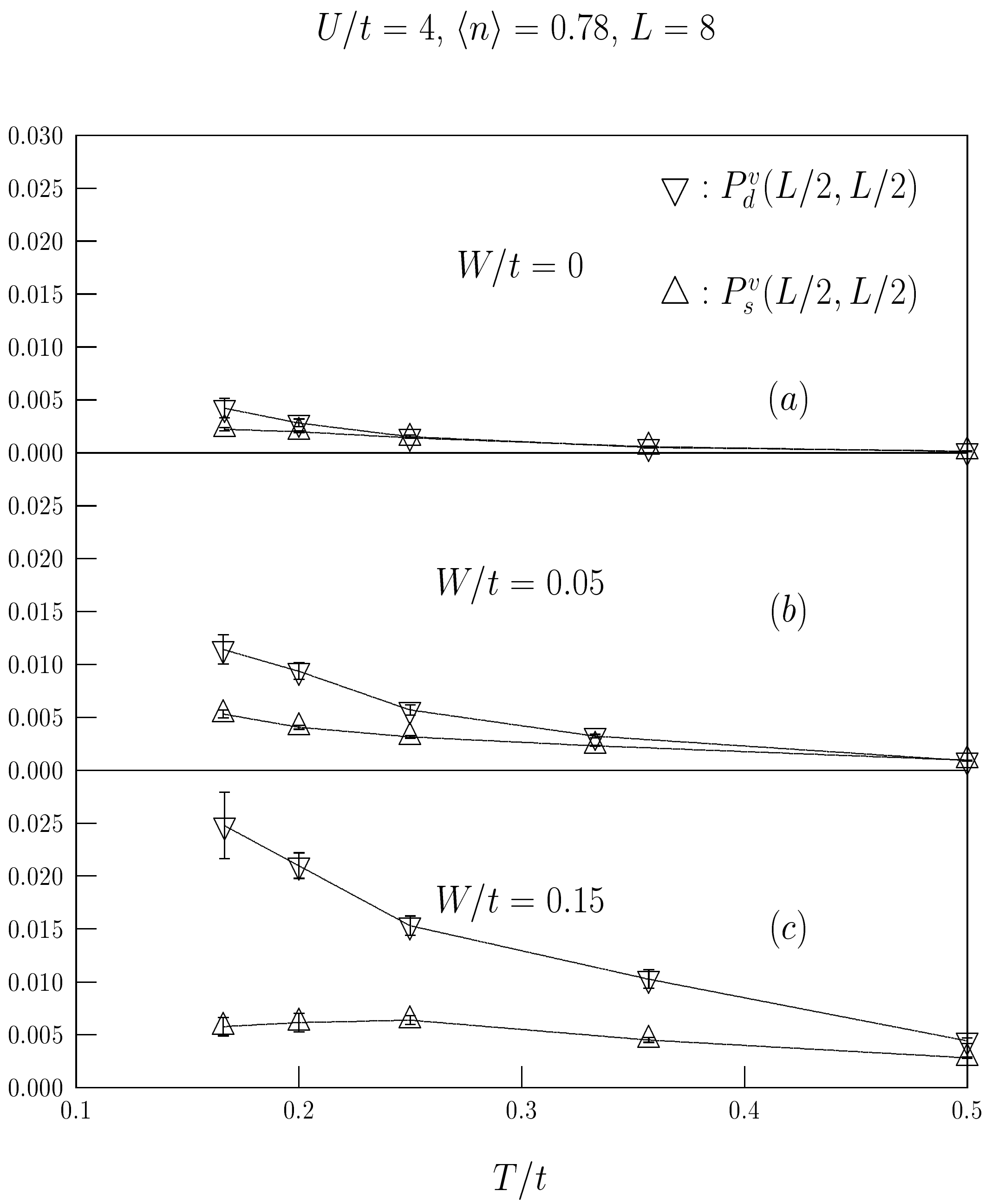

Figure 3.6: Vertex contribution to the pair-field correlations at the largest distance on an $L = 8$ lattice in both the d-wave and extended s-wave channel. The data is plotted versus temperature. Here we fix the particle number to $\langle n \rangle = 0.78$, the Hubbard repulsion to $U/t = 4$ and consider (a) $W/t = 0$, (b) $W/t = 0.05$ and (c) $W/t = 0.15$

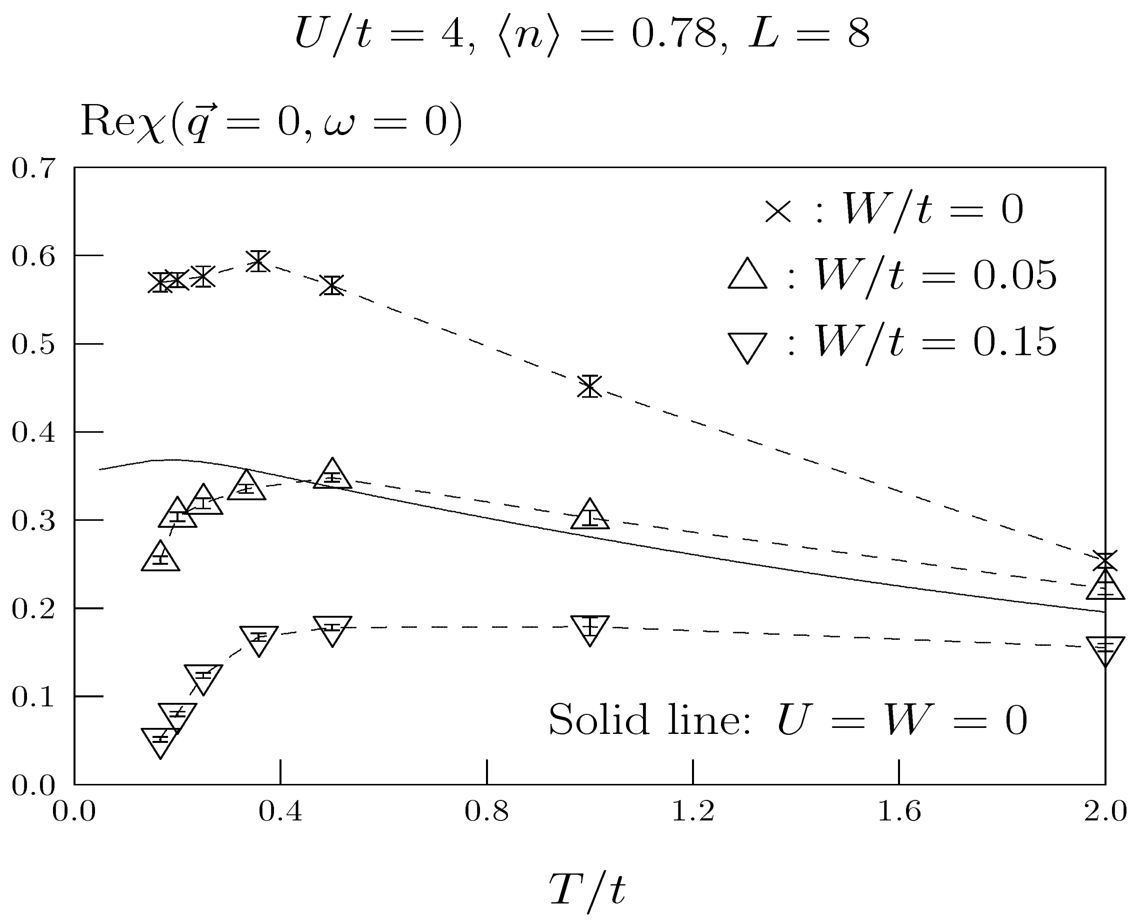

Figure 3.7: Uniform spin susceptibility for the t-U-W model. The solid line corresponds to the spin susceptibility at $U = W = 0$.

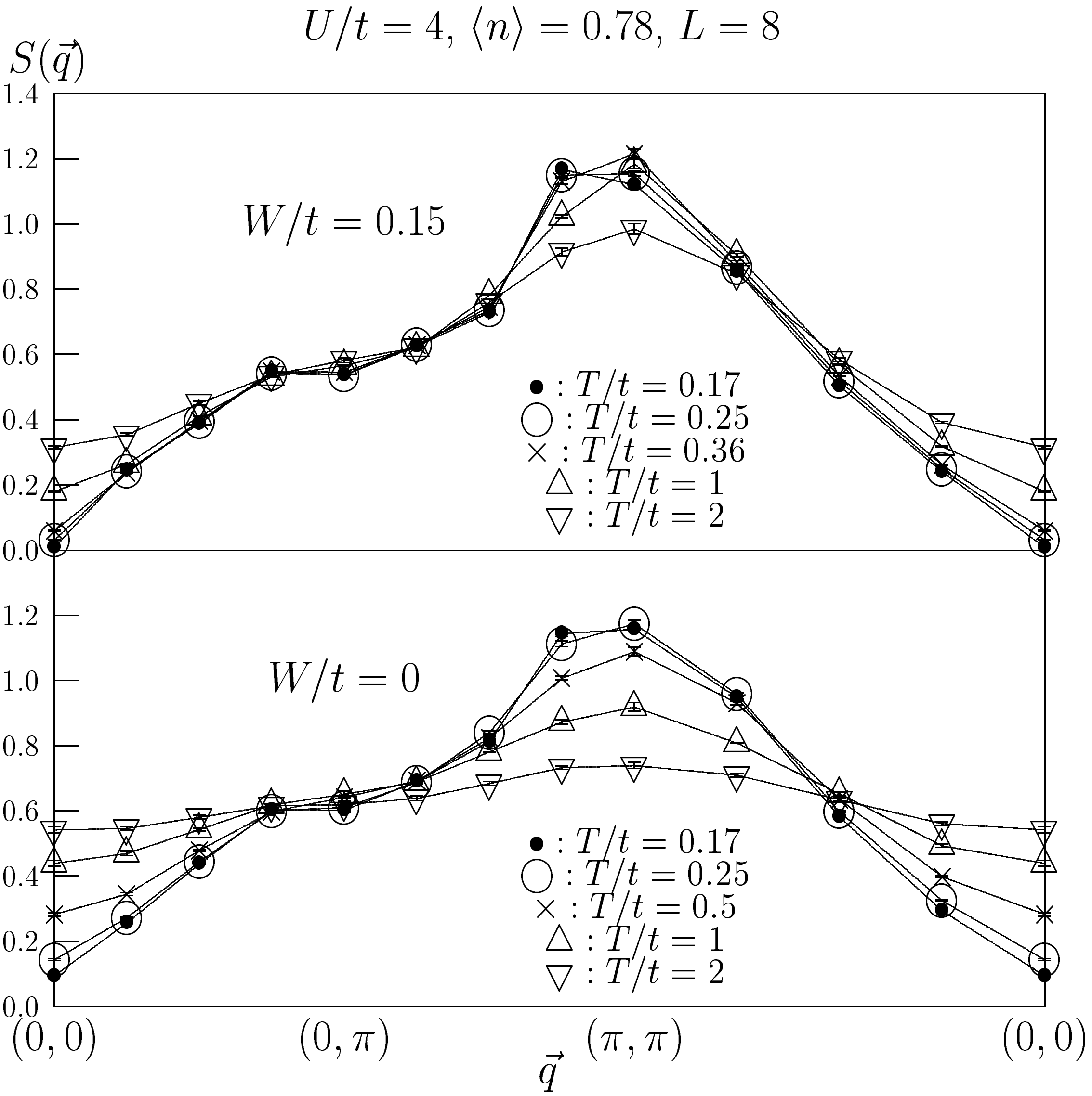

Figure 3.8: Spin structure factor, $S(\vec{q})$, as a function of temperature for the Hubbard and t-U-W models.

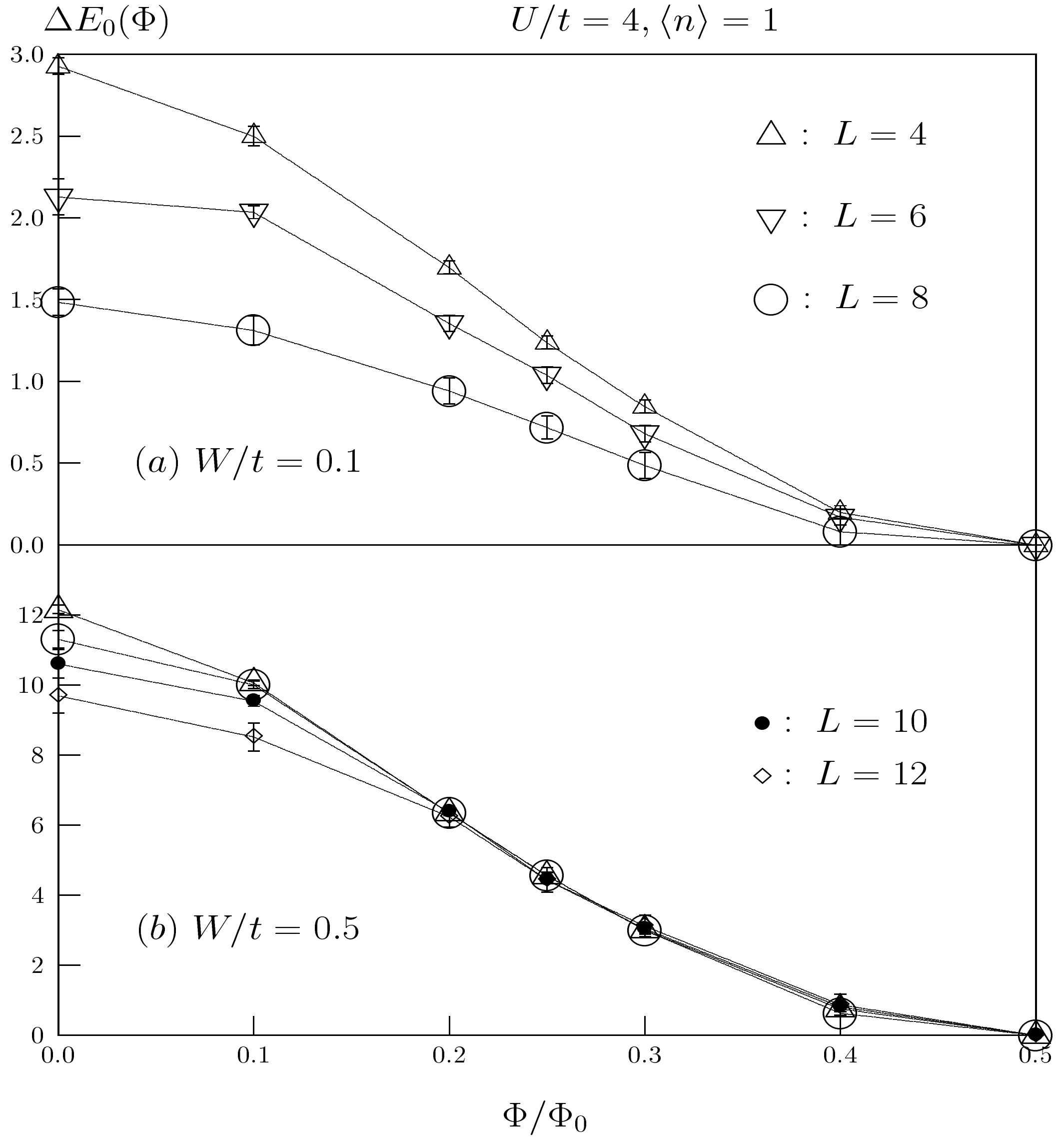

Figure 3.9: $\Delta E_0(\Phi) \equiv E_0(\Phi) - E_0(\Phi_0/2)$ at (a) $W/t = 0.1$ (b) and $W/t = 0.5$

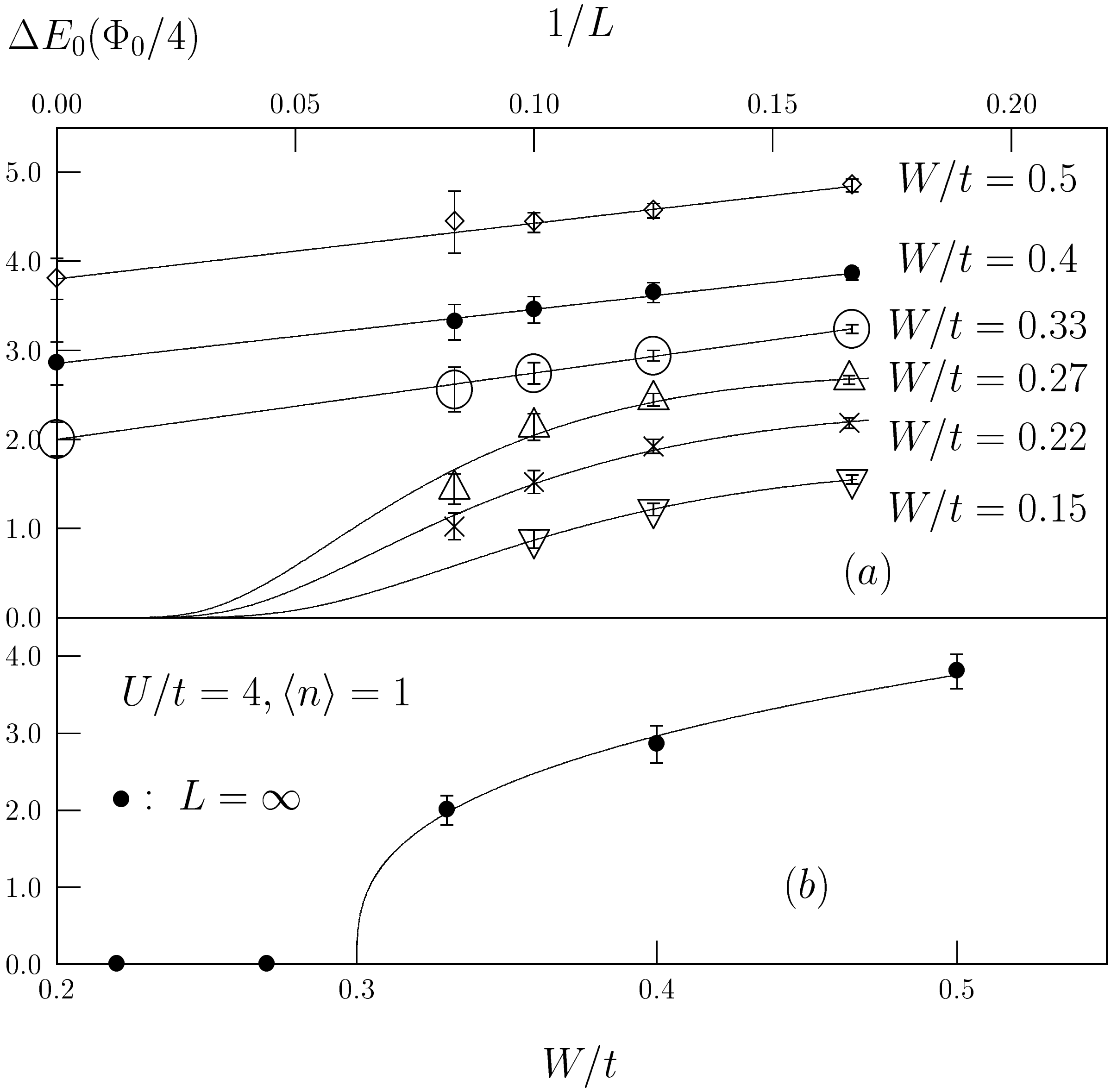

Figure 3.10: (a) $\Delta E_0(\Phi_0/4) \equiv E_0(\Phi_0/4) - E_0(\Phi_0/2)$ versus $1/L$ for several values of W/t. For $W/t < 0.3$ the solid lines correspond to a least square fit of the data to the SDW form: $L \exp(-L/\xi)$. For $W/t > 0.3$ the QMC data is compatible with a $1/L$ scaling to a finite constant. The solid lines are least square fit to this form. (b) Extrapolated value of $\Delta E_0(\Phi_0/4)$ versus W/t. The solid line is a guide to the eye.

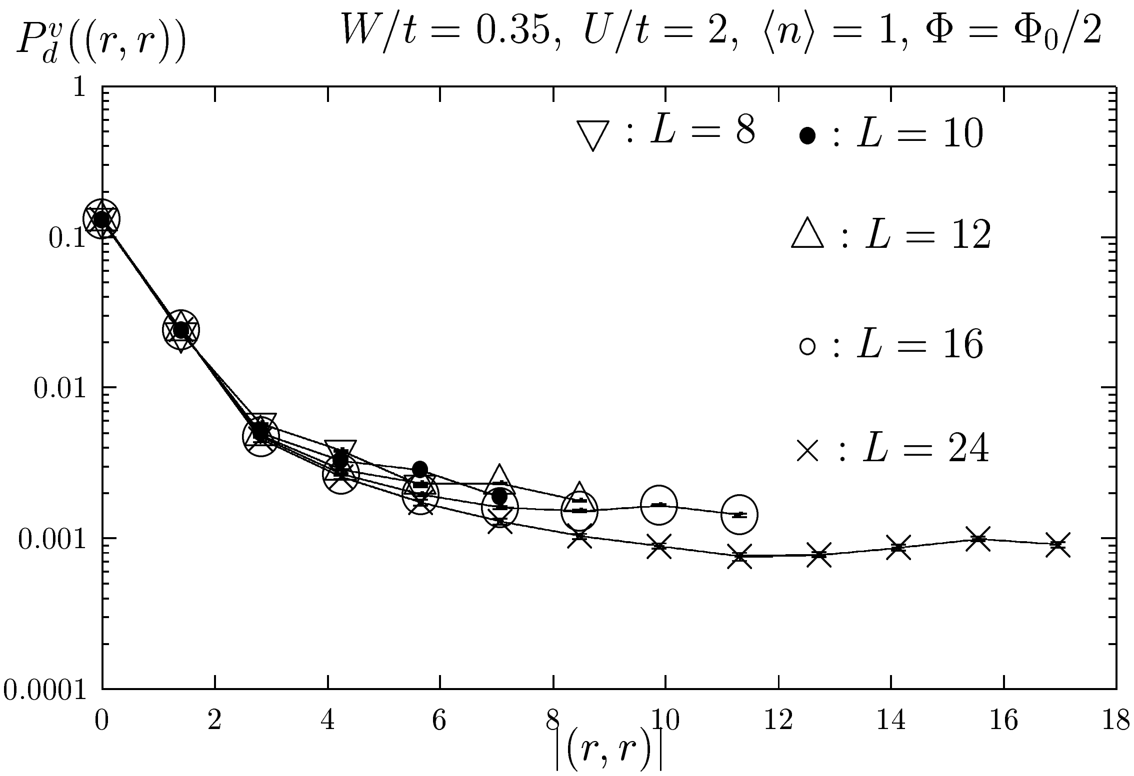

Figure 3.11: Vertex contribution to the d-wave pair field correlations. Here, the temperature is set to $T = 0$.

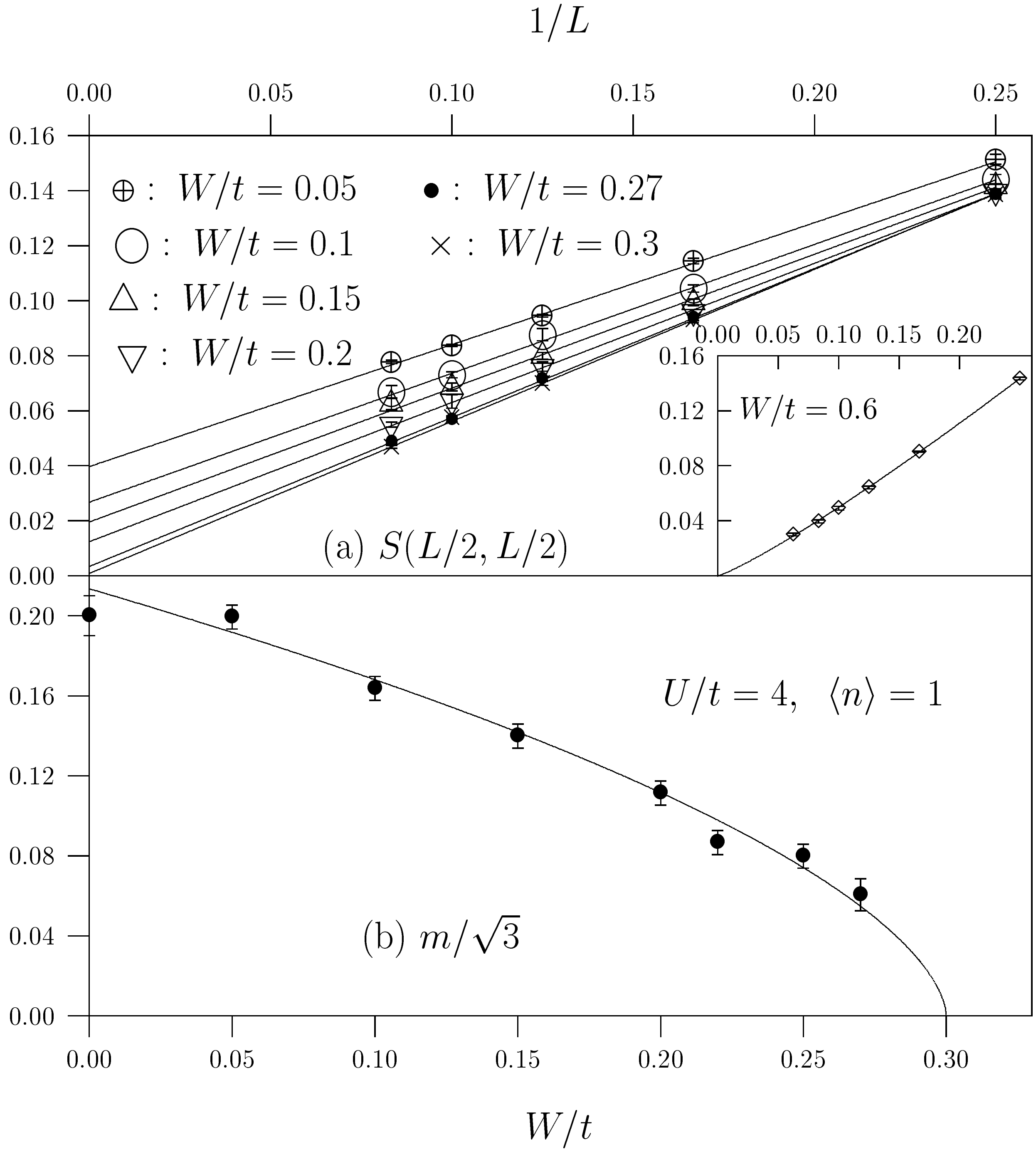

Figure 3.12: (a) $S(L/2, L/2)$ versus $1/L$ for several values of W/t. The solid lines correspond to least square fits of the QMC data to the form $1/L$. Inset: $S(L/2, L/2)$ versus $1/L$ at $W/t = 0.6$. The solid is a least square fit to the form $L^{-\alpha}$. (b) Staggered moment as obtained from (a) versus W/t. The data point at $W/t = 0$ is taken from reference [12]. At $W/t = 0.3$, we were unable to distinguish m from zero within our statistical uncertainty. The solid line is a guide to the eye. The calculations in this figure were carried out at $\Phi = 0$ (see Eq. (3.5)). The $\Delta\tau$ systematic error was extrapolated to zero.

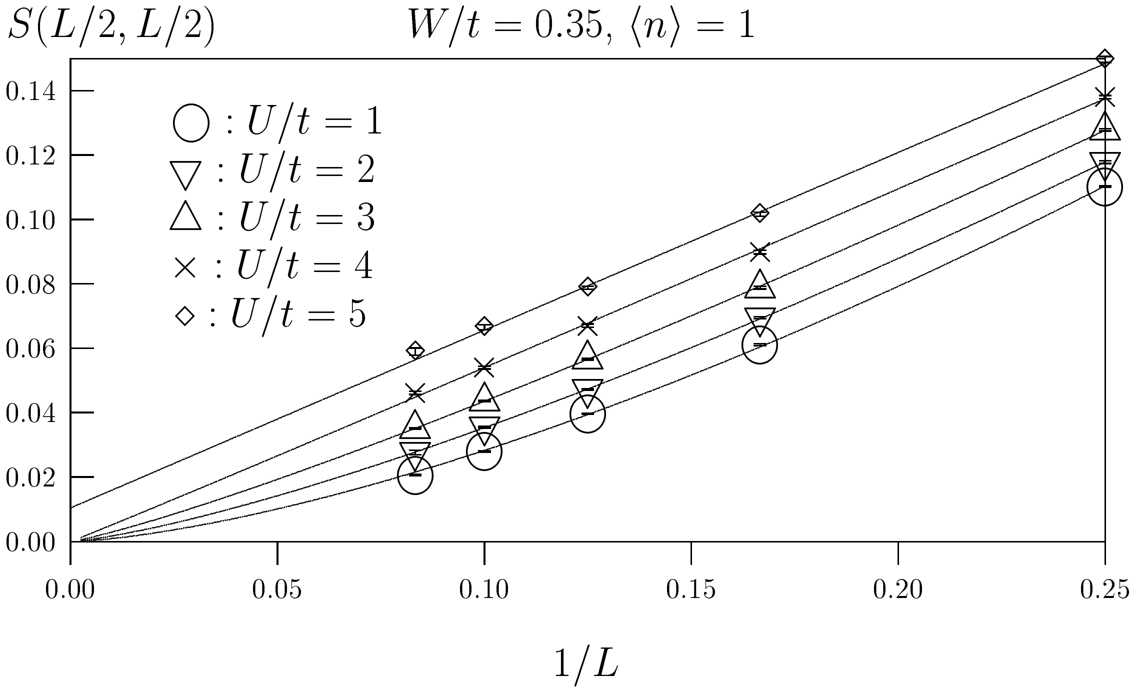

Figure 3.13: $S(L/2, L/2)$ versus $1/L$. The simulations were carried out at $\Phi/\Phi_0 = 0$. Here the $\Delta\tau$ systematic error is extrapolated to zero and the temperature is set to $T = 0$. The solid lines are least square fits to the form: $L^{-\alpha}$. The result of the fit is summarized in Eq. (3.24).

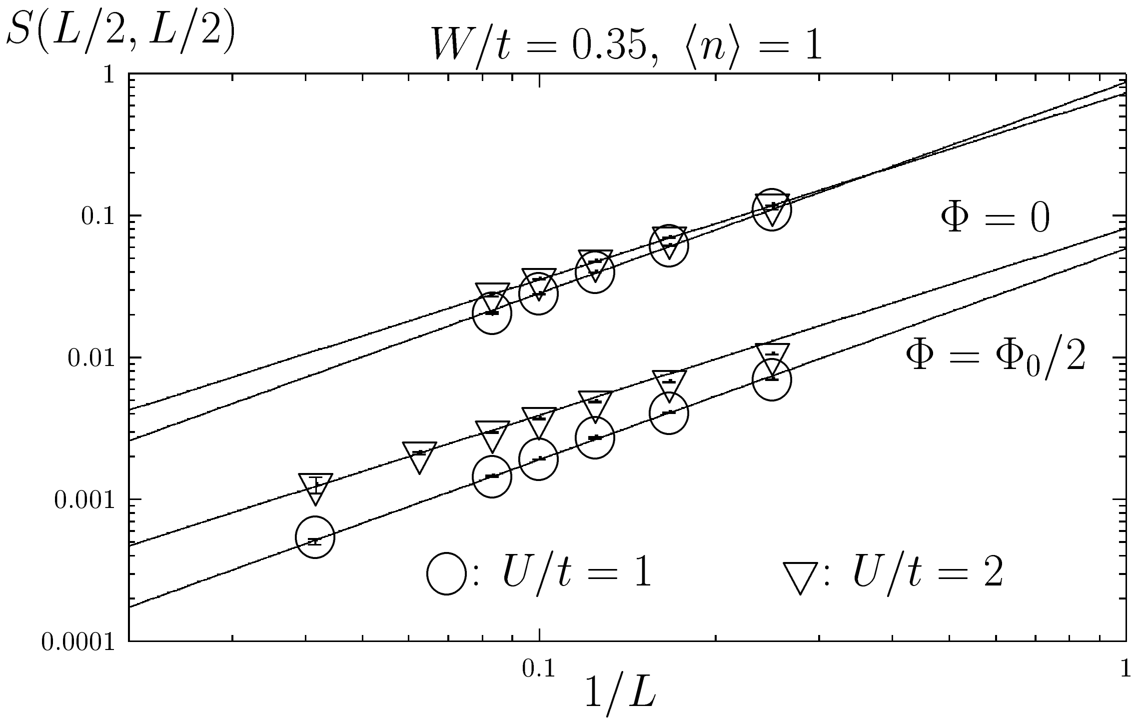

Figure 3.14: $S(L/2, L/2)$ versus $1/L$ for different boundary conditions. The solid line for the $\Phi = 0$ data is obtained from least square fit to the form $L^{-\alpha}$. The same value of the exponent α was used to fit the data at $\Phi = \Phi_0/2$. Here the $\Delta\tau$ systematic error is extrapolated to zero, and $T = 0$.

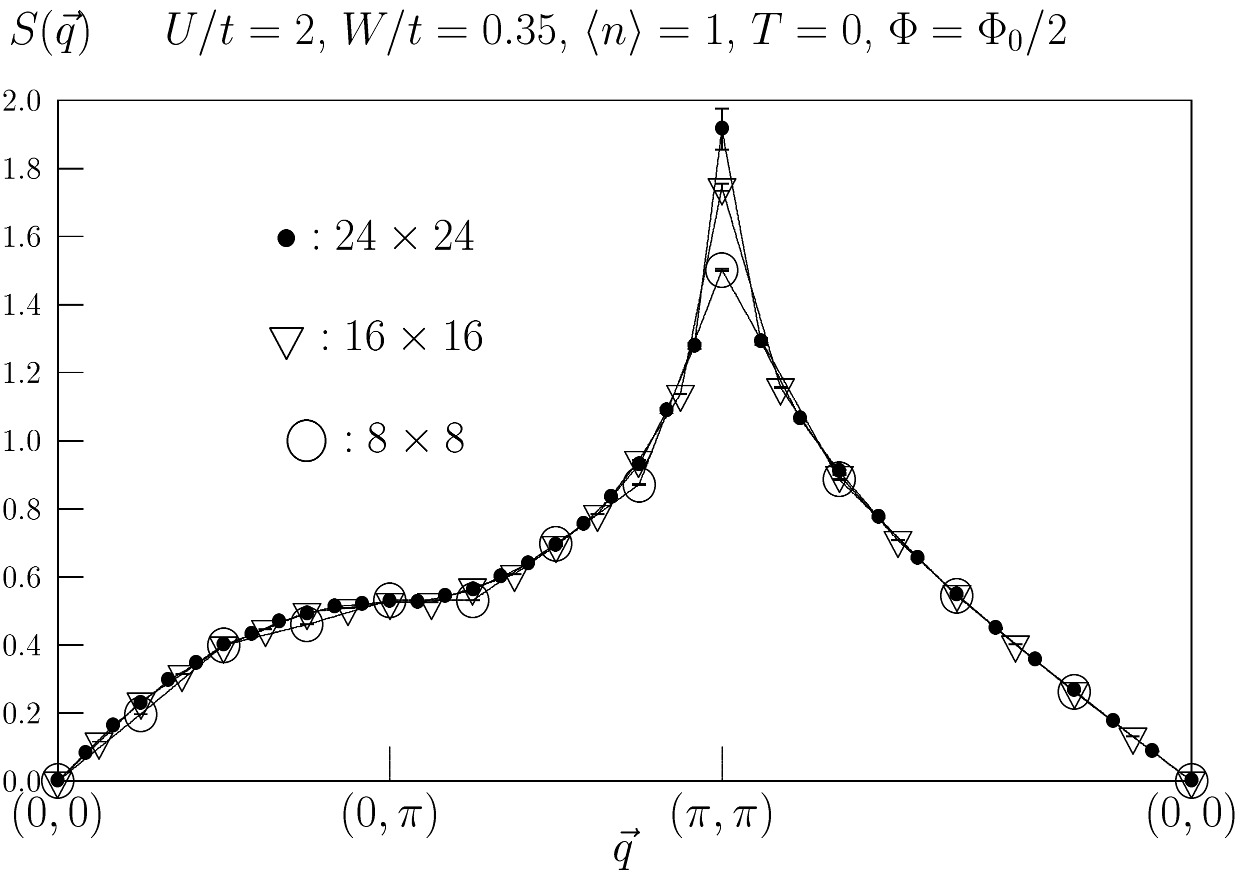

Figure 3.15: Spin structure factor, $S(\vec{q})$, for the t-U-W model in the superconducting phase.

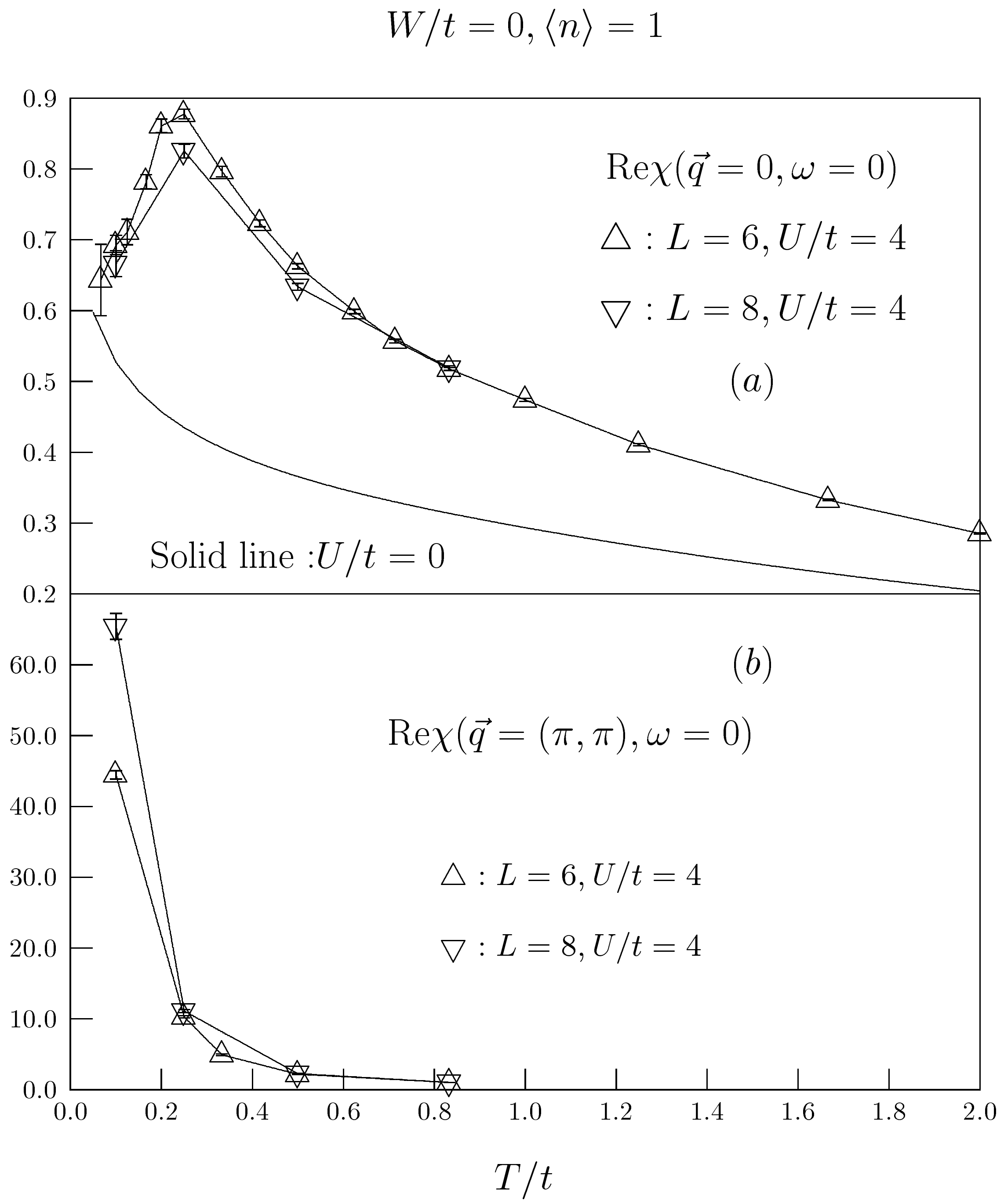

Figure 3.16: (a) Uniform (b) staggered static spin susceptibility for the Hubbard model (i.e. $W/t = 0$) at $U/t = 4$. The solid line with no symbols in (a) corresponds to $\chi(\vec{q} = 0, \omega = 0)$ at $U = W = 0$. The calculations were carried out at $\Phi = 0$ (see Eq. (3.5)).

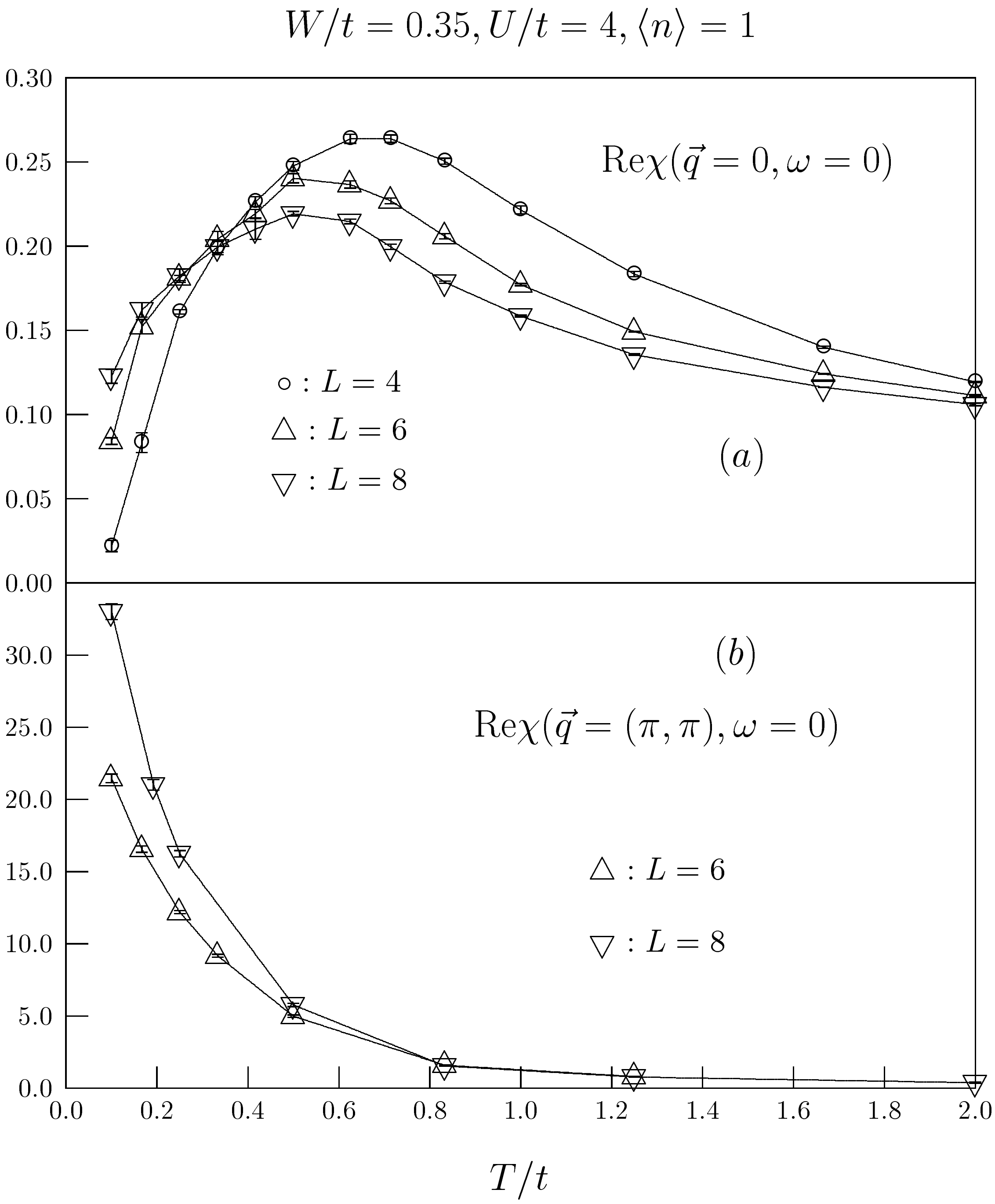

Figure 3.17: (a) Uniform (b) staggered static spin susceptibility in the superconducting state at $W/t = 0.35$ and $U/t = 4$. The calculations were carried out at $\Phi = 0$ (see Eq. (3.5)).

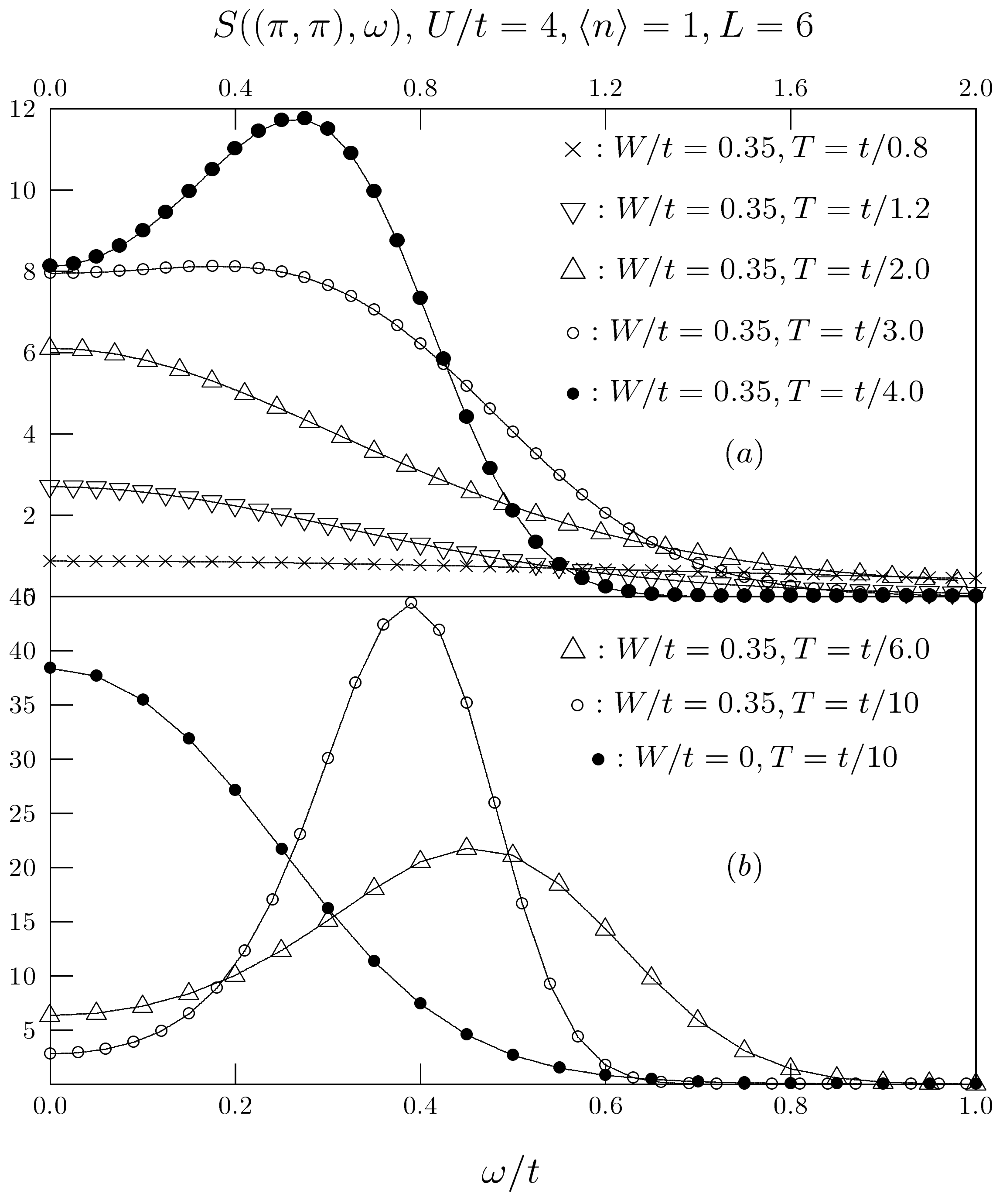

$S((\pi,\pi),\omega)$, $U/t=4, \langle n\rangle = 1, L=6$
0.0
0.4
0.8
1.2
1.6
2.0
12
10
8
6
4
2
0
$\times : W/t = 0.35, T = t/0.8$
$\bigtriangledown : W/t = 0.35, T = t/1.2$
$\bigtriangleup : W/t = 0.35, T = t/2.0$
$\circ : W/t = 0.35, T = t/3.0$
$\bullet : W/t = 0.35, T = t/4.0$
(a)
45
40
35
30
25
20
15
10
5
$\bigtriangleup : W/t = 0.35, T = t/6.0$
$\circ : W/t = 0.35, T = t/10$
$\bullet : W/t = 0, T = t/10$
(b)
0.0
0.2
0.4
0.6
0.8
1.0
ω/t

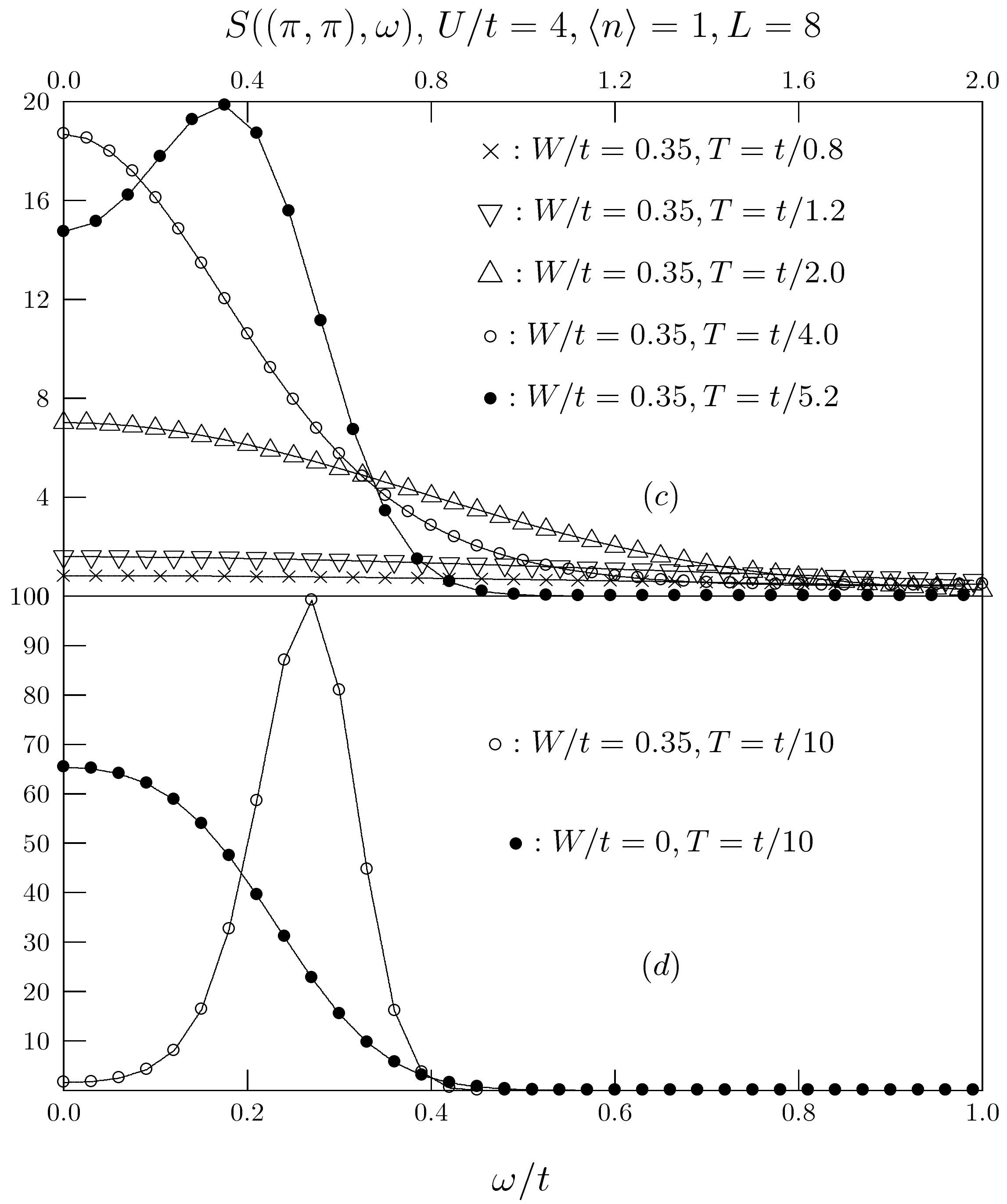

Figure 3.18: $S(\vec{Q},\omega)$ in the superconducting state at $W/t = 0.35$, $U/t = 4$ as a function of system size and temperature. For comparison, at the lowest considered temperature, $T = 0.1t$, we have included the result for the Hubbard model (i.e. $W/t = 0$) at $U/t = 4$. Here, $\Phi = 0$ (see Eq. (3.5)).

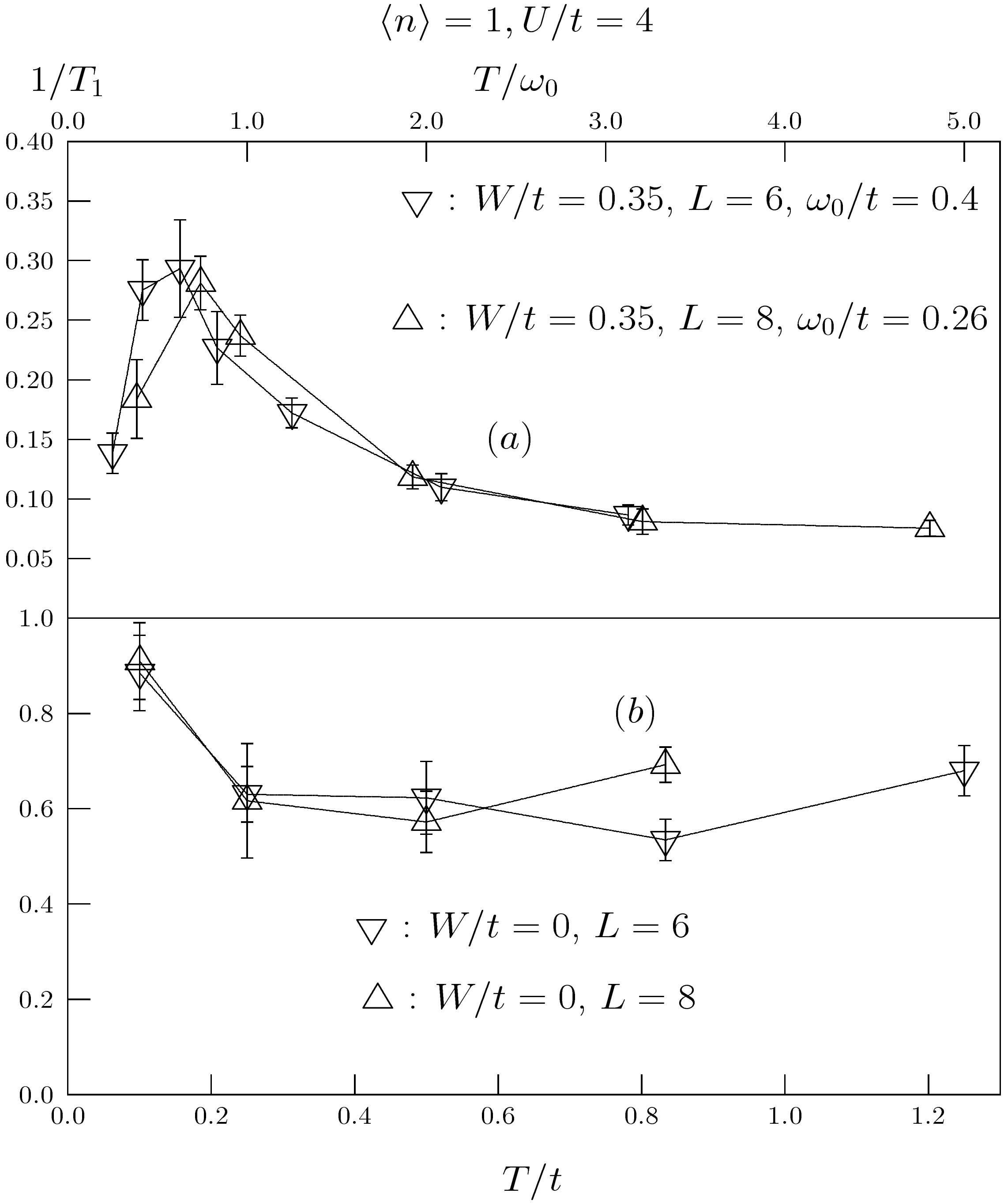

Figure 3.19: (a) $1/T_1$ versus T/ω_0 in the superconducting state at $W/t = 0.35$, $U/t = 4$. The magnetic scale is given by $J \sim 0.5t$. (b). $1/T_1$ versus T for the antiferromagnetic Mott insulating state. Here, $J \sim 0.25t$. The calculations were carried out at $\Phi = 0$ (see Eq. (3.5)).

Chapter 4

Auxiliary Field Quantum Monte Carlo Algorithms

The results described in this article are based on a number of generalizations of the auxiliary field quantum Monte Carlo (QMC) method [46] applied to Hubbard type models. Our work on the high frequency Hall coefficient is based on the generalization of the QMC method to include magnetic fields [63]. We are able to compute the localization length ξ_l only due to the fact that we are able to calculate in a numerically stable way, zero-temperature imaginary time displaced correlation functions [8]. Finally, our work on the t-U-W model is based on a technical trick to incorporate the W term in an efficient way [57]. In this chapter we concentrate on some of those innovations. For a detailed introduction to the determinental (auxiliary field) Monte Carlo method applied to the Hubbard model, we refer the reader to Ref. [103]. For a more general review of numerical methods applied to the study of correlated electron systems, we refer the reader to [35, 104],

We concentrate on the formulation of the zero temperature QMC [48–50] method for the t-U-W model. The extension to the finite temperature QMC algorithm [12, 47] is *straightforward.*

For numerical simulations it is convenient to carry out a canonical transformation: $c_{\vec{i},\sigma} \rightarrow \exp\left(2\pi i \frac{\Phi}{\Phi_0 L} \vec{i}\cdot\vec{a}_x\right) c_{\vec{i},\sigma}$. The t-U-W model may then be written as:

$$H_{tUW} = -\frac{t}{2}\sum_{\vec{i}} K_{\vec{i}}(\Phi) + U\sum_{\vec{i}}(n_{\vec{i},\uparrow}-\frac{1}{2})(n_{\vec{i},\downarrow}-\frac{1}{2}) - W\sum_{\vec{i}}\left[K_{\vec{i}}(\Phi)\right]^2 \tag{4.1}$$

with the hopping kinetic energy

$$K_{\vec{i}}(\Phi) = \sum_{\sigma,\vec{\delta}}\left(c^{\dagger}_{\vec{i},\sigma}c_{\vec{i}+\vec{\delta},\sigma}e^{-i\phi\vec{\delta}\cdot\vec{a}_x} + c^{\dagger}_{\vec{i}+\vec{\delta},\sigma}c_{\vec{i},\sigma}e^{i\phi\vec{\delta}\cdot\vec{a}_x}\right) \tag{4.2}$$

where $\phi = 2\pi\frac{\Phi}{\Phi_0 L}$. The fermionic operators now satisfy periodic boundary conditions:

$$c_{\vec{i}+L\vec{a}_x,\sigma} = c_{\vec{i},\sigma}, \quad c_{\vec{i}+L\vec{a}_y,\sigma} = c_{\vec{i},\sigma}. \tag{4.3}$$

This chapter is organized as follows. In the next section, we will describe the zero temperature or projector QMC (PQMC) algorithm applied to the t-U-W model. The convergence of the PQMC to the ground state strongly depends on the choice of the trial wave function. A description of the trial wave functions used for our calculations is described in Sec. 4.2. In Sec. 4.3 we briefly describe the finite temperature QMC algorithm and in Sec. 4.4 we test and compare both algorithms. The last section is devoted to the numerically stable calculation of zero temperature imaginary time displaced Green functions. We have used this algorithm to compute the localization length as well as to estimate charge gaps.

4.1 Projector quantum Monte Carlo algorithm: PQMC.

The PQMC algorithm is a canonical simulation which produces ground state results. The idea behind the PQMC is to filter out the ground state, $|\Psi_0\rangle$ from a trial wave function $|\Psi_T\rangle$:

$$\frac{\langle\Psi_0|O|\Psi_0\rangle}{\langle\Psi_0|\Psi_0\rangle} = \lim_{\Theta\to\infty} \frac{\langle\Psi_T|e^{-\Theta H} O e^{-\Theta H}|\Psi_T\rangle}{\langle\Psi_T|e^{-2\Theta H}|\Psi_T\rangle} \tag{4.4}$$

The above equation is valid provided that $\langle\Psi_T|\Psi_0\rangle \neq 0$. The Monte Carlo evaluation of the observable O proceeds in the following way. The first step is to carry out a Trotter decomposition of the imaginary time propagation:

$$e^{-2\Theta H} \sim \left(e^{-\Delta\tau H_U} e^{-\Delta\tau H_W^{(1)}} \dots e^{-\Delta\tau H_W^{(n_w)}} e^{-\Delta\tau H_t} \right)^m \tag{4.5}$$

Here, H_t (H_U) denotes the kinetic (potential) term of the Hubbard model, $m\Delta\tau = 2\Theta$ and

$$H_W = \sum_{n=1}^{n_w} H_W^{(n)}, \quad H_W^{(n)} = -W \sum_{r=1}^{N/n_w} K^2_{\vec{k}(n,r)} \text{ and } [K_{\vec{k}(n,r)}, K_{\vec{k}(n,r')}] = 0 \;\forall\; r, r'. \tag{4.6}$$

The above defines the function $\vec{k}(n,r)$, $n = 1 \dots n_w$ and $r = 1 \dots N/n_w$ for an N-site lattice. Hence, $H_W^{(n)}$ is given by a sum of commuting operators. The systematic error produced by the above Trotter decomposition is of the order $\Delta\tau$. However, provided that the operators $H_W^{(n)}$, H_t, H_U, O, as well as the trial wave function $|\Psi_T\rangle$ are simultaneously real representable the prefactor of the systematic error proportional to $\Delta\tau$ in the evaluation of the observable O vanishes [63, 105]. As we will see, this condition is satisfied in our calculations and the systematic error produced by the Trotter decomposition is of order $\Delta\tau^2$.

Having isolated the two-body interaction terms, one may carry out Hubbard Stratonovitch (HS) transformations so as to express the right hand side of equation (4.5) as an imaginary time propagation of non-interacting electrons in an external field. For the Hubbard interaction, it is convenient to carry out a discrete HS decomposition [106] to obtain:

$$e^{-\Delta\tau H_U} = C\sum_{\vec{s}} \exp\left(\sum_{\vec{i},\vec{j},\sigma} c^\dagger_{\vec{i},\sigma} D^\sigma_{\vec{i},\vec{j}}(\vec{s}) c_{\vec{j},\sigma}\right). \tag{4.7}$$

Here $\vec{s}$ denotes a vector of length given by the number of sites, N, of HS Ising fields and

$$D^\sigma_{\vec{i},\vec{j}}(\vec{s}) = \delta_{\vec{i},\vec{j}} \cosh^{-1}\exp\left(\Delta\tau U/2\right) s_{\vec{i}}\sigma. \tag{4.8}$$

The constant $C = \exp(\Delta\tau NU/4)/2^N$ for the N-site system will be dropped below.

For the decomposition of $H_W^{(n)}$ we have used the approximate identity:

$$e^{-\Delta\tau H_W^{(n)}} = C' \sum_{\vec{l}^{(n)}} a^{(n)}(\vec{l}) \exp\left(\sum_{\vec{i},\vec{j},\sigma} c^\dagger_{\vec{i},\sigma} A^{(n)}_{\vec{i},\vec{j}}(\vec{l}) c_{\vec{j},\sigma}\right) + O(\Delta\tau^4) \tag{4.9}$$

where, $\vec{l}^{(n)} = (l^{(n,1)}, \ldots, l^{(n,N/n_w)})$, $l^{(n,r)} = -2,-1,1,2$ for $r = 1 \ldots N/n_w$ and

$$\begin{aligned}
A^{(n)}_{\vec{i},\vec{j}}(\vec{l}) &= \sqrt{\Delta\tau W} \sum_{r=1}^{N/n_w} \eta\left(l^{(n,r)}\right) A^{(n,r)}_{\vec{i},\vec{j}} \\
a^{(n)}(\vec{l}) &= \prod_{r=1}^{N/n_w} \gamma\left(l^{(n,r)}\right) \\
A^{(n,r)}_{\vec{i},\vec{j}} = \quad & \delta_{\vec{i},\vec{k}(n,r)}\left(\delta_{\vec{j},\vec{i}+\vec{a}_x} e^{-i\phi} + \delta_{\vec{j},\vec{i}-\vec{a}_x} e^{i\phi} + \delta_{\vec{j},\vec{i}+\vec{a}_y} + \delta_{\vec{j},\vec{i}-\vec{a}_y}\right) \\
+ \quad & \delta_{\vec{j},\vec{k}(n,r)}\left(\delta_{\vec{i},\vec{j}+\vec{a}_x} e^{i\phi} + \delta_{\vec{i},\vec{j}-\vec{a}_x} e^{-i\phi} + \delta_{\vec{i},\vec{j}+\vec{a}_y} + \delta_{\vec{i},\vec{j}-\vec{a}_y}\right).
\end{aligned} \tag{4.10}$$

The fields η and γ take the values:

$$\begin{aligned}
\gamma(\pm1) = 1 + \sqrt{6}/3, \quad \gamma(\pm2) = 1 - \sqrt{6}/3 \\
\eta(\pm1) = \pm\sqrt{2\left(3-\sqrt{6}\right)}, \quad \eta(\pm2) = \pm\sqrt{2\left(3+\sqrt{6}\right)}
\end{aligned} \tag{4.11}$$

The constant $C' = (1/4)^{N/n_w}$ will also be dropped below. The matrices $A^{(n,r)}$ and $A^{(n,r')}$ commute for all combinations of r and r'. The systematic error produced by the above decomposition of $H_W^{(n)}$ is of order $\Delta\tau^4$ per time slice, and hence produces an overall systematic error of order $\Delta\tau^3$. Compared to the accuracy of the Trotter decomposition (of order $\Delta\tau^2$) this is negligible.

The trial wave function is required to be given by a Slater determinant:

$$
\begin{aligned}
|\Psi_T\rangle = \quad & |\Psi_T^\uparrow\rangle \otimes |\Psi_T^\downarrow\rangle \\
& |\Psi_T^\sigma\rangle = \prod_{n=1}^{N_p^\sigma} \left(\sum_{\vec{i}} c^\dagger_{\vec{i},\sigma} P^\sigma_{\vec{i},n} \right) |0^\sigma\rangle.
\end{aligned}
\tag{4.12}
$$

Here N_p^σ denotes the number of particles in a given spin sector, $|0^\sigma\rangle$ is the vacuum in the spin-σ sector and P^σ is an $N \times N_p^\sigma$ rectangular matrix where N is the number of sites.

The right hand side of Eq. 4.4 may now be written as

$$
\frac{\langle \Psi_T | e^{-\Theta H} O e^{-\Theta H} | \Psi_T \rangle}{\langle \Psi_T | e^{-2\Theta H} | \Psi_T \rangle} = \sum_{\vec{s},\vec{l}} \Pr(\vec{s},\vec{l}) \langle O \rangle_{\vec{s},\vec{l}} \ + O\left(\Delta\tau^2\right) \tag{4.13}
$$

Here,

$$
\Pr(\vec{s},\vec{l}) = \frac{a(\vec{l}) \prod_\sigma \langle \Psi_T^\sigma | U^\sigma_{\vec{s},\vec{l}}(2\Theta, 0) | \Psi_T^\sigma \rangle}{\sum_{\vec{s},\vec{l}} a(\vec{l}) \prod_\sigma \langle \Psi_T^\sigma | U^\sigma_{\vec{s},\vec{l}}(2\Theta, 0) | \Psi_T^\sigma \rangle} \tag{4.14}
$$

The fields $\vec{s}$, $\vec{l}$ acquire an additional time index $\tau : 1 \ldots m$, $a(\vec{l}) = \prod_{r,n,\tau} \gamma\left(l_\tau^{(n,r)}\right)$ and

$$
\begin{aligned}
U^\sigma_{\vec{s},\vec{l}}(\Theta_2, \Theta_1) = \prod_{\tau=\tau_1+1}^{\tau_2} \quad & e^{\sum_{\vec{i},\vec{j}} c^\dagger_{\vec{i},\sigma} D^\sigma_{\vec{i},\vec{j}}(\vec{s}_\tau) c_{\vec{j},\sigma}} e^{\sum_{\vec{i},\vec{j}} c^\dagger_{\vec{i},\sigma} A^{(1)}_{\vec{i},\vec{j}}(\vec{l}_\tau) c_{\vec{j},\sigma}} \ldots \\
& e^{\sum_{\vec{i},\vec{j}} c^\dagger_{\vec{i},\sigma} A^{(nw)}_{\vec{i},\vec{j}}(\vec{l}_\tau) c_{\vec{j},\sigma}} e^{\sum_{\vec{i},\vec{j}} c^\dagger_{\vec{i},\sigma} T_{\vec{i},\vec{j}} c_{\vec{j},\sigma}}
\end{aligned}
\tag{4.15}
$$

Here, $\Theta_1 = \tau_1 \Delta\tau$, $\Theta_2 = \tau_2 \Delta\tau$ and $H_t = \sum_{\vec{i},\vec{j},\sigma} c^\dagger_{\vec{i},\sigma} T_{\vec{i},\vec{j}} c_{\vec{j},\sigma}$ corresponds to the kinetic energy of the Hubbard model. For a given set of fields $\vec{s}$, $\vec{l}$, Wicks theorem applies and it suffices to calculate single-particle Green functions.

$$
(G^\sigma_{\vec{s},\vec{l}}(\Theta,\Theta))_{\vec{i},\vec{j}} = \langle c_{\vec{i},\sigma} c^\dagger_{\vec{j},\sigma} \rangle_{\vec{s},\vec{l}} = \frac{\langle \Psi_T^\sigma | U^\sigma_{\vec{s},\vec{l}}(2\Theta,\Theta) c_{\vec{i},\sigma} c^\dagger_{\vec{j},\sigma} U^\sigma_{\vec{s},\vec{l}}(\Theta,0) | \Psi_T^\sigma \rangle}{\langle \Psi_T^\sigma | U^\sigma_{\vec{s},\vec{l}}(2\Theta,0) | \Psi_T^\sigma \rangle} \tag{4.16}
$$

At this stage, one may integrate out the fermionic degrees of freedom to obtain:

$$
\Pr(\vec{s},\vec{l}) = \frac{a(\vec{l}) \det\left(M^\uparrow(\vec{l},\vec{s})\right) \det\left(M^\downarrow(\vec{l},\vec{s})\right)}{\sum_{\vec{s},\vec{l}} a(\vec{l}) \det\left(M^\uparrow(\vec{l},\vec{s})\right) \det\left(M^\downarrow(\vec{l},\vec{s})\right)}. \tag{4.17}
$$

where

$$
\begin{aligned}
M^\sigma(\vec{l},\vec{s}) \quad &= \quad P^{\dagger,\sigma} B^\sigma_{\vec{s},\vec{l}}(2\Theta,0) P^\sigma \\
& B^\sigma_{\vec{s},\vec{l}}(\Theta_2,\Theta_1) = \prod_{\tau=\tau_1+1}^{\tau_2} e^{D^\sigma_\tau(\vec{s})} e^{A^{(1)}_\tau(\vec{l})} \ldots e^{A^{(nw)}_\tau(\vec{l})} e^{-\Delta\tau T}.
\end{aligned}
\tag{4.18}
$$

The Green functions may be explicitly calculated with:

$$(G^{\sigma}_{\vec{s},\vec{l}}(\Theta,\Theta))_{\vec{i},\vec{j}} = \left(I - B^{\sigma}_{\vec{s},\vec{l}}(\Theta,0) P^{\sigma} M^{\sigma}(\vec{s},\vec{l})^{-1} P^{\dagger,\sigma} B^{\sigma}_{\vec{s},\vec{l}}(2\Theta,\Theta)\right)_{\vec{i},\vec{j}}. \tag{4.19}$$

Here I is the unit matrix, $I_{\vec{i},\vec{j}} = \delta_{\vec{i},\vec{j}}$.

As mentioned previously, the Monte Carlo simulation, for the half-filled case, does not suffer from the sign problem. That $\Pr(\vec{s},\vec{l})$ is positive for all values of the fields $\vec{s}$ and $\vec{l}$ follows by carrying out a particle-hole transformation in say the up spin sector: $c^{\dagger}_{\vec{i},\uparrow} = (-1)^{i_x+i_y} h_{\vec{i},\uparrow}$. Since the electron vacuum $|0^{\uparrow}\rangle$ is given by $|0^{\uparrow}\rangle = \prod_{\vec{i}} h^{\dagger}_{\vec{i},\uparrow}|0^{h,\uparrow}\rangle$ one has

$$|\Psi^{\uparrow}_T\rangle = \prod_{n=1}^{N_p^{\uparrow}} \left(\sum_{\vec{i}} h_{\vec{i},\uparrow}(-1)^{i_x+i_y} P^{\uparrow}_{\vec{i},n}\right) \prod_{\vec{i}} h^{\dagger}_{\vec{i},\uparrow}|0^{h,\uparrow}\rangle \equiv \prod_{n=1}^{N-N_p^{\uparrow}} \left(\sum_{\vec{i}} h^{\dagger}_{\vec{i},\uparrow} \overline{\tilde{P}}_{\vec{i},n}\right) |0^{h,\uparrow}\rangle. \tag{4.20}$$

The above equation defines $\tilde{P}$ and $\overline{\tilde{P}}_{\vec{i},n}$ denotes the complex conjugate of $\tilde{P}_{\vec{i},n}$. Under the above transformation, one has:

$$\det\left(M^{\uparrow}_{\vec{s},\vec{l}}\right) = e^{\alpha \sum_{\vec{i},\tau} s_{\vec{i},\tau}} \overline{\det\left(\tilde{P}^{\dagger} B^{\downarrow}_{\vec{s},\vec{l}}(2\Theta,0)\tilde{P}\right)} \tag{4.21}$$

where $\alpha = \cosh^{-1}\exp(\Delta\tau U/2)$. The complex conjugation comes from the fact that if electrons feel a flux Φ, holes are submitted to a flux $-\Phi$. The complex conjugation changes the sign of the flux Φ. Provided that the particle number in given spin sectors satisfy $N - N_p^{\uparrow} = N_p^{\downarrow}$ and that the trial wave function satisfies $\tilde{P} = P^{\downarrow}$ one has:

$$\det\left(M^{\uparrow}_{\vec{s},\vec{l}}\right) = e^{\alpha \sum_{\vec{i},\tau} s_{\vec{i},\tau}} \overline{\det\left(M^{\downarrow}_{\vec{s},\vec{l}}\right)} \tag{4.22}$$

from which the positivity of the probability distribution $\Pr(\vec{s},\vec{l})$ follows.

The sum over the Hubbard Stratonovitch fields is carried out with Monte Carlo methods. One sweeps sequentially through space time lattice and proposes single spin flip updates. The ratio of new to old probabilities under a local change $l^{(n,r)}_{\tau} \rightarrow l'^{(n,r)}_{\tau}$ is best calculated in a basis where the matrix $A^{(n,r)}_{\vec{i},\vec{j}}$ is diagonal. Since in this basis $A^{(n,r)}_{\vec{i},\vec{j}}$ has only two non-vanishing eigenvalues, the ratio of probabilities involves the knowledge of four Green functions per spin sector. Note that under a proposed local move $s_{\vec{i},\tau} \rightarrow s'_{\vec{i},\tau}$ the ratio of probabilities is given by a single Green function per spin sector. In case of acceptance of the spin flip, the required updating is two times more expensive in the case of an $l^{(n,r)}_{\tau} \rightarrow l'^{(n,r)}_{\tau}$ move than for an $s_{\vec{i},\tau} \rightarrow s'_{\vec{i},\tau}$ move. The numerical stabilization of the algorithm is identical to that used for Hubbard calculations [103].

4.2 Trial wave functions for the PQMC.

In this section we show how to construct trial wave functions which generate no sign problem if $N^{\uparrow} + N^{\downarrow} = N$, and in the special case, $N^{\uparrow} = N^{\downarrow} = N/2$ are spin singlets:

$$\sum_{\vec{i},\vec{j}} \vec{S}_{\vec{i}} \cdot \vec{S}_{\vec{j}} |\Psi_T\rangle = 0 \tag{4.23}$$

where $\vec{S}_{\vec{i}}$ is the spin operator on site $\vec{i}$.

Our starting point is the non-interacting Hamiltonian:

$$H_t = \sum_{\vec{i},\vec{j}} c^{\dagger}_{\vec{i}} T_{\vec{i},\vec{j}} c_{\vec{j}}. \tag{4.24}$$

H_t corresponds to the Hamiltonian (4.1) in the limit $U = W = 0$. We have omitted the spin index, and consider periodic boundary conditions. As in equation 4.1, the flux Φ is included in the hopping matrix T. Let U be the unitary transformation which diagonalizes T: $U^{\dagger} T U = \mathrm{diag}\,(\lambda_1 \dots \lambda_N)$. We define the hole operators by $h_{\vec{i}} = (-1)^{\vec{i}} c^{\dagger}_{\vec{i}}$ as well as

$$\gamma_{\vec{k}} = \sum_{\vec{i}} U^{\dagger}_{\vec{k},\vec{i}} c_{\vec{i}} \ \text{ and } \ \eta_{\vec{k}} = \sum_{\vec{i}} h_{\vec{i}} (-1)^{\vec{i}} U_{\vec{i},\vec{k}}. \tag{4.25}$$

We have used the notation $(-1)^{\vec{i}} = (-1)^{i_x + i_y}$. The above operators satisfy

$$[H_t, \gamma^{\dagger}_{\vec{k}}] = \lambda_{\vec{k}} \gamma^{\dagger}_{\vec{k}} \ \text{ and } \ [H_t, \eta^{\dagger}_{\vec{k}}] = -\lambda_{\vec{k}} \eta^{\dagger}_{\vec{k}}. \tag{4.26}$$

We set the trial wave function in the up spin sector to be the ground state of H_t: $|\Psi^{\uparrow}_T\rangle = \prod_{\vec{k}\epsilon A} \gamma^{\dagger}_{\vec{k}} |0\rangle$, where $|0\rangle$ is the electron vacuum and A is set of $\vec{k}$ points defined by the requirement that $|\Psi_T\rangle$ is the ground state of H_t. By construction $|\Psi^{\uparrow}_T\rangle = \prod_{\vec{k}\epsilon \overline{A}} \eta^{\dagger}_{\vec{k}} |0^h\rangle$, where $|0^h\rangle$ is the hole vacuum and $\overline{A}$ is the complement of A. We may hence define:

$$\begin{aligned} P^{\uparrow}_{\vec{i},\vec{k}} &= U_{\vec{i},\vec{k}} \quad \vec{i} : 1 \dots N, \ \ \vec{k}\epsilon A \\ P^{\downarrow}_{\vec{i},\vec{k}} &= (-1)^{\vec{i}} \overline{U}_{\vec{i},\vec{k}} \quad \vec{i} : 1 \dots N, \ \ \vec{k}\epsilon \overline{A}. \end{aligned} \tag{4.27}$$

With this choice of P^{σ} no sign problem occurs (see Eqs.(4.12), (4.20), (4.21) and (4.22)). We note that the only restriction on the particle number is $N^{\uparrow} + N^{\downarrow} = N$.

In the special case $N^{\uparrow} = N^{\downarrow} = N/2$ the trial wave function $|\Psi_T\rangle = |\Psi^{\uparrow}_T\rangle \otimes |\Psi^{\downarrow}_T\rangle$ satisfies:

$$\begin{aligned} \sum_{\vec{i},\vec{j}} \langle \Psi_T | \vec{S}_{\vec{i}} \cdot \vec{S}_{\vec{j}} | \Psi_T \rangle &= \frac{1}{2} \sum_{\vec{k}} f^{\gamma}(\vec{k}) f^{\eta}(\vec{k}) + \left(f^{\gamma}(\vec{k}) - 1 \right) \left(f^{\eta}(\vec{k}) - 1 \right) \quad \text{where} \\ f^{\eta}(\vec{k}) &= \langle \Psi^{\downarrow}_T | \eta^{\dagger}_{\vec{k}} \eta_{\vec{k}} | \Psi^{\downarrow}_T \rangle \ \text{ and } \ f^{\gamma}(\vec{k}) = \langle \Psi^{\uparrow}_T | \gamma^{\dagger}_{\vec{k}} \gamma_{\vec{k}} | \Psi^{\uparrow}_T \rangle. \end{aligned} \tag{4.28}$$

If the ground state of H_t with $N/2$ particles per spin sector is non-degenerate, then $\sum_{\vec{i},\vec{j}}\langle\Psi_T|\vec{S}_{\vec{i}}\cdot\vec{S}_{\vec{j}}|\Psi_T\rangle$ vanishes, independently of the choice of the unitary transformation U. For non-zero values of the flux Φ (i.e. $\Phi\neq 2\pi n\Phi_0$, n being an integer), this condition is satisfied, and hence a trial wave function showing no sign problem and satisfying (4.23), may easily be constructed numerically.

At $\Phi=0$, the ground state of H_t with $N/2$ particles per spin sector is degenerate, and the total spin of the trial wave function will depend on the choice of the unitary transformation U. In principle, one can use the trial wave function obtained at an *infinitesimal* value of Φ to lift the degeneracy. This procedure would force us to work with complex numbers which enhances the CPU time by a factor three to four. To easily circumvent those problems we define a new Hamiltonian

$$\begin{aligned}\tilde{H}_t = \quad & -t(1-\delta)\sum_{\vec{i}}\left(c^{\dagger}_{\vec{i}}c_{\vec{i}+\vec{a}_y}+\text{H.c.}\right)-t(1-\delta)\sum_{\vec{i}=(2i_x+1,i_y)}\left(c^{\dagger}_{\vec{i}}c_{\vec{i}+\vec{a}_x}+\text{H.c.}\right)\\ & -t(1+\delta)\sum_{\vec{i}=(2i_x,i_y)}\left(c^{\dagger}_{\vec{i}}c_{\vec{i}+\vec{a}_x}+\text{H.c.}\right)\end{aligned}\tag{4.29}$$

with periodic boundary conditions in both lattice directions. For *infinitesimal* values of δ, the ground state of $\tilde{H}_t$ with $N/2$ particles is non-degenerate. Diagonalizing $\tilde{H}_t$ generates an orthogonal matrix U from which one may construct the trial wave function. As we will see in section 4.4, the above trial wave functions provide quick convergence to the ground state. The reason lies in the fact that they are spin singlets and hence orthogonal to spin-wave excitations which constitute the low energy part of the spectrum at least in the case of the half-filled Hubbard model.

Furukawa and Imada [107] have considered trial wave functions given by the solution of the unrestricted Hartree Fock approximation. Depending on the quantity under consideration, rapid convergence is obtained. This approach optimizes the overlap of trial wave function with the ground state but breaks all symmetries. In the special case of half-filling the above described wave functions prove to be more efficient.

4.3 Finite temperature algorithm.

The finite temperature QMC algorithm, is a grand canonical simulation which evaluates:

$$\langle O\rangle=\frac{\text{Tr}\left(e^{-\beta(H-\mu N)}O\right)}{\text{Tr}\left(e^{-\beta(H-\mu N)}\right)}\tag{4.30}$$

where the trace runs over the Fock space and β denotes the inverse temperature. The finite temperature QMC algorithm is conceptually similar to that of the PQMC apart from the numerical stabilization which is more involved [103]. We have used this algorithm for the calculation of the high frequency Hall coefficient. Some special aspects of the algorithm for the calculation of R_H have already been discussed in Sec. 1.3. From the technical point of view, including a magnetic field is similar to including a flux. However, as we will see below, some care has to taken to control the systematic error produced by the Trotter decomposition.

4.4 The $\Delta\tau$ systematic error and convergence to the ground state

The Trotter decomposition present in the above algorithms introduces a systematic error of order $\Delta\tau^2$ provided that the operators $H_W^{(n)}$, H_t, H_U, O, as well as the trial wave function $|\Psi_T\rangle$ are simultaneously real representable [63,105]. In the case of the t-U-W model with finite flux Φ, this may be checked explicitly by calculating the energy with the PQMC algorithm for different values of $\Delta\tau$ with the constraint $\Delta\tau M$ constant. Fig. 4.1 shows such an example. The data follows well an $a + b\Delta\tau^2 + c\Delta\tau^3$ form. Note that the $\Delta\tau^3$ term, originates from the approximate Hubbard Stratonovitch decomposition of H_W.

The assumption that the relevant operators are simultaneously real representable is not generally true. An example where this assumption fails, is obtained in a model of spinless fermions in a transverse magnetic field subject to a nearest-neighbor repulsive interaction. The model is defined by:

$$H = -t \sum_{<\vec{i},\vec{j}>} c^{\dagger}_{\vec{i}} c_{\vec{j}} \exp\left(\frac{2\pi i}{\Phi_0}\int_{\vec{i}}^{\vec{j}} \vec{A} d\vec{l}\right) + \text{H.c.} \ + \frac{V}{2}\sum_{<\vec{i},\vec{j}>} n_{\vec{i}} n_{\vec{j}}. \qquad (4.31)$$

Here, $n_{\vec{i}} = c^{\dagger}_{\vec{i}} c_{\vec{i}}$ and in the Landau gauge $\vec{A}(\vec{x}) = -B(x_2, 0, 0)$ so that $\vec{B} = (0, 0, B)$ and the square lattice lies in the $\vec{e}_1$, $\vec{e}_2$ plane. For this model, the Trotter decomposition as in Eq. (4.5) produces a systematic error of order $\Delta\tau$ (see Fig. 4.2). In order to circumvent this problem it is easy, in the case of the Hubbard model or of the above mentioned model, to modify the algorithm so as to use the symmetric Trotter decomposition:

$$\exp\left(-\Delta\tau\left(H_t + H_U\right)\right) = \exp\left(-\Delta\tau H_t/2\right)\exp\left(-\Delta\tau H_U\right)\exp\left(-\Delta\tau H_t/2\right) + O(\Delta\tau^3). \qquad (4.32)$$

For our work on the Hubbard model presented in the Chap. 1 and 2 we have used the above decomposition. The dependence on $\Delta\tau$ of the energy as well as the spin structure factor at $\vec{Q} = (\pi, \pi)$, $S(\vec{Q}) = \frac{4}{3}\sum_{\vec{r}} e^{i\vec{Q}\vec{r}}\langle \vec{S}_{\vec{r}} \vec{S}_{\vec{0}}\rangle$ is listed in table 4.6. The data is consistent with a $\Delta\tau^2$ behavior.

We now turn to the issue of convergence to the ground state within both the finite temperature algorithm and PQMC algorithm. Fig. 4.3 shows plots of the total energy E as well as the spin structure factor at $\vec{Q} = (\pi, \pi)$, $S(\vec{Q}) = \frac{4}{3}\sum_{\vec{r}} e^{i\vec{Q}\vec{r}}\langle \vec{S}_{\vec{r}}\vec{S}_{\vec{0}}\rangle$ as obtained with the PQMC and finite temperature algorithms. Here we consider the t-U-W model at $U/t = 4$, $W/t = 0.35$ and $\Phi = 0$. For the finite temperature data, we set $\beta = 2\Theta$ and measure the observables with equation (4.30). The same observables are evaluated with equation (4.13) and the above described trial wave function. We set $\Delta\tau = 0.1$ and in the case of the PQMC algorithm measure observables on the ten central time slices. For observables which do not commute with the Hamiltonian, this yields an effective projection parameter $\Theta^{eff} = \Theta - 0.5t$. We consider a 6×6 lattice at $U/t = 4$, $W/t = 0.35$ and $\Phi = 0$. The trial wave function used here, is constructed as shown in Eq. (4.27) and the orthogonal transformation used is obtained by diagonalizing the Hamiltonian of equation (4.29) at a numerically infinitesimal value of δ. We have used this trial wave function for all our calculations at $\Phi = 0$. In the limit of large Θt, both the finite temperature and PQMC results converge to the same value within the error bars. We observe that ground state properties are obtained more efficiently within the PQMC approach. The same behavior is observed in the case of the Hubbard model (see Fig. 4.4).

4.5 Numerically stable algorithm for $T = 0$ calculation of imaginary time green functions.

Our calculation of the charge gap as well as of the localization length presented in Chap. 2 and 3 is based on the knowledge of the imaginary time displaced zero temperature Green functions. This quantity is given by:

$$G_{x,y}(\tau) = \Theta(\tau)\frac{\langle\Psi_0|c_x(\tau)c_y^\dagger|\Psi_0\rangle}{\langle\Psi_0|\Psi_0\rangle} - \Theta(-\tau)\frac{\langle\Psi_0|c_y^\dagger(-\tau)c_x|\Psi_0\rangle}{\langle\Psi_0|\Psi_0\rangle},$$
$$\text{where} \quad c_x(\tau) = e^{\tau(H-\mu N)}c_x e^{-\tau(H-\mu N)}. \tag{4.33}$$

Here $|\Psi_0\rangle$ denotes the ground state of the considered Hamiltonian H and $\Theta(\tau)$ is the Heaviside function. To simplify the notation, the indices x corresponds to the quantum numbers of single particle state, such as location $\vec{i}$ and z-component of spin σ. We note that all quantities are diagonal in the spin indices when using a trial wave function of the form given in Eq. 4.12. μ is the chemical potential which has to satisfy:

$$\lim_{\beta\to\infty}\frac{\mathrm{Tr}\left(e^{-\beta(H-\mu N)}N\right)}{\mathrm{Tr}\left(e^{-\beta(H-\mu N)}\right)} = \frac{\langle\Psi_0|N|\Psi_0\rangle}{\langle\Psi_0|\Psi_0\rangle}, \tag{4.34}$$

in the zero-temperature limit $T \equiv 1/\beta \to 0$. The above equation implies that the chemical potential corresponding to the desired particle density, $n(\mu)$, has to be known prior to the simulation. In a metallic state $n(\mu)$ is in general not known a priori. However, in an insulating state at zero-temperature $n(\mu)$ is constant and in general known for chemical potentials within the charge gap Δ_c. In this situation, the here described algorithm proves to be a powerful tool. The above $T=0$ Green functions have already been calculated with QMC methods by Deisz et al. [76]. Since their algorithm does not incorporate a numerical stabilization scheme, they are restricted to relatively small values of τ (i.e. $\tau = 2.5$ in units of the hopping matrix element for the one-dimensional Hubbard model). Here we follow the work of Deisz et al. [76] and describe a numerical stabilization scheme which allows one to calculate $T=0$ Green functions for arbitrary values of τ.

Since the t-U-W model conserves particle number, and we are working in the canonical ensemble, one may factorize the chemical potential to obtain:

$$G_{x,y}(\tau) = \Theta(\tau) \left. \frac{\langle \Psi_0 | c_x(\tau) c_y^\dagger | \Psi_0 \rangle}{\langle \Psi_0 | \Psi_0 \rangle} \right|_{\mu=0} e^{\tau\mu} - \Theta(-\tau) \left. \frac{\langle \Psi_0 | c_y^\dagger(-\tau) c_x | \Psi_0 \rangle}{\langle \Psi_0 | \Psi_0 \rangle} \right|_{\mu=0} e^{\tau\mu}. \quad (4.35)$$

Due to the above relation we consider the calculation of the $T=0$ Green functions at $\mu = 0$.

In the spirit of equation 4.4 we write:

$$\frac{\langle \Psi_0 | c_x(\tau) c_y^\dagger | \Psi_0 \rangle}{\langle \Psi_0 | \Psi_0 \rangle} = \lim_{\Theta\to\infty} \frac{\langle \Psi_T | e^{-\Theta H} c_x(\tau) c_y^\dagger e^{-\Theta H} | \Psi_T \rangle}{\langle \Psi_T | e^{-2\Theta H} | \Psi_T \rangle}, \quad \tau > 0. \qquad (4.36)$$

The QMC calculation of

$$G^>_{x,y}(\Theta, \tau) \equiv \frac{\langle \Psi_T | e^{-\Theta H} c_x(\tau) c_y^\dagger e^{-\Theta H} | \Psi_T \rangle}{\langle \Psi_T | e^{-2\Theta H} | \Psi_T \rangle} \qquad (4.37)$$

proceeds in a similar way as in section 4.1 and $G^>_{x,y}(\Theta,\tau)$ is given by:

$$G^>_{x,y}(\Theta, \tau) = \frac{\sum_{\vec{s},\vec{l}} \langle \Psi_T | U_{\vec{s},\vec{l}}(2\Theta, \Theta+\tau) c_x U_{\vec{s},\vec{l}}(\Theta+\tau, \Theta) c_y^\dagger U_{\vec{s},\vec{l}}(\Theta, 0) | \Psi_T \rangle}{\sum_{\vec{s},\vec{l}} \langle \Psi_T | U_{\vec{s},\vec{l}}(2\Theta, 0) | \Psi_T \rangle} + O((\Delta\tau)^2). \qquad (4.38)$$

Since $U_{\vec{s},\vec{l}}(2\Theta, 0)$ describes the propagation of non-interacting electrons in an external HS field, one may integrate out the fermionic degrees of freedom to obtain:

$$G^>_{x,y}(\Theta, \tau) = \sum_{\vec{s},\vec{l}} \mathrm{Pr}_{\vec{s},\vec{l}} \left[\Big(B_{\vec{s},\vec{l}}(\Theta+\tau, \Theta) \Big) G_{\vec{s},\vec{l}}(\Theta, \Theta) \right]_{x,y} + O((\Delta\tau)^2). \qquad (4.39)$$

Similarly, one obtains:

$$\begin{aligned} G^<_{x,y}(\Theta, \tau) &\equiv -\frac{\langle \Psi_T | e^{-\Theta H} c_y^\dagger(\tau) c_x e^{-\Theta H} | \Psi_T \rangle}{\langle \Psi_T | e^{-2\Theta H} | \Psi_T \rangle} \\ &= \sum_{\vec{s},\vec{l}} \mathrm{Pr}_{\vec{s},\vec{l}} \left[\Big(G_{\vec{s},\vec{l}}(\Theta, \Theta) - I \Big) B^{-1}_{\vec{s},\vec{l}}(\Theta+\tau, \Theta) \right]_{x,y}, \quad \tau > 0. \quad (4.40) \end{aligned}$$

Thus, the zero-temperature imaginary-time Green function may be calculated from:

$$G_{x,y}(\tau) = \lim_{\Theta\to\infty} \Big(\Theta(\tau) G^>_{x,y}(\Theta, \tau) + \Theta(-\tau) G^<_{x,y}(\Theta, -\tau) \Big) + O((\Delta\tau)^2). \qquad (4.41)$$

4.5.1 Numerical Stabilization

The origin of the numerical instabilities occurring in the calculation of Green functions may be understood by considering free electrons on a two-dimensional square lattice.

$$H = -t \sum_{<\vec{i},\vec{j}>} c^{\dagger}_{\vec{i}} c_{\vec{j}} + \text{H.c.}. \tag{4.42}$$

Here, the sum runs over nearest-neighbors. For this Hamiltonian one has:

$$\langle \Psi_0 | c^{\dagger}_{\vec{k}}(\tau) c_{\vec{k}} | \Psi_0 \rangle = \exp\Big(\tau(\epsilon_{\vec{k}} - \mu)\Big) \langle \Psi_0 | c^{\dagger}_{\vec{k}} c_{\vec{k}} | \Psi_0 \rangle, \tag{4.43}$$

where $\epsilon_{\vec{k}} = -2t(\cos(\vec{k}\vec{a}_x) + \cos(\vec{k}\vec{a}_y))$, $\vec{a}_x$, $\vec{a}_y$ being the lattice constants. The chemical potential satisfies eq. (4.34) and we will assume $|\Psi_0\rangle$ to be non-degenerate. In a numerical calculation the eigenvalues and eigenvectors of the above Hamiltonian will be known up to machine precision, ϵ. In the case $\epsilon_{\vec{k}} - \mu > 0$, $\langle \Psi_0 | c^{\dagger}_{\vec{k}} c_{\vec{k}} | \Psi_0 \rangle \equiv 0$. However, on a finite precision machine the later quantity will take a value of the order of ϵ. When calculating $\langle \Psi_0 | c^{\dagger}_{\vec{k}}(\tau) c_{\vec{k}} | \Psi_0 \rangle$ this roundoff error will be blown up exponentially and the result for large values of τ will be unreliable. In order to circumvent this problem, one may do the calculation at finite temperature and then take the limit of vanishingly small temperatures:

$$\langle \Psi_0 | c^{\dagger}_{\vec{k}}(\tau) c_{\vec{k}} | \Psi_0 \rangle = \lim_{\beta \to \infty} \frac{\exp\Big(\tau(\epsilon_{\vec{k}} - \mu)\Big)}{1 + \exp\Big(\beta(\epsilon_{\vec{k}} - \mu)\Big)}. \tag{4.44}$$

Even if the eigenvalues are known only up to machine precision, the right hand side of the above equation for large but finite values of β is a numerically stable operation. Although very simple, this example reflects the underlying numerical instabilities occurring in the calculation of the Green functions.

We now consider the calculation of

$$\begin{aligned} G_{\vec{s},\vec{l}}(\Theta + \tau, \Theta) &= B_{\vec{s},\vec{l}}(\Theta + \tau, \Theta) G_{\vec{s},\vec{l}}(\Theta, \Theta) \quad \text{and} \\ G_{\vec{s},\vec{l}}(\Theta, \Theta + \tau) &= \Big(G_{\vec{s},\vec{l}}(\Theta, \Theta) - I\Big) B^{-1}_{\vec{s},\vec{l}}(\Theta + \tau, \Theta) \end{aligned} \tag{4.45}$$

required to compute $G^{>}_{x,y}(\Theta, \tau)$ (see eq. (4.39)) and $G^{<}_{x,y}(\Theta, \tau)$ (see eq. (4.40)) respectively. The equal-time Green functions, $G_{\vec{s},\vec{l}}(\Theta, \Theta)$, may be calculated to machine precision [49, 50, 108, 109]. The matrices $B_{\vec{s},\vec{l}}(\Theta + \tau, \Theta)$ contain scales which grow and decrease exponentially with τ. As in the above example, a straightforward multiplication of both matrices will lead to numerical instabilities for large values of τ. Here, the problem is much more severe since the presence of the HS field mixes different scales. In order to circumvent this problem, we propose the following stabilization scheme.

Since the trial wave function is a Slater determinant, we can find a single particle Hamiltonian, $H_0 = \sum_{x,y} c_x^\dagger (h_0)_{x,y} c_y$, which has $|\Psi_T\rangle$ as a non-degenerate ground state. The equal time Green functions may then be written as:

$$
\begin{aligned}
\left(G_{\vec{s},\vec{l}}(\Theta,\Theta)\right)_{x,y} &\equiv \frac{\langle \Psi_T | U_{\vec{s},\vec{l}}(2\Theta,\Theta) c_x c_y^\dagger U_{\vec{s},\vec{l}}(\Theta,0) | \Psi_T\rangle}{\langle \Psi_T | U_{\vec{s},\vec{l}}(2\Theta,0) | \Psi_T\rangle} \\
&= \lim_{\beta\to\infty} \frac{\mathrm{Tr}\left(e^{-\beta H_0} U_{\vec{s},\vec{l}}(2\Theta,\Theta) c_x c_y^\dagger U_{\vec{s},\vec{l}}(\Theta,0)\right)}{\mathrm{Tr}\left(e^{-\beta H_0} U_{\vec{s},\vec{l}}(2\Theta,0)\right)} \\
&= \lim_{\beta\to\infty} \left(I + B_{\vec{s},\vec{l}}(\Theta,0) e^{-\beta h_0} B_{\vec{s},\vec{l}}(2\Theta,\Theta)\right)^{-1}_{x,y} \qquad (4.46)
\end{aligned}
$$

The last equality follows after integration of the fermionic degrees of freedom. Inspiring ourselves from the work of Hirsch [110] we calculate the time displaced Green functions in eq. (4.45) with:

$$
\lim_{\beta\to\infty} \begin{pmatrix} I & B_{\vec{s},\vec{l}}(\Theta,0) e^{-\beta h_0} B_{\vec{s},\vec{l}}(2\Theta,\Theta+\tau) \\ -B_{\vec{s},\vec{l}}(\Theta+\tau,\Theta) & I \end{pmatrix}^{-1} =
$$

$$
\begin{pmatrix} G_{\vec{s},\vec{l}}(\Theta,\Theta) & G_{\vec{s},\vec{l}}(\Theta,\Theta+\tau) \\ G_{\vec{s},\vec{l}}(\Theta+\tau,\Theta) & G_{\vec{s},\vec{l}}(\Theta+\tau,\Theta+\tau) \end{pmatrix} \qquad (4.47)
$$

For very large but finite values of β, we can calculate the left hand side of the above equation by using matrix stabilization techniques developed for finite temperature QMC algorithms. The basic idea behind those numerical stabilization techniques is to keep the different scales occurring in the matrices $B_{\vec{s},\vec{l}}$ separate (for a review see ref. [103]). This is achieved by decomposing the matrices $B_{\vec{s},\vec{l}}$ into a UDV form where U is an orthogonal matrix, D a diagonal matrix containing the exponentially large and exponentially small scales, and V a triangular matrix. The calculation of the left hand side of the above equation is done in the following way:

$$
\begin{pmatrix} I & B_{\vec{s},\vec{l}}(\Theta,0) e^{-\beta h_0} B_{\vec{s},\vec{l}}(2\Theta,\Theta+\tau) \\ -B_{\vec{s},\vec{l}}(\Theta+\tau,\Theta) & I \end{pmatrix}^{-1} = \begin{pmatrix} I & U_1 D_1 V_1 \\ U_2 D_2 V_2 & I \end{pmatrix}^{-1} =
$$

$$
\begin{pmatrix} V_2 & 0 \\ 0 & V_1 \end{pmatrix}^{-1} \begin{pmatrix} (V_2 U_1)^{-1} & D_1 \\ D_2 & (V_1 U_2)^{-1} \end{pmatrix}^{-1} \begin{pmatrix} U_1 & 0 \\ 0 & U_2 \end{pmatrix}^{-1} =
$$

$$
\begin{pmatrix} V_2 & 0 \\ 0 & V_1 \end{pmatrix}^{-1} (U_3 D_3 V_3)^{-1} \begin{pmatrix} U_1 & 0 \\ 0 & U_2 \end{pmatrix}^{-1}. \qquad (4.48)
$$

In the above equation, the matrix D_3 contains only exponentially large scales since the matrices $(V_2 U_1)^{-1}$ and $(V_1 U_2)^{-1}$ act as a cutoff to the exponentially small scales in the matrices D_2 and D_1. Since the other matrices are all well conditioned, the final matrix multiplication is well defined.

A convenient choice of H_0 is obtained in a basis where the trial wave function may be written as:

$$|\Psi_T\rangle = \prod_{n=1}^{N_p} \gamma_n^\dagger |0\rangle. \tag{4.49}$$

In this basis, we define H_0 through

$$H_0 \gamma_n^\dagger |0\rangle = \begin{cases} -\gamma_n^\dagger |0\rangle \text{ if } \gamma_n^\dagger \gamma_n |\Psi_T\rangle = |\Psi_T\rangle \\ +\gamma_n^\dagger |0\rangle \text{ if } \gamma_n^\dagger \gamma_n |\Psi_T\rangle = 0 \end{cases} \tag{4.50}$$

(Here, the energy unit is set by the hopping matrix element t.) For this choice of H_0 values of $\beta t \sim 40$ were well sufficient to satisfy eq. (4.46) within required numerical precision. [1] The above numerical stabilization scheme was indeed successful in all examined cases.

4.6 Tables and figures

$\Delta\tau t$	E/Nt	$S(\pi,\pi)/N$
0.0	-0.8575 ± 0.0003	0.1579 ± 0.0007
0.0625	-0.8571 ± 0.0004	0.1578 ± 0.0009
0.1	-0.8571 ± 0.0003	0.1570 ± 0.0006
0.125	-0.8570 ± 0.0003	0.1564 ± 0.0007
0.166	-0.8563 ± 0.0003	0.1557 ± 0.0008

Table 4.1: Energy per site and $S(\pi,\pi)$ as a function of $\Delta\tau t$ for the Hubbard model at $U/t = 4$ on a 6×6 lattice. The simulations were carried out with the PQMC algorithm at $2\Theta t = 5$. The quoted values at $\Delta\tau t = 0$ are obtained from a least square fit to the form $a + b(\Delta\tau t)^2$. Here we have used the symmetric Trotter decomposition of Eq. (4.32).

[1] Typically, Eq. (4.46) was satisfied on average up to 10^{-11} in absolute values.

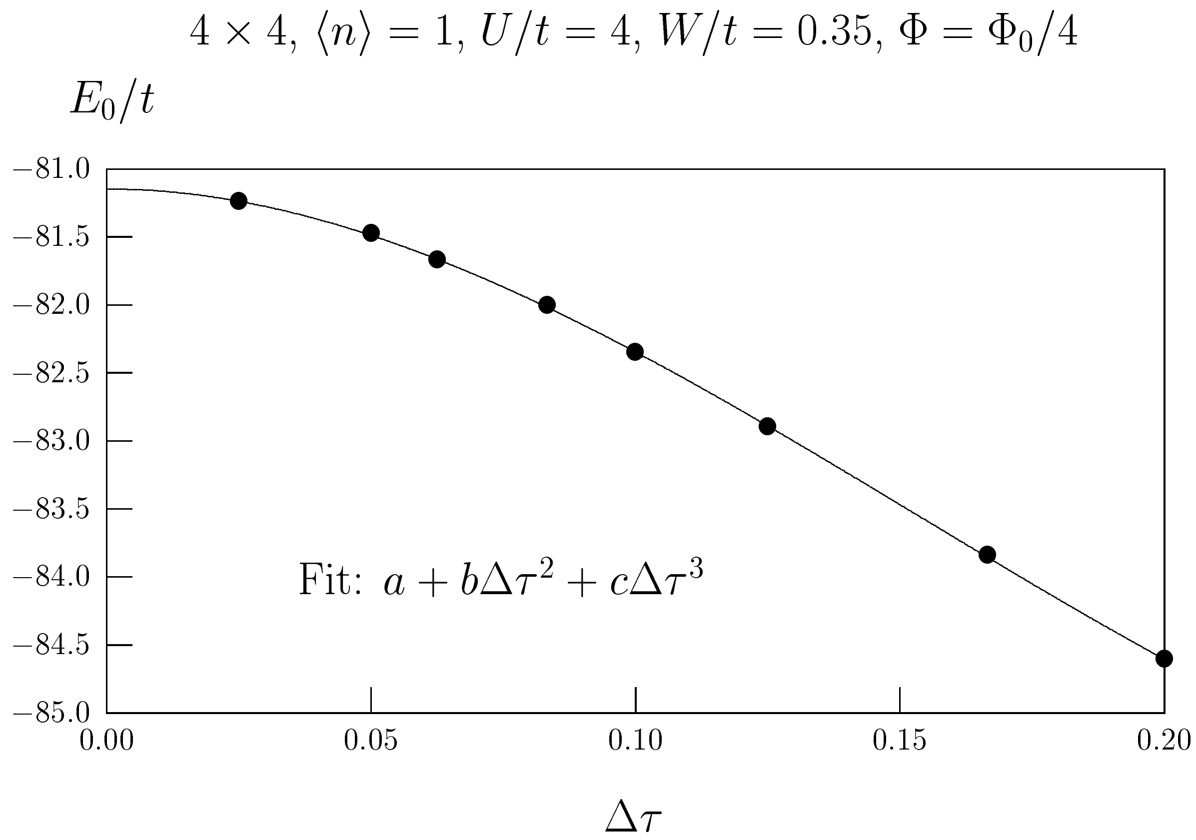

Figure 4.1: Total energy as obtained with the PQMC at $\Theta t = 1$ as a function of $\Delta\tau$. The solid line is a least square fit to the form $a + b\Delta\tau^2 + c\Delta\tau^3$ with $a = -81.146 \pm 0.015$, $b = -153 \pm 3$ and $c = 334 \pm 15$. The energy unit is set by $t = 1$.

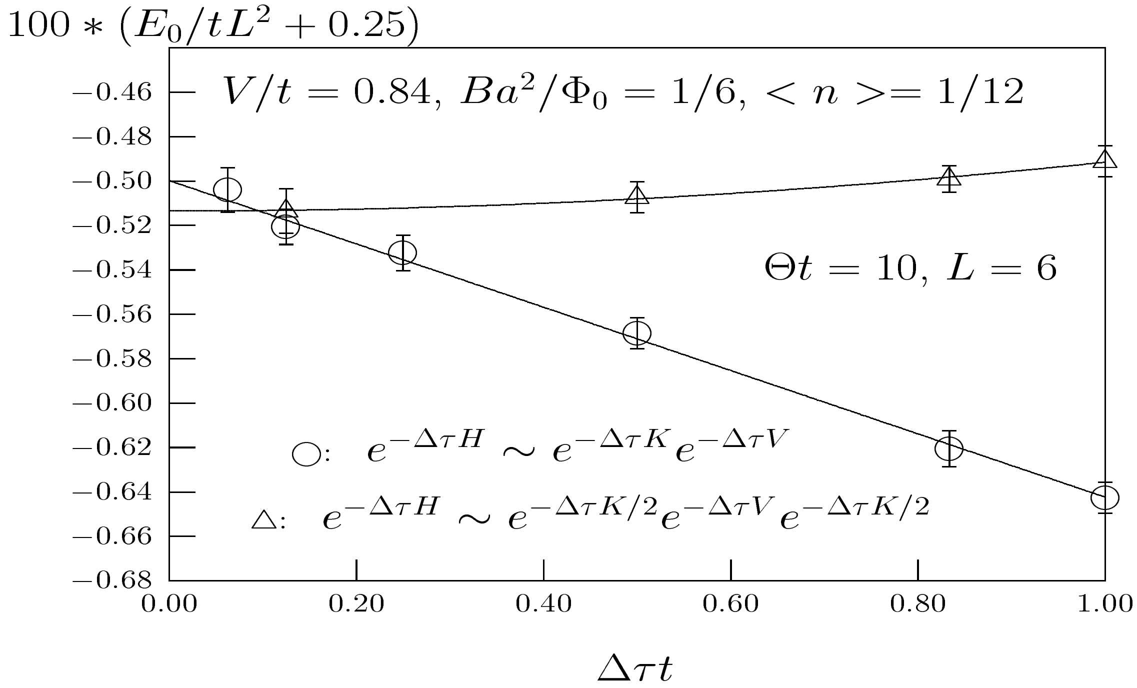

Figure 4.2: Ground state energy for spinless fermions on a square lattice in a transverse magnetic field and submitted to a nearest neighbor repulsive interaction (see equation (4.31)) as a function of $\Delta\tau t$. Here, K denotes the kinetic energy and V the two-body interaction of the Hamiltonian of Eq. 4.31. Within our error and for both Trotter decompositions, the energy scales to the same $\Delta\tau t = 0$ value. For the symmetric Trotter decomposition (4.32) we fit the data to the form $A + B(\Delta\tau t)^2$ whereas for the asymmetric decomposition (4.5), the data follows well a $A + B(\Delta\tau t)$ form.

6×6, $\langle n \rangle = 1$, $U/t = 4$, $W/t = 0.35$, $\Phi = 0$

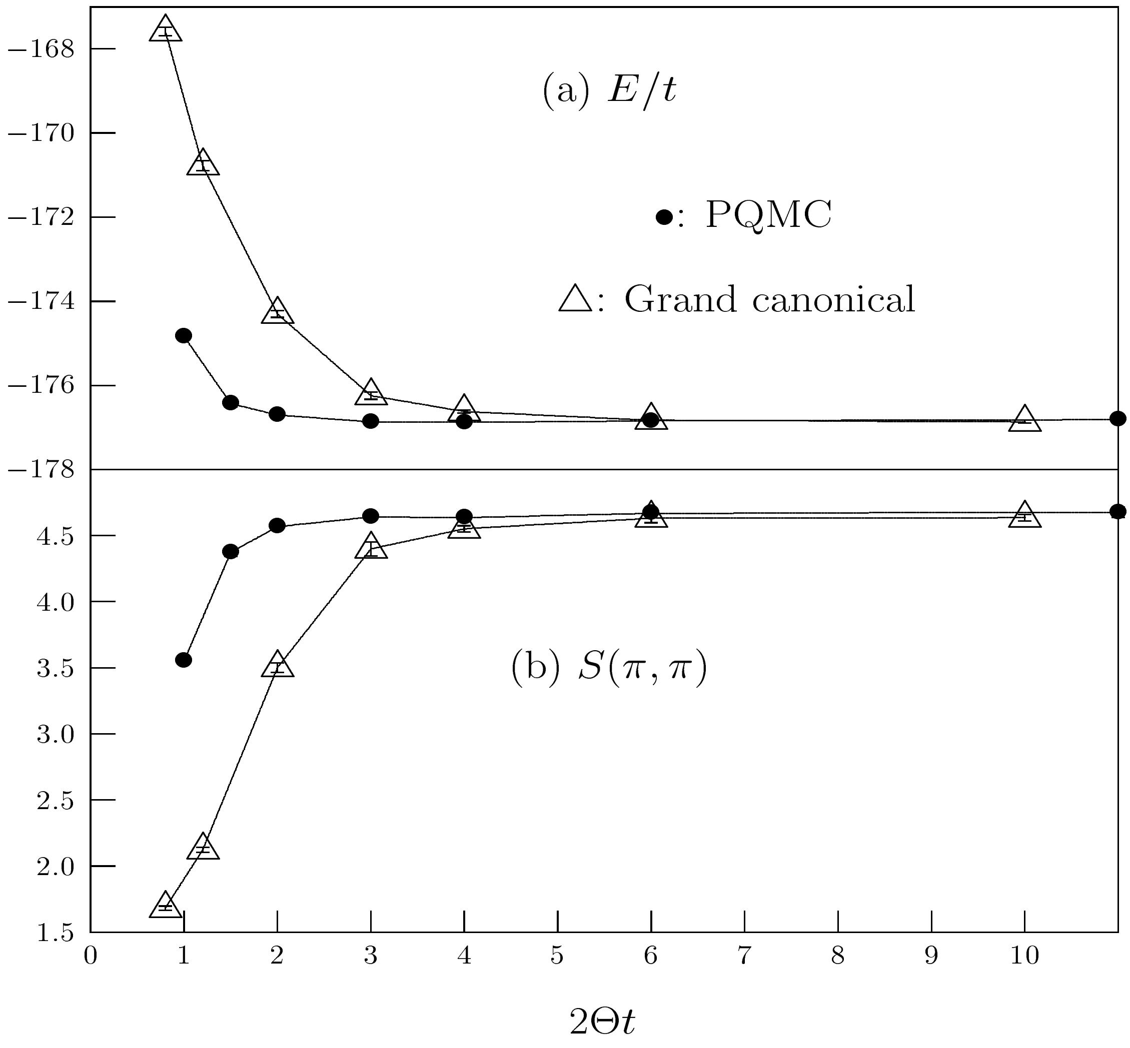

Figure 4.3: •: $\langle \Psi_T | e^{-\Theta H} O e^{-\Theta H} | \Psi_T \rangle / \langle \Psi_T | e^{-2\Theta H} | \Psi_T \rangle$ as a function of the projection parameter Θ. The trial wave function is a singlet ground state of the kinetic energy in Hubbard Hamiltonian. △: $\mathrm{Tr}\left(e^{-2\Theta H} O\right) / \mathrm{Tr}\left(e^{-2\Theta H}\right)$.
We have considered two observables: (a) $O = H$ (b)$O = S(\pi, \pi)$

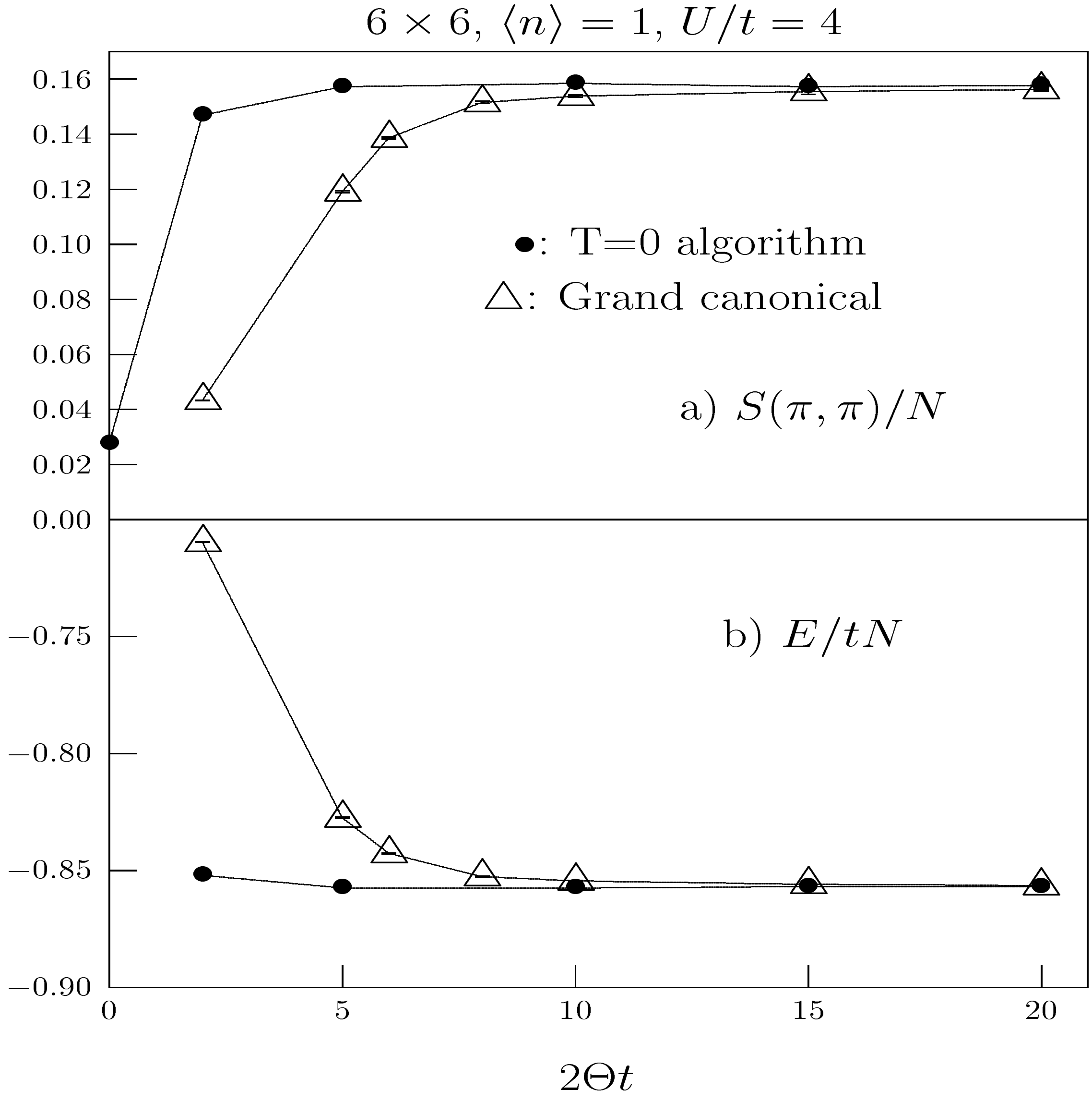

Figure 4.4: Same as Fig. 4.3 but for the Hubbard model. Here we equally consider periodic boundary conditions.

Chapter 5

Summary and Conclusion

Our results are at best summarized by the schematic zero temperature phase diagram of Fig. 5.1 in the W, μ plane. Here we keep the Hubbard U constant, μ is the chemical potential and W the magnitude of the term given by the square of a local kinetic energy. This term was introduced in Chap. 3 and essentially contains pair hopping processes. We have studied this phase diagram along three directions.

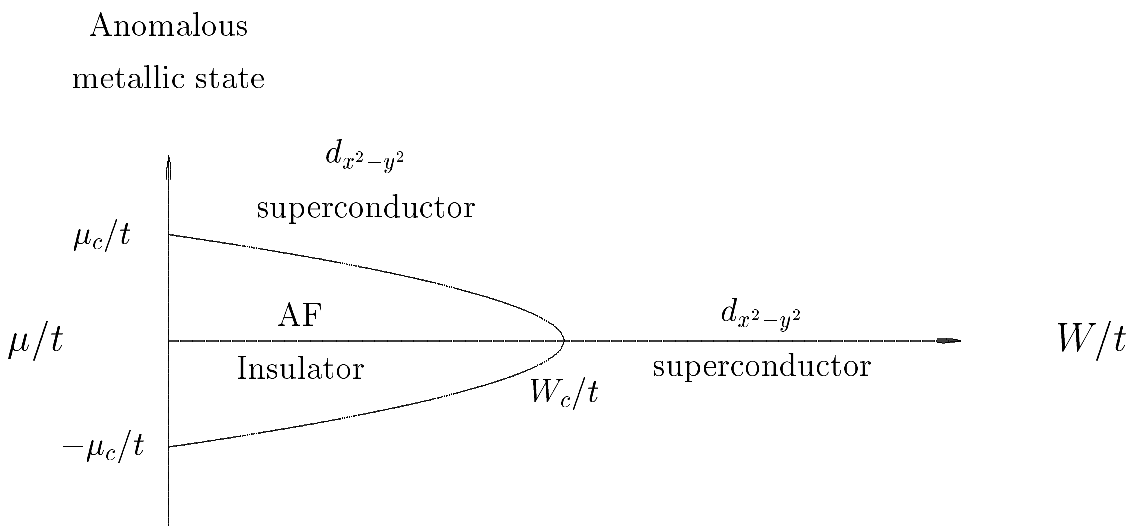

Figure 5.1: Schematic phase diagram of the t-U-W model (See. Eq. (3.4)) in the μ, W plane at fixed U. The intercept of the W, μ axis corresponds to $\mu = W = 0$. At $\mu = 0$ the model is particle-hole symmetric so that the physics is independent on the sign of the chemical potential.

i: In Chap. 1 and 2 we concentrated on the doping induced metal-insulator transition for the Hubbard model. This corresponds to scanning Fig. 5.1 at $W = 0$ as a function of chemical potential. We studied the metal-insulator transition by approaching it both from the insulating and metallic sides.

In Chap. 1 we computed the high frequency Hall coefficient. Our results are consistent with the statement that the both in the weak and strong coupling regimes of the Hubbard model, the low-temperature high frequency Hall coefficient remains electron-like with small amplitude at the metal-insulator transition. Thus, we conclude that the metal-insulator transition is driven by the divergence of the effective mass as opposed to the vanishing of the charge carriers. In the strong coupling and low doping limits, the high frequency Hall coefficient shows a rich temperature behavior: hole-like for $J < T < U$, electron-like with small amplitude for $T < J$ and $T > U$. Here, $J = 4t^2/U$.

In Chap. 2 we computed the zero temperature Green function for frequencies $|\omega| < \mu_c$. At large distances this quantity behaves as $G(\vec{r},\omega) = \exp(-|\vec{r}|/\xi_l)$ with $\xi_l \sim |\omega - \mu_c|^{-1/4}$. The advantage of studying the metal-insulator transition by approaching it from the insulator side lies in the fact that the minus-sign problem inherent to the quantum Monte Carlo method may be avoided. The calculation of ξ_l is based on high precision zero-temperature simulations on lattice size up to 16×16. In a single particle picture, $\xi_l \sim |\omega - \mu_c|^{-1/4}$ leads to the existence of flat-bands with dispersion relation $|\vec{k}|^4$ at the critical chemical potential. Based on the calculation of the single particle spectral function $A(\vec{k},\omega)$ at zero temperature and half-band filling we gave numerical evidence for the occurrence of such a dispersion relation around the $(0,\pm\pi)$, $(\pm\pi,0)$ points in the Brillouin zone (Sec. 2.4).

The charge susceptibility in the metallic state equally shows anomalous behavior. The data of Ref. [6, 29] are consistent with $\chi_c \sim |\mu - \mu_c|^{-1/2} \sim \delta^{-1}$. This behavior is independent on perfect nesting [6]. Similar results were obtained for the t-J model [30, 33].

Finally, the quantity $D/\langle K \rangle$ where $\langle K \rangle$ is the kinetic energy and D the Drude weight has been computed on small clusters at $T = 0$ for the t-J model [39]. The data are compatible with $D/\langle K \rangle \sim \delta$. In the strong coupling limit, one expects $\langle K \rangle \sim \delta$ so that $D \sim \delta^2$. Since the optical conductivity satisfies the sum rule $\int d\omega \sigma(\omega) \sim -\langle K \rangle$ the majority of the weight in $\sigma(\omega)$ is located in the incoherent response.

The results $\xi_l \sim |\omega - \mu_c|^{-1/4}$, $\chi_c \sim |\mu - \mu_c|^{-1/2} \sim \delta^{-1}$ and $D \sim \delta^2$ may be consistently understood under the assumption of a single relevant length scale and a hyperscaling form for the singular part of the free energy provided that one accepts an anomalously large dynamical exponent $z = 4$ [22, 40]. Since the transition is triggered by the chemical potential, $\nu z = 1$. Here ν corresponds to the correlation lenght exponent. Within this classification, the band metal-insulator transition corresponds to a universality class with $z = 2$, and $\nu = 1/2$. [1]

[1] As seen in the introduction, the band-metal insulator transition is characterize $R_H \sim 1/\delta$, $\chi_c \sim \delta^{1-2/d}$, $\xi_l \sim |\omega - \mu_c|^{-1/2}$ and $D \sim \delta$. Here, d is the dimensionality.

It is a challenging issue to elaborate a microscopic theory capable reproducing the above summarized data in the energy window accessible to numerics. This theory will have to take into account the subtle interplay between spin and charge degrees of freedom.

ii: In Chap. 3 we scanned the phase diagram as a function of chemical potential at finite $W < W_c$ and $U/t = 4$. For this value of U/t, $W_c \sim 0.3t$. The low energy physics of the W term is partially contained in the three site terms obtained in a strong coupling expansion of the Hubbard model [41]. Already as $W/t = 0.05$, the localization length satisfies: $\xi_l \sim |\omega - \mu_c|^{-1/2}$ (Sec. 3.2.1). This change in exponent is related to a transition from a $|\vec{k}|^4$ to a $|\vec{k}|^2$ dispersion relation around the $(0, \pm\pi)$, $(\pm\pi, 0)$ points in the Brillouin zone as W is enhanced. At finite dopings d-wave pair-field correlations are strongly enhanced with growing values of W/t. Furthermore, a pseudogap feature is observed in the static spin susceptibility. The results are consistent with the interpretation that the W term radically alters the nature of the metal-insulator transition. The origin being the onset of d-wave superconductivity in the metallic state. The critical value of W, W_c^{μ}/t, at which the nature of the metal-insulator transition changes is uncertain. We can at present only give an upper-bound: $W_c^{\mu}/t < 0.05$ for $U/t = 4$. Clearly, we cannot rule out the possibility that at energy scales beyond reach of the Monte Carlo method, the Hubbard model shows similar physics than the t-U-W model at $W > W_c^{\mu}$.

The above analysis suggests that the metal-insulator transition characterized by the dynamical exponent $z = 4$ is destabilized by a finite value of W to the superconductor-insulator transition with $z = 2$. [2] This instability is triggered by a gain in kinetic energy. The change in universality class comes with a restoration of coherence since when $z = 2$, $D \sim \delta$ as opposed to $D \sim \delta^2$ when $z = 4$. Numerical support for this behavior of the Drude weight has been given in Ref. [39].

iii: Finally, we considered the t-U-W model at half-band filling (i.e $\mu = 0$), $U/t = 4$ and as a function of W. W triggers a quantum transition between an antiferromagnetic Mott insulator and $d_{x^2-y^2}$ superconductor. For $U/t = 4$, this transition occurs at $W_c/t \sim 0.3$. The nature of the spin-spin correlations in the superconducting state show a remarkable compatibility between antiferromagnetic fluctuations and $d_{x^2-y^2}$ superconductivity. At $T = 0$, long range spin-spin correlations are not present in the superconducting phase. However, $S(\vec{r}) \sim \cos(\vec{Q}\vec{r})|\vec{r}|^{-\alpha}$ with $1 < \alpha < 2$ and $\vec{Q} \equiv (\pi, \pi)$. Since we are in two-dimensions this leads to a divergence of $S(\vec{Q}) \sim \sum_{\vec{r}} e^{i\vec{Q}\vec{r}} S(\vec{r})$. Furthermore, the exponent α depends on the coupling constants U and W. This result was shown to be boundary independent and is based on simulations on lattice sizes up to 24×24. At finite temperatures we computed the spin susceptibility $\chi(\vec{q}, \omega)$. As expected for a $d_{x^2-y^2}$ superconduc-

[2] We note that the doping induced metal-superfluid transition for two-dimensional bosons, is described by hyperscaling with exponents: $\nu = 1/2$ and $z = 2$ [111].

tor, our results are consistent with the vanishing of the uniform spin susceptibility, $\mathrm{Re}\chi(\vec{q}=0,\omega=0)$ and spin-lattice relaxation rate $1/T_1$ in the low temperature limit. However, the staggered spin susceptibility $\mathrm{Re}\chi(\vec{Q},\omega=0)$ *diverges* in the zero temperature limit. The dynamical spin structure factor, $S(\vec{Q},\omega)$ has a peak structure at finite frequencies. Due to the sum rule $\int \mathrm{d}\omega S(\vec{Q},\omega) = S(\vec{Q})$ the weight under this peak diverges.

The t-U-W model shows a rich phase diagram. Further studies for the complete understanding of physical properties of the model as function of W, doping and temperature are required.

Acknowledgments

The presented results stem from collaborations with M. Imada and D. J. Scalapino. I thank N. Bulut, T. Dahm, N. Furukawa, W. Hanke, P. A. Lee, T. Müller, M. Muramatsu, A. Sandvik, H. Tsunetsugu, M. Zacher and S. C. Zhang for many instructive conversations. The numerical simulations were carried out on the FACOM VPP500 at the Supercomputer Center of the Institute for Solid State Physics, University of Tokyo, on the Cray-T3E of the HLRS Stuttgart, and Cray-T90 and Cray-T3E of the HLRZ, Jülich.

Appendix

In this appendix, we argue that at $T=0$

$$\lim_{i\omega_m\to 0}\lim_{B\to 0} R_H(B,i\omega_m) = \lim_{\omega\to 0}\lim_{B\to 0} R_H(B,\omega), \tag{1}$$

under the assumption that the Drude weight does not vanish in the limit $B\to 0$. This assumption is justified for the Hubbard model away from half-band filling.

On the real time axis, the conductivity tensor is given by

$$\sigma_{\alpha,\gamma}(\omega) = \frac{e^2}{i(\omega+i\epsilon)} D_{\alpha,\gamma}(\omega) \tag{2}$$

where

$$D_{\alpha,\gamma}(\omega) = \frac{1}{N}\left(\langle K_\alpha\rangle\delta_{\alpha,\gamma} + i\int_0^\infty \mathrm{d}t e^{i(\omega+i\epsilon)t}\langle[j_\alpha(t), j_\gamma(0)]\rangle\right) \tag{3}$$

Here, $\hbar=1$, and N is the number of sites of the square lattice. The current and kenetic energy is given by:

$$\begin{aligned} j_\alpha &= -i\sum_{\vec{i},\sigma}\left(t_{\vec{i},\vec{i}+\vec{a}_\alpha}(\vec{A})c^\dagger_{\vec{i},\sigma}c_{\vec{i}+\vec{a}_\alpha,\sigma} - t_{\vec{i}+\vec{a}_\alpha,\vec{i}}(\vec{A})c^\dagger_{\vec{i}+\vec{a}_\alpha,\sigma}c_{\vec{i},\sigma}\right) && (4)\\ K_\alpha &= \sum_{\vec{i},\sigma}\left(t_{\vec{i},\vec{i}+\vec{a}_\alpha}(\vec{A})c^\dagger_{\vec{i},\sigma}c_{\vec{i}+\vec{a}_\alpha,\sigma} + t_{\vec{i}+\vec{a}_\alpha,\vec{i}}(\vec{A})c^\dagger_{\vec{i}+\vec{a}_\alpha,\sigma}c_{\vec{i},\sigma}\right). && (5)\\ t_{\vec{i},\vec{j}}(\vec{A}) &= -t\exp\left(\frac{2\pi i}{\Phi_0}\int_{\vec{i}}^{\vec{j}}\vec{A}\cdot d\vec{l}\right). && (6)\end{aligned}$$

Here, Φ_0 is the flux quantum and in the Landau gauge $\vec{A}(\vec{x}) = -B(y,0,0)$.

In the weak field limit, $\sigma_{x,y}(\omega)\sim B$. Hence,

$$\lim_{\omega\to 0}\lim_{B\to 0} R_H(B,\omega) = \lim_{\omega\to 0}\lim_{B\to 0}\frac{1}{e^2}\frac{i\omega D_{x,y}(\omega)/B}{D^2_{x,x}(\omega)}. \tag{7}$$

D_{xx} may be written as:

$$\begin{aligned} \mathrm{Re}D_{x,x}(\omega) &= \frac{1}{N}\left(\langle K_x\rangle + \sum_n |\langle n|j_x|0\rangle|^2\left(P\frac{1}{E_n-E_0-\omega} + P\frac{1}{E_n-E_0+\omega}\right)\right)\\ \mathrm{Im}D_{x,x}(\omega) &= \frac{\pi}{N}\sum_n |\langle n|j_x|0\rangle|^2\left(\delta\left(E_n-E_0-\omega\right) - \delta\left(E_n-E_0+\omega\right)\right), && (8)\end{aligned}$$

and $i\omega D_{x,y}(\omega)/B$ is given by:

$$\begin{aligned}
\mathrm{Re}\,(i\omega D_{x,y}(\omega)/B) &= \frac{\omega}{BN^2}\sum_n \left(P\frac{i\langle 0|j_x|n\rangle\langle n|j_y|0\rangle}{E_n - E_0 - \omega} + P\frac{i\langle 0|j_y|n\rangle\langle n|j_x|0\rangle}{E_n - E_0 + \omega} \right) \\
\mathrm{Im}\,(i\omega D_{x,y}(\omega)/B) &= \frac{\pi}{BN^2}\sum_n \\
&\omega[i\langle 0|j_x|n\rangle\langle n|j_y|0\rangle\delta(E_n - E_0 - \omega) - i\langle 0|j_y|n\rangle\langle n|j_x|0\rangle\delta(E_n - E_0 + \omega)].
\end{aligned} \tag{9}$$

In the above equations $\sum_n |n\rangle\langle n| = 1$, with $H|n\rangle = E_n|n\rangle$ and P denotes the principal value. Note that for the Hubbard model, $H = \sum_{<\vec{i},\vec{j}>,\sigma} t_{\vec{i},\vec{j}}(\vec{A}) c^\dagger_{\vec{i},\sigma} c_{\vec{j},\sigma}$ $+U\sum_{\vec{i}} n_{\vec{i},\uparrow} n_{\vec{i},\downarrow}$ one may choose a basis such that $\langle 0|j_y|n\rangle\langle n|j_x|0\rangle$ and $\langle 0|j_x|n\rangle\langle n|j_y|0\rangle$ are purely imaginary. As apparent from equations (8) and (9),

$$\lim_{\omega\to 0}\lim_{B\to 0} \mathrm{Im} D_{x,x}(\omega) = 0 \tag{10}$$

and

$$\lim_{\omega\to 0}\lim_{B\to 0} \mathrm{Im}\,(i\omega D_{x,y}(\omega)/B) = 0. \tag{11}$$

In a metallic state, the Drude weight

$$D \sim -\lim_{\omega\to 0}\lim_{B\to 0} \mathrm{Re} D_{x,x}(\omega) \tag{12}$$

does not vanish. Hence equation (7) may be written as:

$$\lim_{\omega\to 0}\lim_{B\to 0} R_H(B,\omega) = \lim_{\omega\to 0}\lim_{B\to 0} \frac{1}{e^2}\frac{\mathrm{Re}\,(i\omega D_{x,y}(\omega)/B)}{(\mathrm{Re} D_{x,x}(\omega))^2}. \tag{13}$$

On the imaginary time axis the conductivity tensor is given by

$$\sigma_{\alpha,\gamma}(i\omega_m) = -\frac{e^2}{\omega_m} D_{\alpha,\gamma}(i\omega_m) \tag{14}$$

where

$$D_{\alpha,\gamma}(i\omega_m) = \lim_{\beta\to\infty}\frac{1}{N}\left(\frac{\langle K\rangle}{2}\delta_{\alpha,\gamma} + \int_0^\beta \mathrm{d}\tau e^{i\omega_m\tau}\langle j_\alpha(\tau) j_\gamma(0)\rangle\right). \tag{15}$$

In the above notation:

$$\lim_{i\omega_m\to 0}\lim_{B\to 0} R_H(B, i\omega_m) = \lim_{i\omega_m\to 0}\lim_{B\to 0}\frac{1}{e^2}\frac{-\omega_m D_{x,y}(i\omega_m)/B}{D^2_{x,x}(i\omega_m)} \tag{16}$$

with

$$D_{x,x}(i\omega_m) = \frac{1}{N}\left(\langle K_x\rangle + \sum_n |\langle n|j_x|0\rangle|^2 \left(\frac{1}{E_n - E_0 - i\omega_m} + \frac{1}{E_n - E_0 + i\omega_m}\right)\right) \tag{17}$$

and

$$-\omega_m D_{x,y}(i\omega_m)/B = \frac{i\omega_m}{BN}\sum_n \left(\frac{i\langle 0|j_x|n\rangle\langle n|j_y|0\rangle}{E_n - E_0 - i\omega_m} + \frac{i\langle 0|j_y|n\rangle\langle n|j_x|0\rangle}{E_n - E_0 + i\omega_m}\right). \tag{18}$$

One may see from equations (8) and (17) that

$$\lim_{i\omega_m\to 0}\lim_{B\to 0} D_{x,x}(i\omega_m) = \lim_{\omega\to 0}\lim_{B\to 0}\mathrm{Re}D_{x,x}(\omega). \tag{19}$$

Similarly, from equations (9) and (18) follows:

$$\lim_{i\omega_m\to 0}\lim_{B\to 0}\left(-\omega_m D_{x,y}(i\omega_m)/B\right) = \lim_{\omega\to 0}\lim_{B\to 0}\mathrm{Re}\left(i\omega D_{x,y}(\omega)/B\right). \tag{20}$$

Equation (1) then follows from equation (13).

Bibliography

[1] E. H. Lieb and F. Y. Wu, Phys. Rev. Lett. **74**, 3872 (1968).

[2] W. Kohn, Phys. Rev. A **133**, 171 (1964).

[3] D. J. Scalapino, S. White, and S. Zhang, Phys. Rev. Lett. **68**, 2830 (1992).

[4] D. J. Scalapino, S. White, and S. Zhang, Phys. Rev. B. **47**, 7995 (1993).

[5] F. F. Assaad, W. Hanke, and D. J. Scalapino, Phys. Rev. Lett. **71**, 1915 (1993).

[6] N. Furukawa and M. Imada, J. Phys. Soc. Jpn. **62**, 2557 (1993).

[7] N. Bulut, D. J. Scalapino, and S. R. White, Phys. Rev. Lett. **73**, 748 (1994).

[8] F. F. Assaad and M. Imada, J. Phys. Soc. Jpn. **65**, 189 (1996).

[9] M. S. Makivic and H. Q. Ding, Phys. Rev. B **43**, 3562 (1991).

[10] E. Manousakis, Rev. Mod. Phys. **63**, 1 (1991).

[11] J. E. Hirsch and S. Tang, Phys. Rev. Lett. **62**, 591 (1989).

[12] S. White *et al.*, Phys. Rev. B **40**, 506 (1989).

[13] J. G. Bednorz and K. A. Müller, Z. Phys. B **64**, 189 (1986).

[14] W. E. Picket, Rev. Mod. Phys. **61**, 443 (1989).

[15] B. Keimer *et al.*, Phys. Rev. B. **46**, 14034 (1992).

[16] P. W. Anderson, Science **235**, 1196 (1987).

[17] F. C. Zhang and T. M. Rice, Phys. Rev. B. **37**, 3759 (1988).

[18] S. Chakravarty, B. I. Halperin, and D. R. Nelson, Phys. Rev. Lett. **60**, 1057 (1988).

[19] S. Chakravarty, B. I. Halperin, and D. R. Nelson, Phys. Rev. B **39**, 2344 (1989).

[20] E. Dagotto and T. M. Rice, Science **271**, 618 (1996).

[21] R. M. Noack, S. White, and D. J. Scalapino, Phys. Rev. Lett. **73**, 882 (1994).

[22] M. Imada, A. Fujimori, and Y. Tokura, Rev. Mod. Phys. **70**, No. 4 (1998).

[23] A. Luther and I. Peschel, Phys. Rev. B. **12**, 3908 (1975).

[24] H. Frahm and V. E. Korepin, Phys. Rev. B. **42**, 10553 (1990).

[25] M. Imada, N. Furukawa, and T. M. Rice, J. Phys. Soc. Jpn. **61**, 3861 (1992).

[26] Y. Iino and M. Imada, J. Phys. Soc. Jpn. **64**, 4392 (1995).

[27] Y. M. Vilk, L. Chen, and A. M. S. Tremblay, Phys. Rev. B **49**, 13267 (1994).

[28] Y. M. Vilk and A. M. S. Tremblay, J. Phys. I France **7**, 1309 (1997).

[29] N. Furukawa and M. Imada, J. Phys. Soc. Jpn. **61**, 3331 (1992).

[30] M. Kohno, Phys. Rev. B **55**, 1435 (1997).

[31] T. Usuki, N. Kawakami, and A. Okiji, Phys. Lett. A **135**, 476 (1989).

[32] B. S. Shastry and B. Sutherland, Phys. Rev. Lett. **65**, 243 (1990).

[33] J. Jaklic and P. Prelovsek, Phys. Rev. Lett. **77**, 892 (1996).

[34] G.Dopf *et al.*, Phys. Rev. Lett. **68**, 2082 (1992).

[35] E. Dagotto, Rev. of Mod. Phys. **66**, 763 (1994).

[36] N. Bulut, D. J. Scalapino, and S. R. White, Phys. Rev. B **50**, 7215 (1994).

[37] D. S. Dessau *et al.*, Phys. Rev. Lett. **71**, 2781 (1993).

[38] Z. X. Shen and D. S. Dessau, Phys. Rep. **253**, 1 (1995).

[39] H. Tsunetsugu and M. Imada, J. Phys. Soc. Jpn. **67**, No. 6 (1998).

[40] M. Imada, J. Phys. Soc. Jpn. **64**, 2954 (1995).

[41] J. E. Hirsch, Phys. Rev. Lett. **54**, 1317 (1985).

[42] Y. Tokura *et al.*, Phys. Rev. Lett. **70**, 2126 (1993).

[43] W. Metzner and D. Vollhardt, Phys. Rev. Lett. **62**, 324 (1989).

[44] A. Georges, G. Kotliar, W. Krauth, and M. J. Rozenberg, Rev. of. Mod. Phys. **68**, 13 (1996).

[45] E. Müller-Hartmann, Z. Phys. B **74**, 507 (1989).

[46] R. Blankenbecler, D. J. Scalapino, and R. L. Sugar, Phys. Rev. D **24**, 2278 (1981).

[47] J. E. Hirsch, Phys. Rev. B **31**, 4403 (1985).

[48] G. Sugiyama and S. Koonin, Anals of Phys. **168**, 1 (1986).

[49] S. Sorella, S. Baroni, R. Car, and M. Parrinello, Europhys. Lett. **8**, 663 (1989).

[50] S. Sorella *et al.*, Int. J. Mod. Phys. B **1**, 993 (1989).

[51] W. von der Linden, Applied Physics A **60**, 155 (1995).

[52] M. Jarrell and J. Gubernatis, Physics Reports **269**, 133 (1996).

[53] F. F. Assaad and M. Imada, Phys. Rev. Lett **74**, 3868 (1995).

[54] F. F. Assaad and M. Imada, Phys. Rev. Lett **76**, 3176 (1996).

[55] N. Furukawa, F. F. Assaad, and M. Imada, J. Phys. Soc. Jpn. **65**, 2339 (1996).

[56] F. F. Assaad, M. Imada, and D. J. Scalapino, Phys. Rev. Lett **77**, 4592 (1996).

[57] F. F. Assaad, M. Imada, and D. J. Scalapino, Phys. Rev. B **56**, 15001 (1997).

[58] F. F. Assaad and M. Imada, Phys. Rev. B **58**, 1845 (1998).

[59] B. Shastry, B. Shraiman, and R. Singh, Phys. Rev. Lett. **70**, 2004 (1993).

[60] M. Imada, J. Phys. Soc. Jpn. **62**, 1105 (1993).

[61] E. Fradkin, *Field Theories of condensed matter systems*, *Frontiers in Physics* (Addison-Wesley Publishing Company, Redwood City, 1991).

[62] J. M. Ziman, *Principles of the Theory of Solids*, 2 ed. (Cambridge University Press, Cambridge, 1972).

[63] F. F. Assaad, W. Hanke, and D. J. Scalapino, Phys. Rev. B **50**, 12835 (1994).

[64] E. Dagotto *et al.*, Phys. Rev. B **45**, 10741 (1992).

[65] S. G. Kaplan *et al.*, Phys. Rev. Lett. **76**, 696 (1996).

[66] P. W. Anderson, Phys. Rev. Lett. **67**, 2092 (1991).

[67] L. B. Ioffe and A. J. Millis, Cond-mat/9801092 .

[68] N. P. Ong *et al.*, Phys. Rev. B **35**, 8807 (1987).

[69] H. Takagi *et al.*, Phys. Rev. B **40**, 2254 (1989).

[70] T. Nagano *et al.*, Phys. Rev. B **48**, 9689 (1993).

[71] T. Nishikawa, J. Takeda, and M. Sato, J. Phys. Soc. Jpn. **62**, 2568 (1993).

[72] H. Y. Hwang and et al., Phys. Rev. Lett. **72**, 2636 (1994).

[73] H. Tsunetsugu and M. Imada, J. Phys. Soc. Jpn. **66**, 1876 (1997).

[74] G. D. Mahan, *Many-Particle Physics*, 2 ed. (Plenum Press, New York, 1990).

[75] P. W. Anderson, Phys. Rev. **124**, 41 (1961).

[76] J. J. Deisz, W. von der Linden, R. Preuss, and W. Hanke, in *Computer Simulations in Condensed Matter Physics*, edited by D. Landau, K. Moon, and H.-B. Schüttler (Springer, Berlin, 1994), Vol. 8.

[77] E. Dagotto, A. Nazarenko, and M. Boninsegni, Phys. Rev. Lett. **73**, 728 (1994).

[78] R. Preuss, W. Hanke, C. Gröber, and H. G. Evertz, Phys. Rev. Lett. **79**, 1122 (1997).

[79] B. O. Wells *et al.*, Phys. Rev. Lett. **74**, 964 (1995).

[80] C. Kim *et al.*, Phys. Rev. Lett. **80**, 4245 (1998).

[81] R. Eder, Y. Ohta, and G. A. Sawatzky, Phys. Rev. B. **55**, 3414 (1997).

[82] Z. X. Shen and J. R. Schrieffer, Phys. Rev. Lett. **78**, 1771 (1997).

[83] K. Gofron *et al.*, Phys. Rev. Lett. **73**, 3302 (1994).

[84] S. L. Sondhi, S. M. Girvin, J. P. Carini, and D. Shahar, Rev. of Mod. Phys. **69**, 315 (1997).

[85] D. J. Scalapino, in *Proceedings of the Internation School of Physics, Enrico Fermi*, edited by R. A. Broglia and J. R. Schrieffer (North Holland, N.Y., 1994), Vol. CXX1, p. 95.

[86] G. Dopf, A. Muramatsu, and W. Hanke, Phys. Rev. Lett. **68**, 1992 (1992).

[87] K. Kuroki and H. Aoki, Phys. Rev. Lett. **76**, 440 (1996).

[88] H. Endres, W. Hanke, H. G. Evertz, and F. F. Assaad, Phys. Rev. Lett. **78**, 160 (1997).

[89] S. R. White and D. J. Scalapino, Phys. Rev. Lett. **80**, 1272 (1998).

[90] W. P. Su, J. R. Schrieffer, and A. J. Heeger, Phys. Rev. B. **22**, 2099 (1980).

[91] J. E. Hirsch, Phys. Rev. B **35**, 8726 (1987).

[92] N. Byers and C. N. Yang, Phys. Rev. Lett. **7**, 46 (1961).

[93] C. N. Yang, Rev. of Mod. Phys. **34**, 694 (1962).

[94] N. Bulut and D. J. Scalapino, Phys. Rev. B **45**, 2371 (1992).

[95] D. J. Scalapino, Phys. Rep. **250**, 329 (1995).

[96] M. Randeria and J. C. Campuzano, High T_c superconductors: new insights from angle-resolved photoemission. Cond-mat/9709107 .

[97] T. Mason *et al.*, Phys. Rev. Lett. **77**, 1604 (1996).

[98] J. Rossat-Mignod *et al.*, Physica C **185-189**, 86 (1991).

[99] H. F. Fong *et al.*, Phys. Rev. Lett. **75**, 316 (1995).

[100] H. F. Fong, B. Keimer, D. L. Milius, and I. A. Aksay, Phys. Rev. Lett. **78**, 713 (1997).

[101] Y. Itoh *et al.*, J. Phys. Soc. Jpn. **61**, 1287 (1992).

[102] M. H. Julien *et al.*, Phys. Rev. Lett. **76**, 4238 (1996).

[103] E. Loh and J. Gubernatis, in *Modern Problems of Condensed Matter Physics*, edited by W. Hanke and Y. V. Kopaev (North Holland, Amsterdam, 1992), Vol. 32, p. 177.

[104] W. von der Linden, Phys. Rep. **220**, 53 (1992).

[105] R. Fye, Phys. Rev. B. **33**, 1028 (1986).

[106] J. E. Hirsch, Phys. Rev. B **28**, 4059 (1983).

[107] N. Furukawa and M. Imada, J. Phys. Soc. Jpn. **60**, 3669 (1991).

[108] M. Imada and Y. Hatsugai, J. Phys. Soc. Jpn. **58**, 3752 (1989).

[109] F. F. Assaad, Helv. Physica Acta **63**, 580 (1990).

[110] J. E. Hirsch, Phys. Rev. B **38**, 12023 (1988).

[111] M. P. A. Fisher, P. Weichman, G. Grinstein, and D. S. Fisher, Phys. Rev. B **40**, 546 (1989).